Optical and Theoretical Studies of Excitons in Few-Layer Lead Iodide

by

Alexis S. Toulouse

A dissertation submitted in partial fulfillment
of the requirements for the degree of
Doctor of Philosophy
(Applied Physics)
in the University of Michigan
2015

Doctoral Committee:

Professor Roberto D. Merlin, Chair
Assistant Professor Hui Deng
Assistant Professor Emmanouil Kioupakis
Professor Çağlıyan Kurdak
Assistant Professor Lu Li

"The secret of happiness is to see all the marvels of the world,
and never to forget the drops of oil on the spoon."

- Paulo Coelho, *The Alchemist*

2015

Pour Maman, Papa, Nicholas, Sonja et Stefan.

ACKNOWLEDGMENTS

The Ph.D. journey has been a long and arduous one, throughout which I have relied on many people for the love, support, and guidance I required along the way. My family, friends and colleagues have been of fundamental importance in helping me to persevere and complete this endeavor. First, I must thank my advisor Roberto Merlin for taking me on as a graduate student. His enthusiasm, insightful guidance and continuous support have been critical to my success. Moreover, his ability to see the big picture and his persistent optimism were invaluable during challenging periods. I must also thank Manos Kioupakis, who has been like a co-advisor the last few years. His dedication, passion for science, eagerness to attack problems, and willingness to spend as much time as necessary to explain even the simplest of things are all testaments to his aptitude as a professor. I would also like to thank Çağlıyan Kurdak, Charles Sutton, Lauren Segall, Cyndi McNabb and the entire Applied Physics family for the fantastic environment they have created and the support they have provided over the years. Furthermore, I would like to thank Lu Li, Hui Deng, Duncan Steel and the rest of my committee for their participation in this process.

I have been lucky to work with and learn from a number of very talented labmates in the Merlin Lab. Andrea Bianchini was like a mentor when I first joined the group and has continued to be a good friend. I am indebted to him for his guidance, particularly in the canonical approach, and for his novel self reflection techniques. Ben Isaacoff was my partner in research for the first few years and has since been a valuable sounding board and good friend. His exuberance along with his practical and fearless approach to science were contagious and much appreciated. Prashant Padmanabhan has been like a younger brother, and his entertaining and gregarious personality has been a refreshing distraction. His passion and willingness to debate anything were both infuriating and incredibly useful in developing my own understanding of things. I am also extremely grateful for the help and discussions I had with Jingjing Li and Ilya Vugmeyster, who were always very friendly and willing to provide advice. Steve Young has been an incredible resource to discuss just about anything with, and his group barbecues have been a great opportunity to socialize outside of work. I would also like to thank Guangsha Shi and Dylan Bayerl for all their

help in my computational work, and especially Guangsha for patiently teaching me to use the various codes. Last but certainly not least, I would like to thank Ibrahim Boulares and Meredith Henstridge for commiserating and supporting me during the final push. They provided entertaining distractions as well as useful discussions, and they have been extremely valuable resources in the lab.

Outside of the lab, I am tremendously grateful for all the friendships I formed in Ann Arbor and the support structure they provided for me. I have to start by thanking my Applied Physics cohort, in particular Dave Anderson and Liz Shtrahman who were my foundation from the beginning to the end. I would like to thank all those who passed through the Brickhouse and made it such a great place to live, especially Michelle, Lucas, Sophie, Rob, Marco, Gina, Claire, Laurel, Jenny, Sarah, Carson, Megan, and of course Haydee. I cannot forget to thank the honorary roommates as well: Chris, Cassandra, Julia and Warren. In addition, I would like to acknowledge some of the other close friends I made during my time here: Smriti, Naike, Jim, Jana, Danny and Jeff. I want to especially thank Sara Bowling for her support and positive impact on my personal development during graduate school. I would also like to thank all the members of the Rackham Student Government, in particular Rahul, Michael, Kaitlin, Phil, as well as the members of the Student Advocates for Graduate Education, especially Mike, David and Manny. It has been a pleasure working with such interesting people with diverse passions, and I am happy to call them friends. I want to also thank the Ann Arbor Soccer Club, my instructors at the Center for Yoga, and the baristas at Mighty Good, my second office. As I look back at my seven years in Ann Arbor, I am most grateful for the time spent together with all of these people!

Finally, I would like to thank my family whose love and support has been ever-present. It is largely because of them that I have had all these opportunities, and I am forever grateful.

TABLE OF CONTENTS

LIST OF FIGURES

LIST OF TABLES

ABSTRACT

Optical and Theoretical Studies of Excitons in Few-Layer Lead Iodide

by

Alexis S. Toulouse

Chair: Roberto D. Merlin

Optical measurements and first-principles calculations of few-layer lead iodide (PbI_2) crystals are presented in this work. Results indicate that the band structure and exciton energies change dramatically from direct-gap bulk to few-layer PbI_2. Moreover, the $n = 1$ exciton appears to be Frenkel-like in nature, in that its energy exhibits a weak dependence on thickness down to atomic length scales. Calculations predict large increases of the gap and exciton binding energy with decreasing number of layers, as well as a transition of the fundamental gap from direct to indirect for 1 - 2 layers. Results are in reasonable agreement with a simple particle-in-a-box model relying on the Wannier-Mott theory of exciton formation. General arguments and existing data suggest that the Frenkel-like character of the lowest exciton is a common feature of wide-gap layered semiconductors whose effective masses and dielectric constants yield bulk Bohr radii on the order of the layer separation. In addition, experimental observations of exciton mediated multiphonon resonant Raman scattering in few-layer PbI_2 are presented. Results demonstrate that the resonance and overtone scattering strength can be tuned with varying crystal thickness. This is shown to be an effective technique for the characterization of few-layer polar semiconductors such as PbI_2.

CHAPTER 1

Introduction

Layered materials, such as graphene and molybdenum disulfide, have recently been shown to exhibit novel properties in their two-dimensional mono- and few-layer forms. Confinement effects combined with changes in dielectric screening caused by the size reduction results in changes to both the electronic and optical properties of these systems, which can be starkly different from their bulk counterparts. Up until this point, the emphasis in this burgeoning field of atomically thin two dimensional crystals has been on the transition metal dichalcogenides. However, there exists an entire class of similarly layered materials with strong intra-layer bonds and weak van der Waals bonds between the layers, which I refer to as van der Waals (vdW) crystals henceforth. Materials such as graphene, boron nitride, molybdenum disulfide and black phosphorous, just to name a few, are all layered materials with weak inter-layer van der Waals bonds. Individual layers can be isolated from bulk vdW crystals, yielding structures with new and in some cases tunable material properties with layer thickness. These materials have the potential to revolutionize a multitude of electronic and optoelectronic technologies.

The work presented in this thesis involves the study of the layered vdW material lead iodide (PbI_2) by using the mechanical exfoliation technique, also known as the scotch tape peeling method. This method has been widely employed to generate mono- and few-layer samples of other van der Waals crystals and reliably produces mono- and few-layer samples with lateral dimensions on the order of 1 - 5 μm, but often these samples are not

completely uniform and are in contact with thicker areas, sometimes creating measurement challenges. The thickness of these samples has been confirmed through optical contrast measurements as well as with atomic force microscopy measurements. Using such samples we have performed optical experiments including reflection, photoluminescence, and Raman scattering measurements. These experiments have been performed using a lab built micro-optical setup, which allows for white light or laser excitation to be focused down to a spot size of $\sim$ 1-2 μm and reliably positioned on samples of interest. In addition, first-principles calculations have been performed to predict and compare the electronic and excitonic properties in few-layer crystals.

Experimental measurements in addition to theoretical calculations have studied the electronic and optical properties of this material with decreasing thickness down to a monolayer. In particular, our measurements indicate that the excitons in semiconductors like PbI_2, although traditionally treated as Wannier excitons with large radii, are actually Frenkel-like in nature. Our results show that with decreasing thickness, quantum size effects result in an increasing electronic band gap which increases in close proportionality to the expected inverse of the thickness squared. Simultaneously, there is a dramatic enhancement of the exciton binding energy, with the end result that the lowest optical transition shifts very weakly until the thickness is on the order of the bulk exciton radius. Similar effects have been observed in the transition metal dichalcogenides and may be typical of many such layered systems.

In addition, we have demonstrated the ability to use resonant enhancement of scattering from longitudinal optical phonons in few layer samples to measure changes in layer thickness. By using resonant excitation and scattering to identify changes in the exciton energies, we can identify changes in thickness even in atomically thin samples with weak absorption and emission. These results have provided a better understanding of common changes in electronic structure and exciton behavior with decreasing thickness in few-layer semiconductors and pave the way for better understanding and control of the properties in

these structures.

Looking forward, this work should contribute to the ability to controllably engineer the optical response of structures using different few-layer materials with well-defined layer-thicknesses and even potentially stacking arrangements to form complex heterostructures.

CHAPTER 2

Background Theory

This chapter describes the theoretical foundations that are central to the remainder of this thesis. Much of the theory in this chapter has been well developed and is covered more thoroughly in others sources as indicated by the references in each section. For completeness, we briefly summarize some important basic concepts as they are relevant to the subsequent work.

2.1 Van der Waals Crystals

The defining property of vdW crystals, and arguably the most critical, is the van der Waals interactions, which lead to a special form of bonding between layers of the crystal. The reason this form of bonding is so critical, is that the bond is relatively weak, which allows layers to be separated through exfoliation techniques. This property alone has yielded an entire field of research on two-dimensional layered materials. The difference in relative strength of the weak inter-layer bonding between layers versus the stronger intra-layer bonding within the layers creates a unique crystal structure that is particularly conducive to isolating atomically thin single crystals. Various techniques, including a significant amount of work on chemical exfoliation and intercalation [1], have attempted over the years to obtain few-layer samples, but for a long time it was believed that ultra thin crystal lattices were unstable [2]. However, this all changed after Konstantin Novoselov and Andre Geim

demonstrated the ability to isolate single crystalline layers of vdW crystals using a simple mechanical exfoliation technique.

2.1.1 Van der Waals Bonding

To understand why the bonds in vdW crystals are special, it is instructive to consider the relative strength of different types of bonds. It is well known that ionic and covalent bonds are considered to be strong chemical bonds. This is because, in the covalent case, bonds involve the sharing of electrons between atoms. While in the ionic case, bonds are formed by strong Coulomb attraction of positive and negative ions. Van der Waals bonds, on the other hand, are much weaker and to lowest order arise from dipole-dipole interactions of neutral atoms or molecules. In the simplest case of inert atoms, such as noble gases, the time-averaged dipole moment is zero, but fluctuations in the dipole moment of an atom at any given instant can also induce a dipole in nearby atom (see for example Refs. [3, 4] for more detailed discussions). This correlation leads to an attractive force, known as the London or dispersion force, which is offset by a repulsive interaction to account for the Pauli exclusion principle. The potential energy of the total interaction to good approximation can be represented by what is known as the Lennard-Jones potential

$$U(R) = -\frac{A}{R^6} + \frac{B}{R^{12}} \tag{2.1}$$

where R is the distance between the particles and A and B are empirical parameters.

For comparison we consider the energies required to break the different bonds and separate the individual atoms or ions from each other. As an example, the cohesive energies for inert gas crystals held together with van der Waals bonds at low temperatures, e.g. neon, argon, krypton, and xenon, are all in the range of $\approx$ 1 - 15 kJ/mol [3]. In contrast, the lattice energy for the archetypal ionic crystal of sodium chloride (NaCl) is 880 kJ/mol, and typical covalent bond energies in H_2O and SiO_2 are 460 and 370 kJ/mol respectively [4]. Thus we

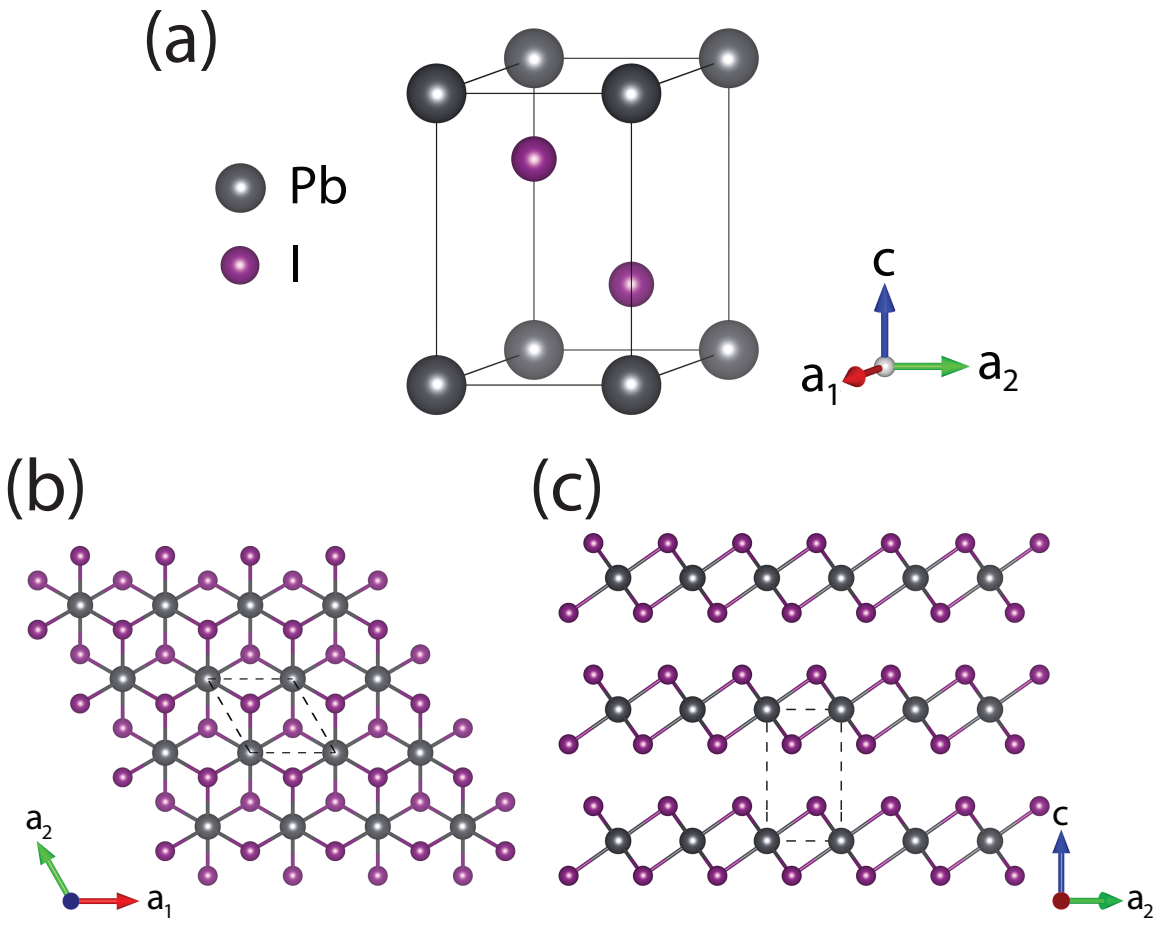

Figure 2.1: A single unit cell of PbI_2 (a) shown beside the unit vectors of the lattice. Crystal structure of PbI_2 shown along the out-of-plane, $\hat{c}$, (b) and in-plane, $\hat{a}_1$ (c) directions with a unit cell depicted by the dotted line.

see that van der Waals bonds can be anywhere from $\approx$ 20 - 100 times weaker than than ionic and covalent bonds.

2.1.2 PbI_2 Crystal Structure

PbI_2 belongs to the class of vdW crystals with attractive van der Waals bonds between its layers. The bonding within its layers, on the other hand, is composed of partially ionic bonds [5, 6, 7] with some debate in the literature as to the relative strength of the ionic and covalent components. A unit cell of PbI_2 is composed of three atoms: one lead and two iodine atoms, as shown in Fig. 2.1 (a). The iodine atoms are octahedrally coordinated

about the lead atoms to form the hexagonal layered structured depicted in Fig. 2.1 (b) & (c) with lattice vectors $a_1 = a_2 = 4.555$ Åand $c = 6.977$ Å[8]. As a result of the ionicity, the Pb-I bonds within the layers are polar bonds.

One feature of layered vdW crystals that must be considered is the formation of polytypes resulting from different stacking orders of the atoms in adjacent layers [8]. The polytype of a given crystal is determined by many growth factors and can be difficult to control or predict. The simplest and most common polytype of PbI_2 is the *2H* polytype with *A B C A B C* stacking [9], as depicted in Fig. 2.1. The second most common polytype is the *4H* polytype, with *A B C B A C* stacking, whose unite cell then includes 2 layers. The bulk crystals received and used in this work were expected to be of the *2H* type.

2.2 Effective Mass Approximation

One of the simplest and most useful approximations in the discussion of semiconductors is the effective mass approximation. For a thorough description see for example Ref. [10]. To understand the behavior of an electron or hole moving in a semiconductor, we must solve the Schrödinger equation for a particle in a idealized crystal with Hamiltonian, H_0, and a screened Coulomb potential, U:

$$(H_0 + U)\Psi(\boldsymbol{r}) = E\Psi(\boldsymbol{r}) \tag{2.2}$$

It is convenient to describe the wavefunction of the electron in real space rather than reciprocal space using Wannier functions, $a_n(\boldsymbol{r} - \boldsymbol{R_i})$,

$$\Psi(\boldsymbol{r}) = N^{-\frac{1}{2}} \sum_{n,i} \Phi_n(\boldsymbol{R}_i) a_n(\boldsymbol{r} - \boldsymbol{R}_i) \tag{2.3}$$

where N is the number of cells in the crystal volume and $\Phi_n(\boldsymbol{R}_i)$ gives the amplitude of each function for a specific band, n, and lattice vector, $\boldsymbol{R}_i$).

Eq. 2.2 is typically solved by employing the effective mass approximation, which assumes that U is a slowly varying function of $\boldsymbol{r}$ and can be expanded to first order about the lattice vector, $\boldsymbol{R}$. In other words, the change in the potential over the space of a single lattice site is assumed to be small such that the potential throughout the crystal can be approximated by the potential at individual lattice sites, $U(\boldsymbol{r}) \approx U(\boldsymbol{R})$, and $\boldsymbol{R}$ can be treated as a continuous variable.

Let us then consider that the electron in question is in the lowest nondegenerate conduction band of a direct gap semiconductor. If the band is approximately parabolic near the minimum, its energy can be described by

$$E(\boldsymbol{k}) = E_0 + \frac{\hbar^2}{2m_e}\boldsymbol{k}^2 \tag{2.4}$$

where E_0 is the energy of the fundamental band gap and the prefactor $\frac{\hbar^2}{2m_e}$ is a fitting parameter for the curvature of the band. It can then be shown that Eq. 2.2 simplifies to:

$$\left[-\frac{\hbar^2}{2m_e}\frac{\partial^2}{\partial \boldsymbol{R}^2} + U(\boldsymbol{R})\right]\Phi(\boldsymbol{R}) \approx [E - E_c]\,\Phi(\boldsymbol{R}) \tag{2.5}$$

This equation can be understood as describing the envelope function, $\Phi(\boldsymbol{R})$, of an electron moving in a crystal with effective mass, m_e. It is important to note that U must be a weak and slowly varying potential for the approximation to truly be valid.

2.3 Excitons

It is well established, that radiation with sufficient energy incident on a semiconductor can excite an electron above the band gap from the top valence band to the lowest conduction band. The behavior of the remaining valence electrons is then modeled by a positively charged hole left behind by the excited electron. The electron and hole behave independently according to the band structure of a given material, but some properties, in particular

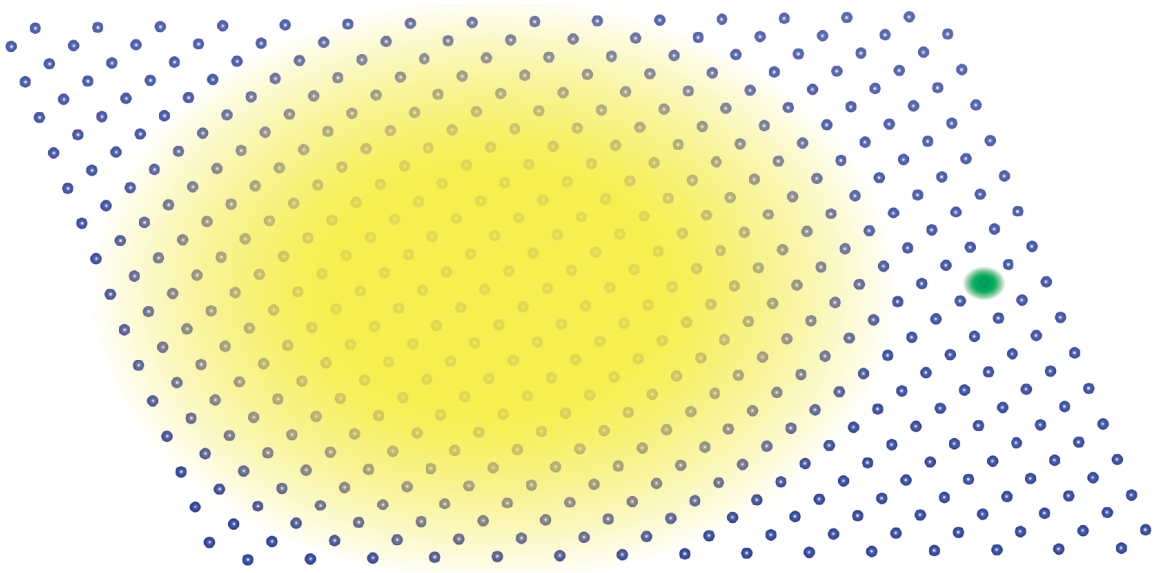

Figure 2.2: Schematic representation of the electron distribution for a Wannier-Mott (yellow) and Frenkel exciton (green) drawn for a slice of crystal.

the absorption profile, are strongly modified by the Coulomb interaction between the electron and hole. This interaction is accounted for with electron-hole quasiparticles, termed excitons, which are divided into two archetypal forms, tightly bound Frenkel excitons and weakly bound Wannier-Mott excitons. A schematic representation of these two extreme limits is shown in Fig. 2.2. For a complete derivation of these cases see Ref. [11]. In the following sections we expand upon these two limiting cases.

2.3.1 Frenkel Excitons

Frenkel excitons describe the limiting case whereby the separation between the bound electron and hole pair is on the order of a single atom or lattice site. A nice discussion can be found in Refs. [3, 12]. This type of exciton is akin to a mere excited atom within a lattice of atoms for which for a single electron excitation can be described by the wavefunction

$$\Phi_n(\boldsymbol{r}_1, \ldots, \boldsymbol{r}_N) = \phi_e(\boldsymbol{r}_n) \prod_{m \neq n} \phi_g(\boldsymbol{r}_m) \tag{2.6}$$

where ϕ_g and ϕ_e represent the ground and excited states of the individual atoms. The Hamiltonian for this system contains an interaction term accounting for the Coulomb interaction between the electrons of different atoms, which to lowest order results in an energy dispersion of the form [12]

$$E(\boldsymbol{K}) = E_0 + \sum_m D(\boldsymbol{R}_m) e^{-i\boldsymbol{K}\cdot\boldsymbol{R}_m} \tag{2.7}$$

where $\boldsymbol{R}_m$ is the position of the m^{th} atom and $\boldsymbol{K}$ is the wavevector of the exciton. This excitation can thus propagate throughout the crystal by means of hopping from one lattice to the next. The hopping mechanism is a result of the dipole-dipole interaction $D(\boldsymbol{R}_m)$ between atoms and leads to the formation of an energy band as a function of wavevector in the crystal. A nice toy-model example of this band formation can be found in Ref. [3]. Frenkel excitons have been observed and are well known in the large band gap alkali halide crystals as well as in molecular crystals where individual molecules are weakly bonded by van der Waals forces.

2.3.2 Wannier-Mott Excitons

The model associated with the vast majority of semiconductors is the Wannier-Mott exciton model. Continuing with the formulation in Ref. [10], this model assumes the validity of the effective mass approximation and treats the electron and hole as particles with masses determined by their respective bands. It is illustrative to consider the effect of excitons in an idealized model at the band edge of a direct gap semiconductor. Once again, treating the highest valence and lowest conduction bands as nondegenerate isotropic and parabolic near their minima, we obtain:

$$E_e(\boldsymbol{k}_e) = E_0 + \frac{\hbar^2 k_e^2}{2m_e} \tag{2.8a}$$

$$E_h(\boldsymbol{k}_h) = \frac{\hbar^2 k_h^2}{2m_h} \tag{2.8b}$$

The exciton wavefunction utilizing Wannier functions for both the electron and hole is then given by:

$$\Psi(\boldsymbol{r}_e, \boldsymbol{r}_h) = N^{-1/2} \sum_{\boldsymbol{R}_e, \boldsymbol{R}_h} \Phi(\boldsymbol{R}_e, \boldsymbol{R}_h) a_{\boldsymbol{R}_e}(\boldsymbol{r}_e) a_{\boldsymbol{R}_h}(\boldsymbol{r}_h) \tag{2.9}$$

The Schrödinger equation, Eq. 2.2, thus takes the form:

$$\left[-\frac{\hbar^2}{2m_e} \nabla^2_{\boldsymbol{R}_e} - \frac{\hbar^2}{2m_h} \nabla^2_{\boldsymbol{R}_h} - \frac{e^2}{\varepsilon_0 |\boldsymbol{R}_e - \boldsymbol{R}_h|} \right] \Phi(\boldsymbol{R}_e, \boldsymbol{R}_h) = E \Phi(\boldsymbol{R}_e, \boldsymbol{R}_h) \tag{2.10}$$

If the exciton motion is separated into the motion of the center of mass, $\boldsymbol{R}$, and the relative motion of the electron and hole, $\boldsymbol{r}$, then the Schrödinger equation simplifies to two equations:

$$-\frac{\hbar^2}{2M} \nabla^2_{\boldsymbol{R}} \psi(\boldsymbol{R}) = E_R \psi(\boldsymbol{R}) \tag{2.11}$$

$$\left[-\frac{\hbar^2}{2\mu} \nabla^2_{\boldsymbol{r}} - \frac{e^2}{\varepsilon_0 r} \right] \phi(\boldsymbol{r}) = E_r \phi(\boldsymbol{r}) \tag{2.12}$$

where M and μ correspond to the total and reduced masses. Eq. 2.11 is just the equation for a free particle with wavevector $\boldsymbol{K}$ and kinetic energy $\hbar^2 K^2 / 2M$. Eq. 2.12, on the other hand, is identical in form to the equation for the hydrogen atom. The only differences being that the Coulomb potential is screened and the reduced mass appears in this case because the electron and hole masses are comparable. Solving this equation in the same way as the hydrogen problem yields the energy states of the exciton with quantum numbers n, l and m:

$$E_{nlm} = E_0 + \frac{\hbar^2 K^2}{2M} - \left(\frac{\mu e^4}{2\hbar^2 \varepsilon_0^2} \right) \frac{1}{n^2} \tag{2.13}$$

where the term in parentheses is known as the exciton Rydberg constant, R^* and ε_0 is the static dielectric constant. Thus these excitons display a series of hydrogenic states at energies below the band gap by an amount known as the binding energy.

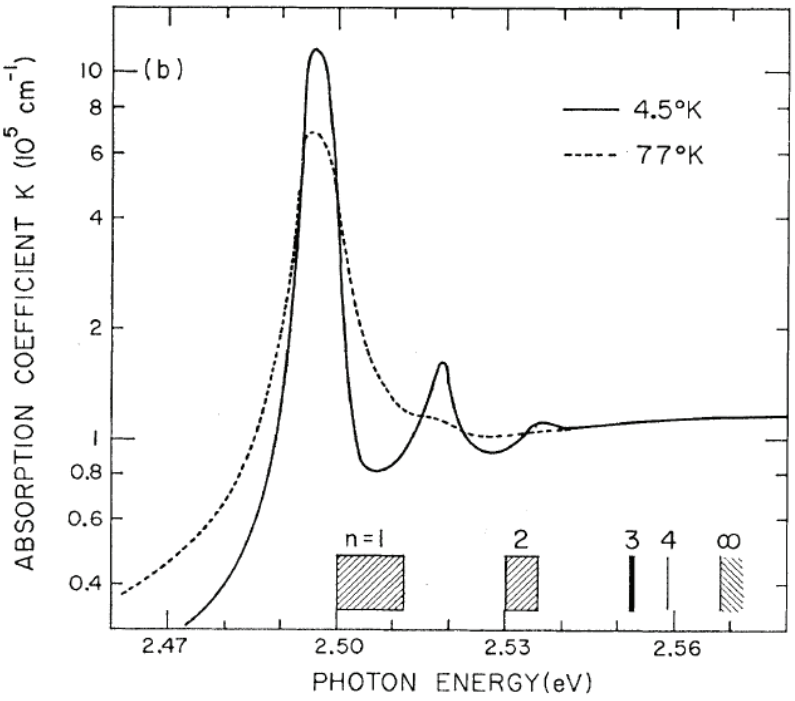

Figure 2.3: Absorption spectrum as a function of energy obtained from Kramers-Kronig analysis of reflectivity measurements on bulk PbI_2 at 4.5 and 77 K from [13].

2.3.3 Exciton Absorption

The effect of excitons is most apparent in the absorption near the fundamental band gap of a semiconductor. It can be shown that bound Wannier exciton states modify the form of the imaginary part of the dielectric function as [10]

$$\varepsilon_i(\omega) = \frac{8\pi \left|\langle c| \hat{\boldsymbol{e}} \cdot \boldsymbol{p} |v\rangle\right|^2 \mu^3}{\omega^2 \varepsilon_0^3} \sum_n \frac{1}{n^3} \delta(\omega - \omega_n) \tag{2.14}$$

which produces a series of absorption peaks at the energies of the hydrogenic series, ω_n, that decrease in strength as $\sim 1/n^3$. Once converted to a real and imaginary index of refraction, $\tilde{n} = n + i\kappa$, the absorption is defined as:

$$\alpha = \frac{4\pi\kappa}{\lambda_0} \tag{2.15}$$

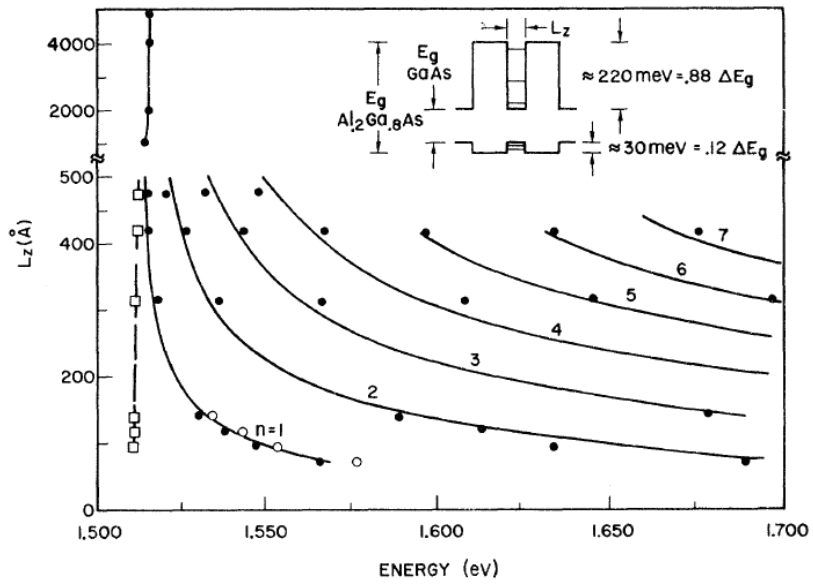

Figure 2.4: Exciton energies extracted from absorption measurements in $Al_{0.2}Ga_{0.8}As$-GaAs quantum wells as a function of thickness from [18]. n values indicate the quantized electronic transitions in the wells.

which exhibits the corresponding hydrogenic series form of the permittivity.

The absorption profile of bulk PbI_2 exhibits such an excitonic series at its band edge, and up to the n = 4 state of the exciton has been confirmed experimentally with some evidence of higher peaks[14, 13, 15]. A fit using the hydrogenic model with a Rydberg energy of 0.127 eV is in excellent agreement to all but the lowest $n = 1$ peak exciton peak energy, and predicts a band gap of 2.552 eV [13]. The lowest energy peak is shifter to higher energy by 0.072 eV for a binding energy of 0.055 eV, and this shift is attributed to a repulsive central cell correction [16], which is very similar to the case of MoS_2 [17].

2.4 Quantum Wells

Due to their anisotropy, few-layer crystals are similar in many ways to quantum wells. There is a vast literature on semiconductor quantum wells, and a good survey can be found in Ref. [19]. Much of the fundamental quantum well work has been performed using

gallium arsenide quantum wells grown with lattice matched aluminum gallium arsenide barriers [20]. It is well known that the energy levels of a particle in an infinite square well are given by

$$E_n = E_0 + \frac{\hbar^2 \pi^2 n^2}{2ml^2} \tag{2.16}$$

where l is the well width. This $1/l^2$ dependence has been demonstrated experimentally in $Al_xGa_{1-x}As$-GaAs in the work of Dingle [18], which is shown in Fig. 2.4. Those results obtained from absorption measurements show the energies of the lowest excitonic states for the first seven electronic levels as a function of well width. Dingle et al. extracted a binding energy increase from 4 to 7 meV from their data. Similar results with confinement could be expected to be observed in natural quantum wells formed from few-layer van der Waals crystals, however as we demonstrate later, the material properties in these quantum wells are very different.

2.5 Raman Scattering

Raman scattering is a useful tool for the study of lattice vibrations in crystals that is well documented in the literature. Reviews of the theory and methods can be found in Refs. [10, 22]. We briefly mention the role of selection rules in scattering here. The scattered light intensity can be shown to be proportional to

$$I_s \propto |\hat{\boldsymbol{e}}_{\boldsymbol{i}} \cdot R \cdot \hat{\boldsymbol{e}}_{\boldsymbol{s}}|^2 \tag{2.17}$$

where R is the Raman tensor and the $\hat{\boldsymbol{e}}_{\boldsymbol{i,s}}$'s are the incident and scattered polarizations. The Raman tensors for various crystal systems are given in Ref. [23]. PbI_2 belongs to the trigonal crystal system and the D_{3d} class. In addition, it has inversion symmetry, which means the odd parity modes are raman inactive but IR active and the even parity modes Raman active. A Raman spectrum for bulk PbI_2 is shown in Fig. 2.5, which displays the

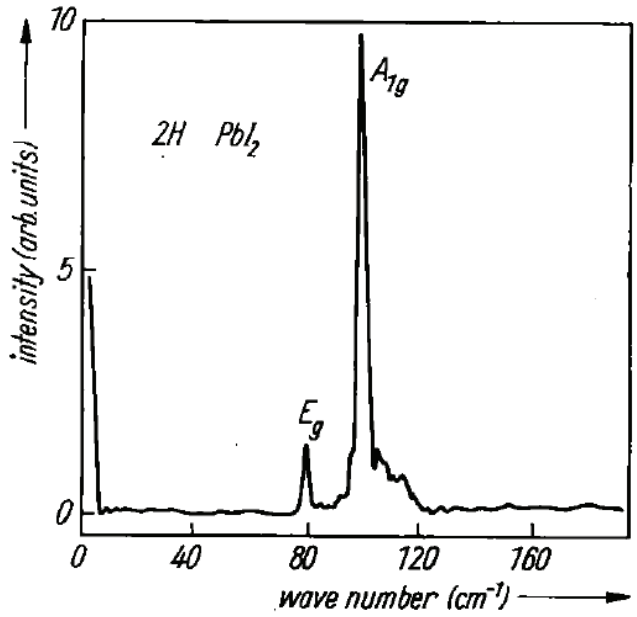

Figure 2.5: Raman spectrum taken on bulk 2H PbI_2 at 4.2 K using a 532 nm source from Ref. [21].

Raman active E_g and A_{1g} phonon modes. The broad peak between 100 - 120 cm^{-1} is attributed to weaker second order scattering due to scattering by two phonons.

2.5.1 Resonant Raman Scattering

We also briefly mention the conceptual basis for resonant Raman scattering which leads to scattering enhancements near electronic resonances. The Raman scattering in a material can be described by its differential scattering cross-section. According to Ref. [24] Section 3.1, this cross-section for an incident photon, with wavevector $\boldsymbol{k}_1$ and energy $\hbar\omega_1$, scattered to a photon, with $\boldsymbol{k}_2$ and $\hbar\omega_2$, can be represented by:

$$\frac{d\sigma(\boldsymbol{k}_1, \omega_1; \boldsymbol{k}_2, \omega_2)}{d\Omega} = \frac{1}{4\pi^2\hbar^2c^4} \sum_f |K_{2f,1g}|^2 \left(\hbar\omega_1 - E_f\right)^2 \tag{2.18}$$

where E_f is the final state of the material and $K_{2f,1g}$ contains the matrix elements linking the ground state g to the final state f. The cross section must be summed over all the final

states that contribute to the scattering.

If we consider a Stokes scattering process near resonance, then the lowest order contribution to the matrix element K can be written as:

$$K_{2f,1g} \approx \sum_i \frac{\langle \omega_2 f | \, H_{MR} \, | 0i \rangle \, \langle 0i | \, H_{MR} \, | \omega_1 g \rangle}{\hbar\omega_1 - E_i - i\Gamma_i} \tag{2.19}$$

where the interaction Hamiltonian between matter and the radiation field, denoted H_{MR}, couples the system from its ground state to its final state through an intermediate state i. The imaginary term with energy Γ_i accounts for the lifetime of the intermediate states. It should be clear from this form, that a resonance with a Lorentzian form exists when $\hbar\omega_1 \approx E_i$. However, it is also important to note that because the matrix elements in Eq. 2.19 are complex, interference effects can occur in the final cross-section when squaring the sum over multiple states. Here the sum is performed over all contributing intermediate states, and if the intermediate state interactions are treated as constant, the expression can be simplified into different forms depending on the nature of the intermediate state (see [24] Section 3.2 for more details).

To understand the role of excited quasi-particles in a material, the intermediate state interactions must be explicitely included into the matrix elements through the material Hamiltonian. Since we are interested primarily in the quasi-particle interaction through phonons, we consider only a quasi-particle interaction Hamiltonian H'_M. This interaction is treated as a perturbation because such quasi-particles are not true eigenstates of the system. To first order this gives:

$$K_{2f,1g} = \sum_{i,j} \frac{\langle f | \, H_{MR} \, | j \rangle \, \langle j | \, H'_M \, | i \rangle \, \langle i | \, H_{MR} \, | g \rangle}{(\hbar\omega_1 - E_i - i\Gamma_i)\,(\hbar\omega_2 - E_j - i\Gamma_j)} \tag{2.20}$$

where it is assumed a phonon is created between intermediate states i and j. We see now that for single pair of intermediate states i and j, there will be an incoming resonance at $\hbar\omega_1 \approx E_i$ as well as an outgoing resonance at $\hbar\omega_2 \approx E_j$. Again, one must sum over all

contributing intermediate states, and depending on the nature of these states, the resonances in Eq. 2.20 can take on modified forms.

2.5.2 Fröhlich Interaction

It is also known that near an M_0 type band gap, the Fröhlich interaction contributes strongly to the scattering intensity [24]. As such, we consider briefly here the form of the Fröhlich term in the Hamiltonian for a phonon mode ν interacting with an electron. To first order the Hamiltonian takes the form [24]:

$$H'_M = \frac{1}{V^{1/2}} \left[\frac{\gamma_\nu}{q} e^{i\boldsymbol{q}\cdot\boldsymbol{r}} b_\nu + \frac{\gamma_\nu}{q} e^{-i\boldsymbol{q}\cdot\boldsymbol{r}} b_\nu^\dagger \right] \tag{2.21}$$

where V is the volume of the crystal, γ_ν is a coefficient describing the strength of the longitudinal electric field accompanying phonon mode ν, and b_ν ($b_\nu^\dagger$) is the phonon annihilation (creation) operator.

Near zone center, for $q \approx 0$, the Fröhlich term can be expanded as

$$\frac{\gamma_\nu}{q} e^{i\boldsymbol{q}\cdot\boldsymbol{r}} = \frac{\gamma_\nu}{q} \left[1 + i\boldsymbol{q}\cdot\boldsymbol{r} - (\boldsymbol{q}\cdot\boldsymbol{r})^2 + \dots \right] \tag{2.22}$$

The first term in the expansion is canceled out when the electron and hole contributions are summed together. The linear term is independent of q and corresponds to an interband electrooptic contribution. Finally the important term for this discussion is the third term, which results in a linear dependence on q and does not cancel for electon and hole. This term results in a strong wavevector dependence with a strong contribution near the band edge of polar crystals.

CHAPTER 3

Experimental Methods

This chapter presents the experimental techniques used in the preparation and study of atomically thin exfoliated PbI_2 samples.

3.1 Few-Layer Sample Preparation

Bulk PbI_2 crystals were grown using the Bridgman-Stockbarger technique by Professor Marie Matuchová's group at the Czech Technical University in Prague. Samples were identified as predominantly belonging to the *2H* polytype from X-ray diffraction and electron backscatter diffraction techniques. For more details on the growth process see Ref. [25]. Samples used in this work were hand cleaved from bulk grown ingots yielding bulk lamellar crystals. Few-layer samples were then prepared from these bulk crystals using the mechanical exfoliation technique, also known as the scotch tape method, which was first employed in a slightly more complicated fashion to isolate monolayer graphene [26]. Variations on this technique, in one form or another, have been shown to be capable of isolating monolayers of a number of different vdW crystals [1], which can then be identified relatively easily on a silicon substrate with an appropriate oxide surface layer. While the technique is relatively simple, it has proved to be effective in yielding mono- and few-layer crystals and is capable of producing them at almost every attempt.

The first step in our process is to prepare the substrates. Large 4 inch diameter silicon wafers with a 90 or 285 nm oxide surface layer were purchased online from www.graphene-

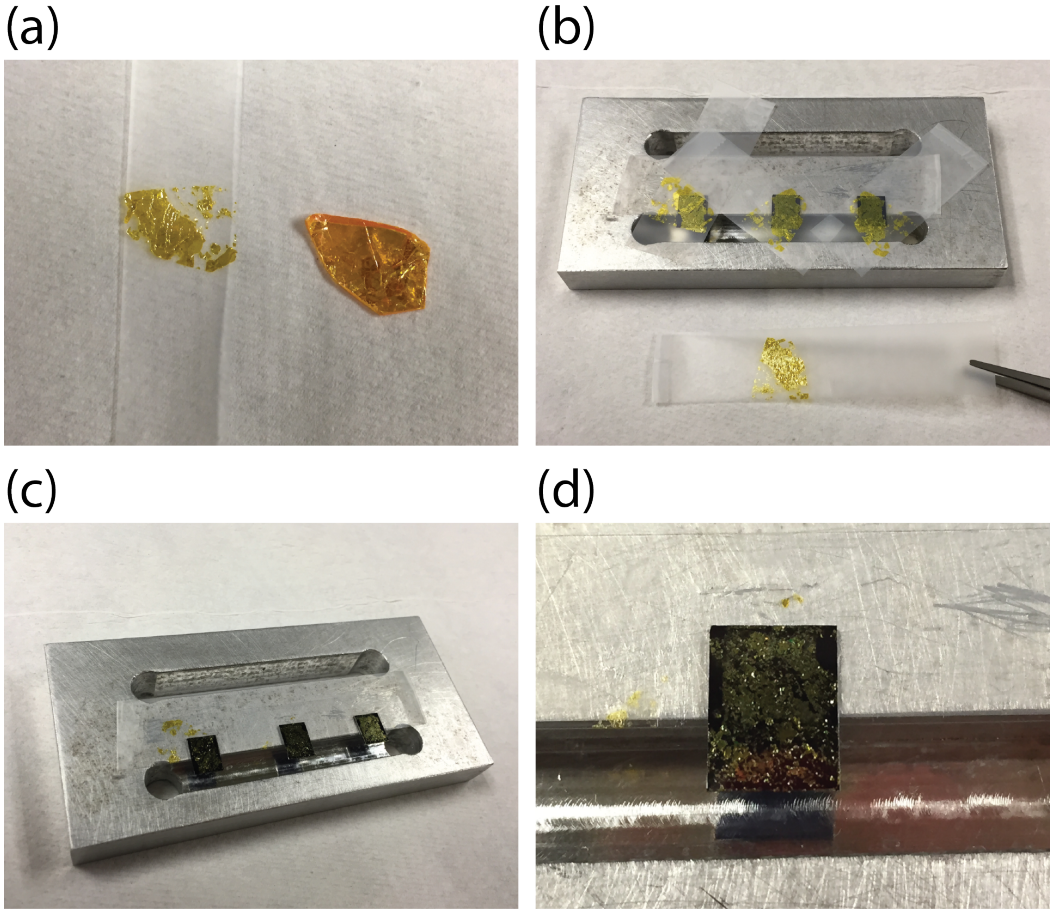

Figure 3.1: Images of the mechanical exfoliation process.

supermarket.com. These wafers were then cleaved by hand along lines inscribed on the oxide surface using a standard diamond scribe. The wafers were easily cleaved to specification by placing the wafer on a solid block with the inscribed line directly above the edge. By holding the wafer in place and putting pressure on the overhanging area, the wafer generally cleaved directly along the line. In this way, individual substrates with dimensions $\sim$ 5 x 10 mm were prepared. These dimensions were chosen to fit one or two substrates within the space of a cryostat window, and to allow translation across the entire sample using a standard 0.5 inch linear translation stage. Once prepared, the substrates were mounted on a metal holder using double sided tape and the surface of each substrate was cleaned by hand. This was done using standard lens cleaning techniques with lens tissue and a combination of methanol and acetone. After wiping the surfaces, they were inspected under a microscope to ensure there was no residue on the surface. Acetone was usually found to be better for this, with methanol sometimes leaving visible streaks on the surface.

The next step is to exfoliate the crystals. This process is depicted in Fig. 3.1, and is performed while wearing nitrile gloves to avoid directly contaminating the samples. First, a bulk crystal is placed and then gently pressed down on to a long piece of tap laid down with its sticky side up. Using tweezers the crystal is then slowly pulled off of the tape leaving behind some material as shown in Fig. 3.1 (a). Additional pieces of tape can be laid sticky side down on to the original strip to peel off some material for multiple substrates. The individual strips of tape can then be repeatedly folded closed and pulled apart to thin down the attached material. After a few repetitions, an area of the tape is selected and pressed face down on to a mounted substrate, shown in Fig. 3.1 (b). It can be helpful to gently rub the back of the tape making sure the material comes into good contact with the surface and depositing crystals on to the wafer. If done successfully, when the tape is pulled off, the substrate should be covered with crystals ranging from millimeters to nanometers in size as seen in Fig. 3.1 (c,d). There is no exact recipe to obtain large high quality few-layer samples, however, based on experience there are certain guidelines that

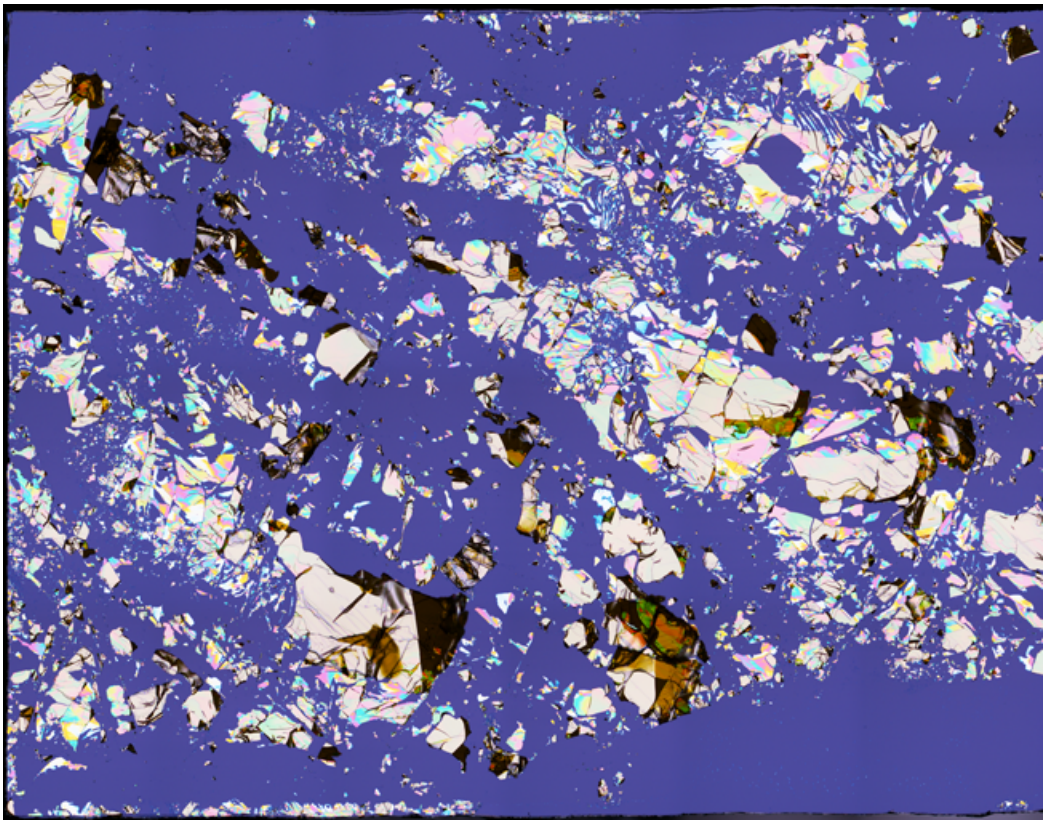

Figure 3.2: Full image of a substrate with exfoliated PbI_2 stitched together from separate microscope images obtained with at 10x objective. Images like this one were used as a map to locate individual areas of interest for experiments.

give very reproducible results. Most importantly, if the material is peeled too many times, giving the appearance of a uniformly coated area on the tape with no clear crystalline form, the crystals deposited on the substrate will tend to be too small to measure optically. Conversely, if the material is not peeled enough times, the deposited crystals tend to be hundreds of microns in lateral size but mostly very thick. There is happy medium from which there tends to be an intermediate range of large and small samples, and very often one can find few-layer samples protruding at the edges of some of these larger samples.

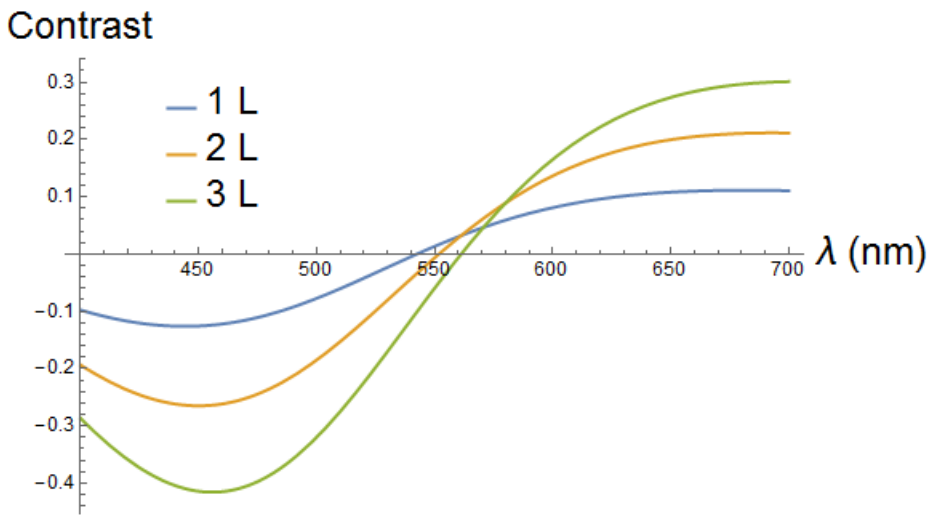

Figure 3.3: Optical contrast calculations for 1, 2 and 3 layers of material with refractive index $n = 3$ on a silicon substrate with a 90 nm oxide layer.

3.2 Optical Imaging

Once the samples have been deposited on the silicon and silicon dioxide substrates, they can readily be identified under an optical microscope as seen in Fig. 3.2. Deposited samples can broadly be broken down into three categories based on their thickness and their visual appearance. The first category corresponds to the thickest samples, $\gtrsim 1$ μm, which are the largest crystals with a beige-like color. The second category corresponds to samples with thicknesses down to ~ 50 nm and smaller lateral dimensions, which display a variety of different colors based on their thickness. Finally, the thinnest samples, $\lesssim 50$ nm, display as shades of blue becoming darker with decreasing thickness and are typically $\lesssim 10$ μm in size.

Despite being almost completely transparent, mono- and few-layer areas can still be faintly visualized. This is because when viewed under illumination from above, the reflections at each interface as well as the phase shifts induced as the light passes through each layer, combine to create an optical contrast with respect to the bare substrate [27]. This can be shown by calculating the optical contrast between the bare substrate and the substrate

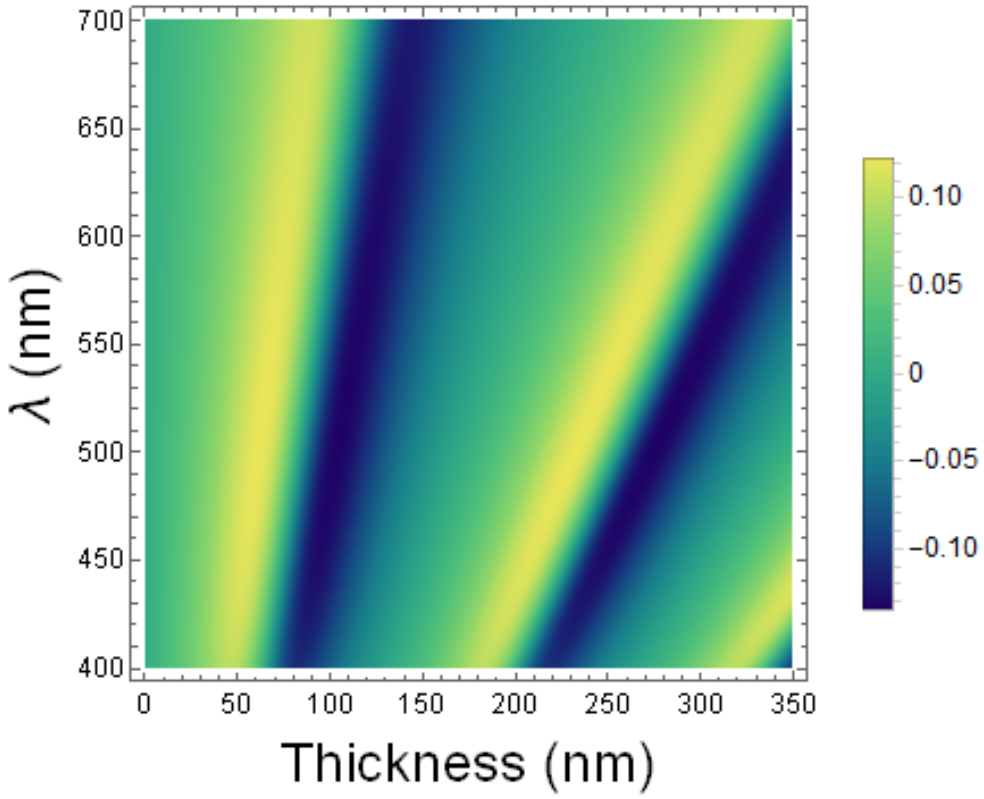

Figure 3.4: Density plot of the optical contrast calculated for a range of oxide thicknesses. Calculations were performed for a monolayer of material with refractive index $n = 3$.

with a layer of material on it of refractive index n, $\frac{I_{sub}-I(n)}{I_{sub}}$. It is apparent from Fig. 3.3, where the contrast has been calculated for 1, 2 and 3 layers of material with a real refractive index of $n = 3$, that even a monolayer of material should be visible. The choice of substrate was critical in the initial work demonstrating the ability to isolate two-dimensional crystals [1] because it allowed atomically thin samples to be identified fairly rapidly amidst a plethora of thicker crystals. It is important to note however, that the choice of oxide thickness is critical in maximizing the contrast. Figure 3.4 shows that oxide thicknesses of ≈ 90 and 285 nm provide optimal contrast around a wavelength of sim 550 nm, corresponding to the most sensitive spectral region of the our eyes.

Calculations such as those presented in Figs. 3.3 & 3.4 performed for graphene and boron nitride [27, 28] are in good agreement with experiments, and as a result, oxide thicknesses of 90 and 285 nm have become standard for two-dimensional materials. However, these are special cases because the optical constants vary minimally over the visible spectrum. This is not the case for PbI_2, for which it is difficult to predict the optical constants in few-layer samples, and contrast calculations presented here were done using a real refractive index of $n = 3$ [29]. Including the imaginary part of the index changes the exact form of the contrast below 500 nm, but the result that there is a finite contrast for few-layer crystals is unchanged. Optical images of few-layer samples and their corresponding atomic force microscopy images, such as those presented in Fig. 3.5 confirm the ability to identify such atomically thin samples visually.

3.3 Atomic Force Microscopy

While few-layer samples can be identified optically, it is difficult to confirm their thickness visually. Thus, atomic force microscopy (AFM) is used as method to probe the thickness of crystals more directly. This is done by bringing a sharp cantilever tip in to contact with the surface and then raster scanning it across an area of interest, which can in theory measure

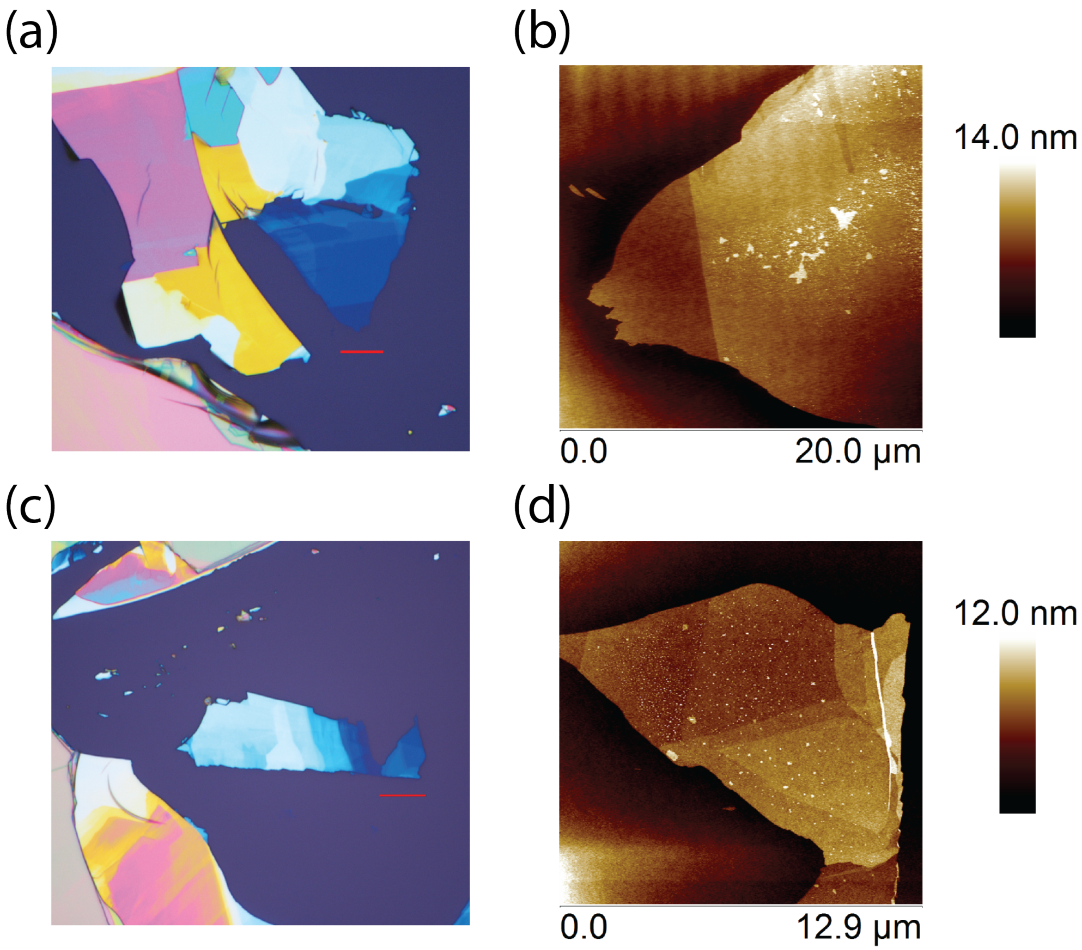

Figure 3.5: (a,c) Optical microscope images of PbI_2 samples under white light illumination with a 50x objective. Red scale bars are equal to a distance of 10 μm. (b,d) Corresponding AFM images of few-layer areas.

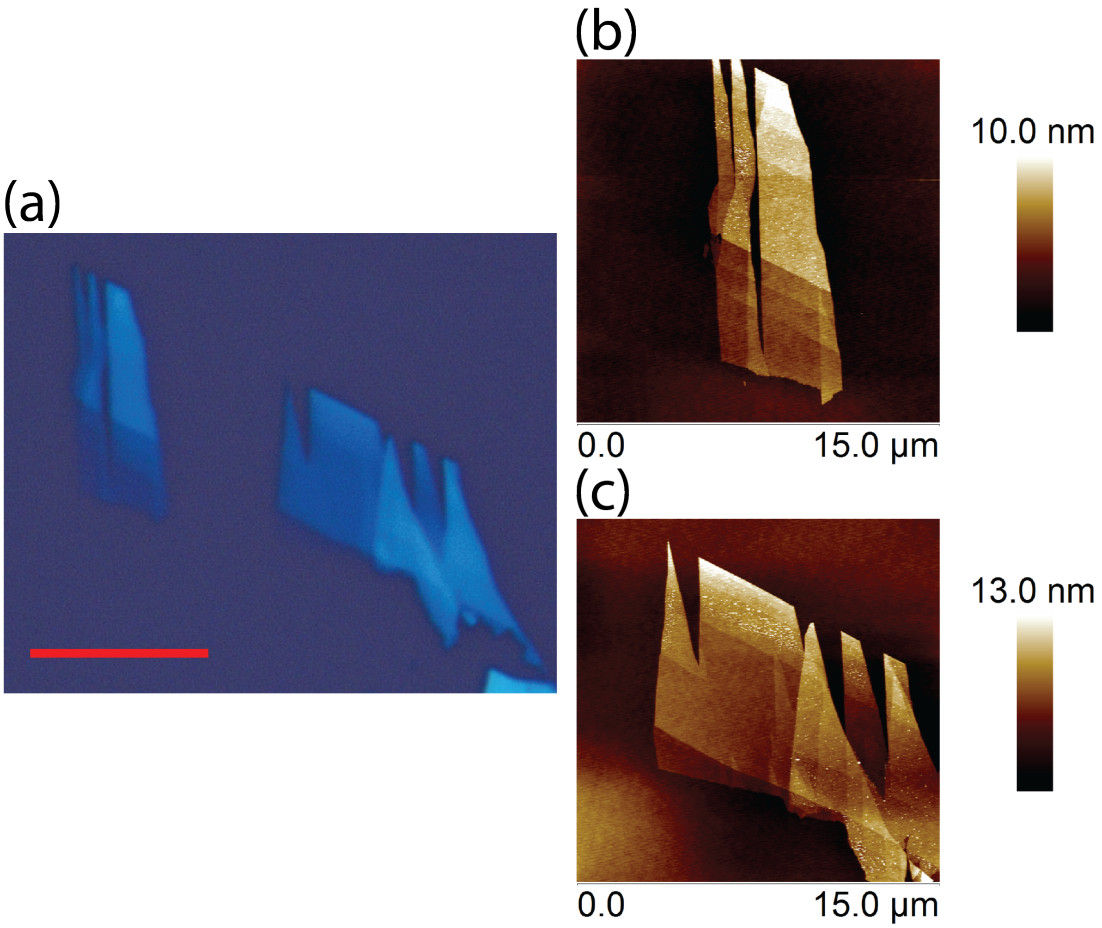

Figure 3.6: (a) Optical microscope image of few-layer PbI_2 crystals under white light illumination with a 100x objective. The red scale bar corresponds to a distance of 10 μm. (b,c) Corresponding AFM height images of the samples shown in (a).

height changes less than a nanometer. AFM measurements were performed on a Bruker Dimension Icon AFM in the Electron Microbeam Analysis Laboratory at the University of Michigan's North Campus Research Complex. Bruker's proprietary ScanAsyst imaging mode was used, which employs a special form of tapping known as PeakForce Tapping mode. Rather than just tapping a the cantilever across the surface at a resonant frequency as in traditional tapping mode, PeakForce Tapping oscillates below resonance to obtain force curves relative to the height of the cantilever at each pixel. ScanAsyst in turn, uses a feedback loop to optimize the various scan parameters automatically. A more thorough description of the different modes can be found in the documentation on Bruker's website [30]. In addition, Bruker's SCANASYST-AIR probes were used as the cantilevers, and a new tip was used every time. AFM measurements were done on all samples but only after optical experiments had been performed so as to avoid any potential contamination or damage to the samples.

Figure 3.6 shows both optical and AFM images taken of few-layer samples. The AFM images, whose false colors are given by the height of the tip, are consistent with the optical images, and actually show the thinnest samples more clearly. Typically AFM scan areas were carefully chosen due to certain constraints of the instrument. One limitation of AFM is that it works best over very small areas, generally less than a few micrometers. This is apparent in Fig. 3.6 (c) where there is some bowing in the image due to the large scan area. Some of this can be corrected in post-processing using plane-fitting options, which was sometimes done on a case by case basis, but usually with limited improvement. Another issue is the difficulty in imaging areas with large variations in step height. Not only do the large steps saturate the resulting image, but it is difficult to actually measure anything accurately near the edge of a large step. Thus whenever possible, smaller scans were done and isolated fairly uniform areas were selected.

In addition, there are a number of challenges in using an AFM to accurately characterize the height of few-layer samples. Despite an interlayer distance of ≈ 0.34 nm in bulk

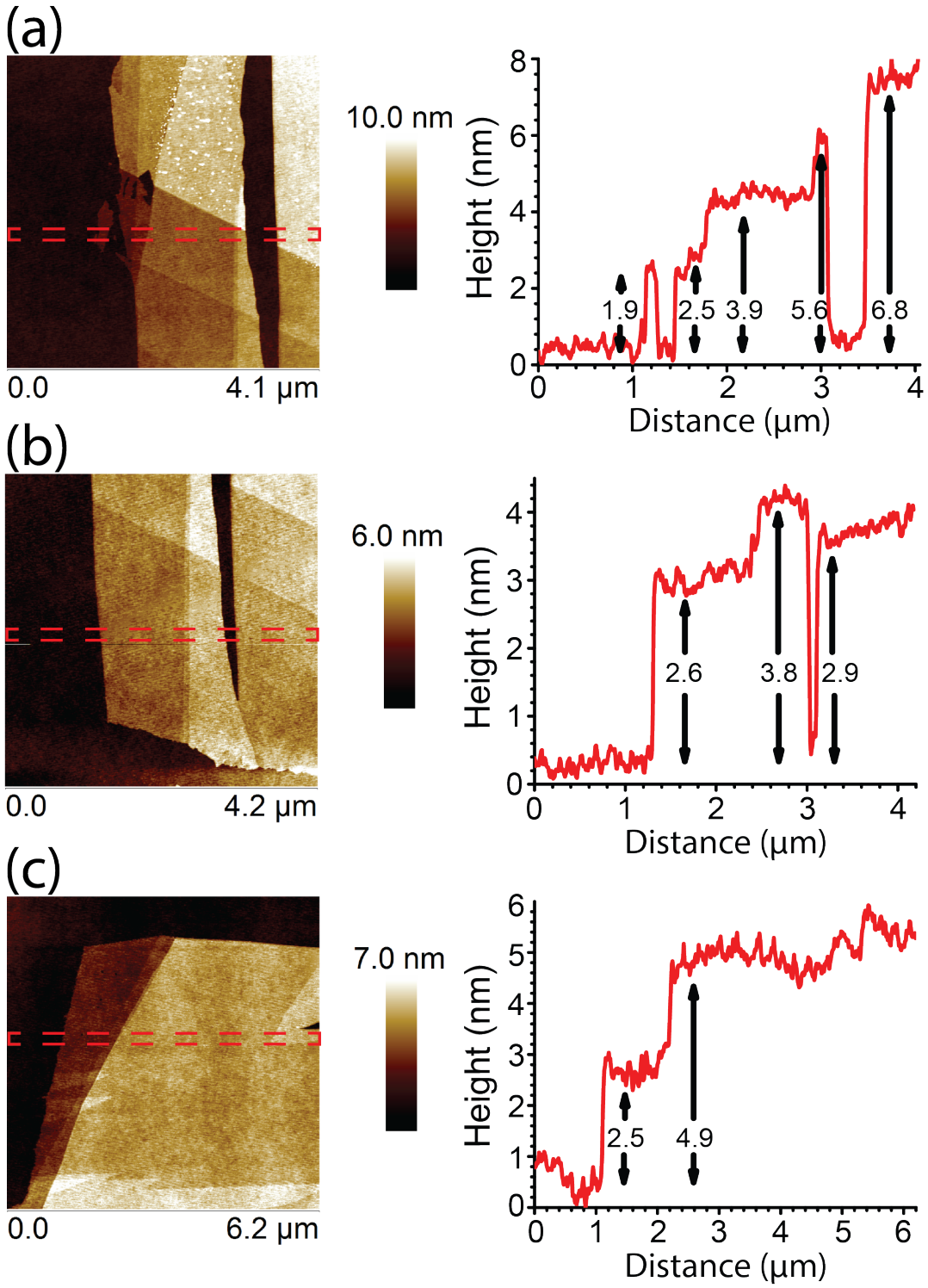

Figure 3.7: Zoomed in AFM images of the samples shown in Fig. 3.6. The plots on the right side of each image correspond to a averaged line traces over the areas demarcated by red dotted lines in the images.

graphite, Novoselov et al. reported apparent AFM thicknesses of 1 - 1.6 nm for measurements on graphene samples in their initial work [26]. Two primary factors were found to contribute to this overvaluation. The first is an adsorbed layer of water on the substrate surface which can become trapped between the crystal and surface creating a "dead layer", which varied in thickness but was close to $\approx$ 1 nm. The second factor is the difference in interaction of the tip of the cantilever with the substrate and the material. Similar effects were observed for AFM measurements of few-layer PbI_2. Ideally some of these effects may be accounted for by carefully selecting the type of tip used and the instrument parameters and setpoints to obtain more accurate heights. Measurements on graphene showed that by varying certain setpoints it was possible to obtain more accurate measurements as well as large variations of $\sim$ 1 - 2 nm [31]. The AFM measurements performed here were done in air using standard ScanAsyst settings and tips, which produced reasonable and consistent results. Example line traces used to determine sample thicknesses are shown next to the corresponding images in Fig. 3.7. Each line trace is averaged over the region enclosed by the dotted red lines in the images. The line traces and the associated heights are representative of typical samples. The thinnest flakes with the lowest optical contrast produced height measurements of $\approx$ 2 - 2.5 nm. These values are large compared to the bulk interlayer spacing of 0.7 nm. However, steps measured from one PbI_2 area to slightly thicker area produced heights equal to integral multiples of $\approx$ 0.6 - 0.7 nm. Therefore, it is safe to assume that a similar "dead layer" exists between the samples and the surface, which combined with the contrasting tip interactions, leads to an overestimation of the sample thicknesses. We therefore assume that samples with thicknesses measured to be $\lesssim$ 2.5 nm correspond to 1 - 2 layers of PbI_2. The thickness of samples in contact with these thinnest layers can then easily be deduced using the bulk interlayer spacing. The number of layers composing much thicker samples was estimated by subtracting an approximate dead layer thickness and dividing by the interlayer spacing.

We also note that many of the samples do not lie flat on the substrate. As is clear for the

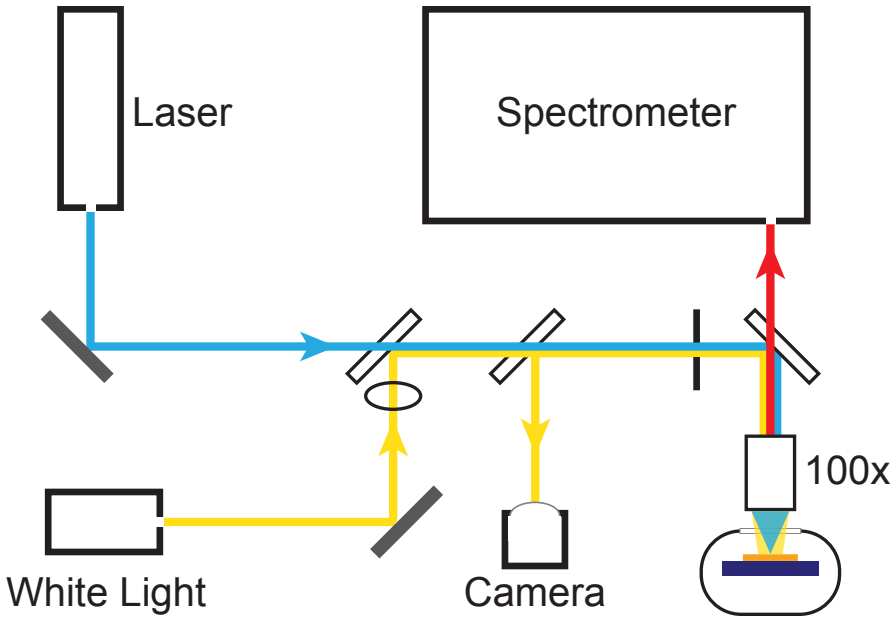

Figure 3.8: Schematic drawing of the experimental setup used for PL measurements.

line traces, there is often a slope, and measurements must be made close to edges. Finally, while we rarely observe pleats or folding such as those seen in graphene, we do observe some rippling in the samples, particularly apparent in the image in Fig. 3.7 (c). These effects must all be taken into account when determining layer thickness. In the rest of this thesis, we therefore assume the error in the layer thickness of the thinnest few-layer sample to be $\pm$ 1 layer, while for thicker samples, it is assumed to be $\pm$ 2 layers.

3.4 Experimental Setup

This section describes the experimental setup and equipment used for PL, Raman and reflection measurements of few-layer PbI_2 samples. The basic layout of the experimental setup for PL and Raman measurements is shown in Fig. 3.8. The setup for reflection measurements was effectively the same, but modified slightly to incorporate a reference measurement of the incident illumination for longer measurements. There are two incident light paths in Fig. 3.8; one path is for the laser excitation, and the other is for white light

illumination of the samples. There are also two light detection paths; one is for sample visualization using a video camera and the other is for collection of the emitted, scattered and reflected light directed into a spectrometer.

Experiments were done in a backscattering geometry, and a beamsplitter was used to reflect the incident light in to the path of the objective, while letting the outgoing light pass through to the spectrometer. Due to the micrometer sized samples, a long working distance microscope objective was used to both focus the incident light on areas of interest and collect the backward propagating light. Initial measurements, including the reflection measurements presented later, were performed using a 50X Mitutoyo plan apochromatic infinity-corrected super long working distance objective with a 20.5 mm working distance and a 0.42 numerical aperture, which produced a laser spot size of ≈ 5 μm. To obtain a tighter spot size and better signal collection, a shorter working distance and larger magnification objective was purchased and used to collect most of the PL and Raman data presented in this work. This was a 100X Mitutoyo plan apochromatic infinity-corrected long working distance objective with a 6 mm working distance and a 0.7 numerical aperture, which resulted in a spot size of ≈ 2 μm. Dramatic improvements in signal were observed using the higher magnification and shorter working distance objective. Further aspects of the experimental setup and measurements are detailed in the following sections.

3.4.1 Cryostats

Samples were mounted on the cold-finger of a cryostat and cooled cryogenically. Two cryostats were primarly used for optical measurements. The first was a custom build Precision Cryogenics liquid nitrogen cryostat used in initial measurements, and the second was a liquid helium cooled Janis ST-500 microscopy cryostat with a controlled temperature range of 3.5 - 475 K, which was used in all the later measurements after being purchased courtesy of lab flood #2. The nitrogen cryostat provided more stability because the chamber could be filled once and sit untouched. The helium one was a continuous flow cryostat, which

induced more vibrations. Due to the short working distances of objectives, special low oxygen copper sample mounts were made to place the samples in close proximity, $\approx$ 1 - 3 mm, to the cryostat window.

3.4.2 Sample Visualization

Once the cryostat is mounted and aligned in the setup, proper illumination is critical for the adequate visualization of samples. Given the small crystal sizes and the sheer number of them scattered on the substrate, micrometer translation stages are used to adjust the cryostat position. It is important to clearly image the surface to be able to retrieve the position of specific areas identified under the microscope during sample preparation. Limited by the field of view of the setup, their positions on the substrate are marked in advance on an image of the full substrate, which is used as a map to navigate to an exact location. The already aligned laser is then centered exactly on the areas of interest.

Illumination was done using an Ocean Optics HL-2000-HP tungsten halogen white light source, which was collimated at the output of a fiber. Its path was adjusted such that it was collinear with the incident laser beam upon reflection from the first beamsplitter. Imaging requires a diffuse beam of light encompassing the field of view, which can be tricky since the objective is setup to focus the laser on to the sample. This was accomplished by focussing the beam down with a lens prior to the microscope objective such that the beam diverged after the objective. A 20 cm focal length lens was used and its position was determined empirically. Finally, a second beamsplitter was also place in the path of the incident light, and a video camera with an adjustable zoom lens was able to use light reflected from the second beamsplitter to focus through the objective on to the sample surface.

3.4.3 Light Sources

Optical measurements were performed using a number of different light sources. PL measurements were predominantly performed using a Spectra-Physics BeamLok argon ion laser at the lasing wavelengths 476.5, 488.0, 496.5, and 514.5 nm. The output was directed into a prism monochromator to eliminate residual fluorescence and plasma lines from the spectra. In addition, measurements at higher energies were also performed using a 406 nm Coherent Cube diode laser borrowed from Professor Biteen's lab, and a 400 nm source obtained from frequency doubling the 800 nm output of a Spectra-Physics Tsunami oscillator with a BBO crystal. Finally, reflection measurements were performed using a 100 W quartz tungsten halogen lamp in a Newport cylindrical housing and powered by a DC power supply. The output of the lamp was sent through a diffuser mounted in a tube lens and focused into an optical fiber to be brought and aligned with the experimental setup. The fiber's output was the recollimated using an objective at its output. The lamp produced a blackbody radiation spectrum with conspicuously weaker output at higher energies. This resulted in noisier data and required increased averaging and longer scan times.

3.4.4 Spectrometers

Spectra were obtained using a SPEX 1404 double grating monochromator and a Dilor XY triple grating monochromator. The SPEX was equipped with a photomultiplier tube, while the Dilor has a Horiba Synapse CCD detector. PL and Raman experiments were done using the Dilor because of the ability to record spectra in one or two scan windows using the CCD detector. This allowed for more rapid data collection and averaging for each sample. The reflection measurements were done using the SPEX because of the uniform response of the PMT over the spectral ranges of interest. However, these scans took significantly longer as each step is measured individually and required more sample stability, hence the use of the nitrogen cryostat. It also important to note the polarization sensitivity of the cryostats due to the different grating responses. This was particularly critical in the comparison or Raman

peaks, and a broadband unpolarized lamp source with an analyzer was used to determine the relative spectrometer response at specific wavelengths.

3.4.5 Experimental Challenges

Two of the most glaring challenges in these measurements are the requirements for stability down to a micrometer scale and maximum signal collection. The first was particularly challenging given some of the experimental constraints. The optical tables were not floated to isolate from vibrations in the room. The entrance to the spectrometer is ≈ 25 cm above the table and the optics and cryostat were placed on long posts and elevated platforms for alignment with the spectrometer. Finally, the continuous flow of helium through the cryostat inherently causes some vibrations. Little could be done to address these issues without significant modifications and investment in the setup design. Every attempt was made to minimize vibrations and maximize the stability of the optics used. However the laser spot could be observed to vibrate on the sample and care was taken to choose large samples whenever possible. Additionally, the laser position was monitored before and after every scan to ensure that there was no significant drift during a scan.

While scans needed to be kept short to avoid drift over long time scales, they also needed to be long enough to ensure good signal to noise ratios. Typically this meant scans lasting no longer than 10 - 15 minutes on any one sample. Other factors were employed to maximize the signal collection. The beamsplitter directly before the cryostat was selected to have a 30/70 reflection to transmission ratio to maximize signal transmission. The selection of objective played the most critical role in improving the signal. The initial selection of a 50x objective with a 20.5 mm working distance proved to be a poor one. The spot size was often too large for the thinnest crystals and their signals were weak. Due to its distance, the 50x objective collected a significant amount of stray light relative to the emitted light from areas of interest. Moving to the 100x objective with a 6 mm working distance required much greater proximity of the objective as well as the samples to the cryostat window but

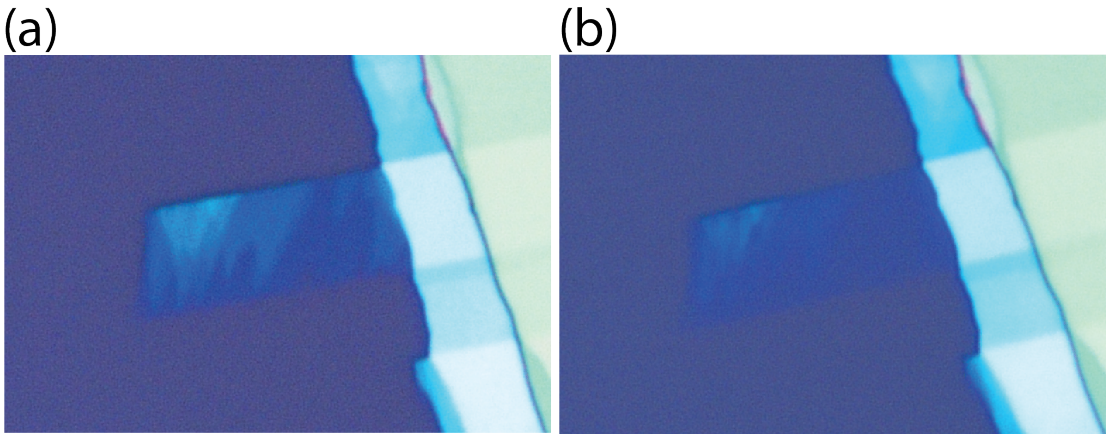

Figure 3.9: Optical microscope image of the same sample (a) immediately after exfoliation and (b) a week after exfoliation. Note image (b) was taken after the sample had been measured optically at low temperature and with the AFM.

resulted in a dramatic enhancement of signal collection.

Another factor taken into consideration was the quality and stability of exfoliated crystals over time. While reports of exfoliated sample degradation have been limited, there have been some materials which are reported to degrade over time [1, 32]. Exfoliated PbI_2 crystals did not appear to degrade significantly over time, but in a few instances, it was noticed visually that a sample appeared to have changed such as the one shown in Fig. 3.9. It was not clear if this degradation was from exposure to the environment, temperature cycling, or from AFM measurements. In addition, there have been some reports in the literature that temperature cycling may affect the exciton absorption strength. To avoid any issues, new samples were prepared for every measurement the day before and immediately put in vacuum after imaging the samples under the optical microscope. AFM measurements were then performed within a day or two of optical measurements.

3.4.6 Raman Microscope

We briefly mention here the existence of a number of different commercial Raman microscopes. Some measurements were performed on a Renishaw inVia Raman microscope in

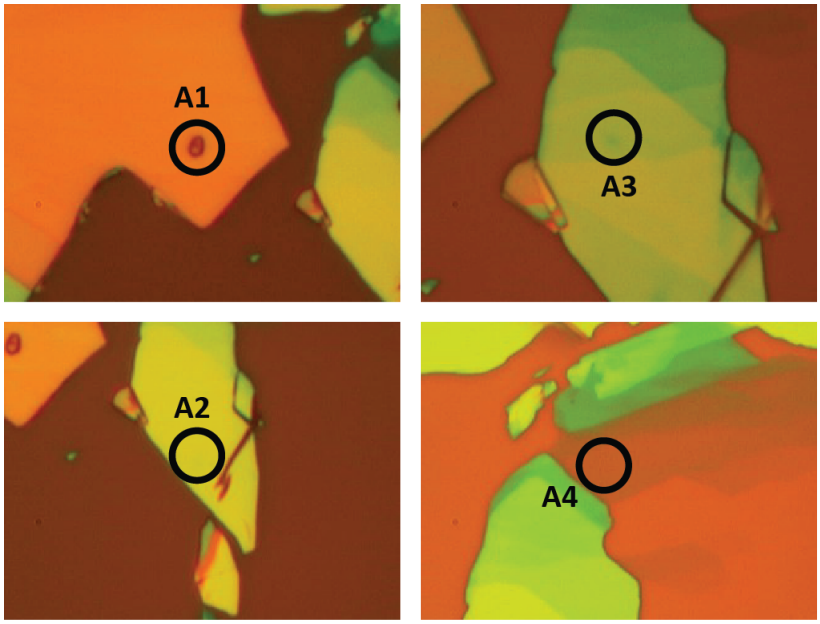

Figure 3.10: Images of PbI_2 samples taken on a Renishaw inVia Raman Microcope.

Professor Adam Matzger's lab. Images of samples measured are showed in Fig. 3.10. The advantage of such commercial instruments is that everything is built into the instrument with short optical paths, large signal collection, and relative stability. The samples can be imaged optically on a computer and positioned very precisely, using motorized stages, under the laser spot for PL and Raman measurements to be performed at the click of a button. The disadvantage is that these systems are extremely expensive and the setup is fixed. Most of the systems have one or two sources with accompanying filters that cannot be easily altered, and the systems in question did not have low temperature capabilities. Some measurements were performed using an 532 nm laser at room temperature, but the instrument used a notch filter to remove the laser line, which simultaneously blocked any signal below $\approx$ 150 cm^{-1}. In theory, such an instrument could be extremely useful if equipped properly for the material of interest.

CHAPTER 4

Computational Methods

Well established theories and techniques have been pioneered by a number of groups, which allow for incredibly accurate first principles calculations of the electronic and in turn, the optical properties of bulk and nanoscale materials. We have successfully demonstrated that these techniques can be applied to layer structures down to the mono- and few-layer limits, where the structure effectively becomes a two-dimensional material. These new material systems exhibit novel properties in stark contrast to their bulk counterparts and have the potential to strongly impact a multitude of electronic and optoelectronic technologies. Among other things, our work has demonstrated the ability to calculate electronic band gaps, exciton energies, as well as absorption profiles for mono- and few-layer structures for materials including PbI_2. We have found dramatic increases in the electronic band gaps of monolayers on the order of 1 eV as well as simultaneous enhancements in the exciton binding energies on the order of hundreds of meV. In addition to these properties, we have predicted fundamental changes in the electronic structure with decreasing thickness that can result in band gaps changing from direct to indirect or vice versa. These calculations are a powerful means of predicting and understanding the electronic and optical response of atomically thin materials, and can be applied to a diverse set of materials and substrates. At these scales, the surrounding dielectric screening can have an important effect on the energies of the system, which must be modeled for different substrates and applications. This is particularly important to study for the case of stacking different mono- and few-layer materials

on top of one another with the hopes of tuning the optical transition energies and charge transfer within the system. These calculations provide unprecedented power to guide the experimental efforts as well as providing insight to their results.

The procedures laid out in the following sections were utilized to calculate the band-structure and $n = 1$ exciton energies for bulk and few-layer PbI_2. The steps can generally be categorized under a few different types of calculations: steps 1 though 4 are density functional theory (DFT) calculations, steps 7 & 8 are termed GW calculations and steps 9 & 10 are Bethe-Salpeter equation (BSE) calculations. With the results of those calculations, it is possible to then make corrections for spin orbit effects and perform interpolation of the eigenenergies to generate the complete electronic band structure of a material. These procedures are individually described in more detail in the following sections.

4.1 Density Functional Theory Calculations

To exactly calculate the electronic properties of a material, requires solving the Schrödinger equation for all the interacting electrons and nuclei within the system. The required Hamiltonian is given by

$$\hat{H} = \sum_i \frac{-\hbar^2}{2m_e}\nabla_i^2 + \sum_{i,I} \frac{Z_I e^2}{|\boldsymbol{r}_i - \boldsymbol{R}_I|} + \frac{1}{2}\sum_{i\neq j} \frac{e^2}{|\boldsymbol{r}_i - \boldsymbol{r}_j|} + \sum_I \frac{-\hbar^2}{2M_I}\nabla_I^2 + \frac{1}{2}\sum_{I\neq J} \frac{Z_I Z_J e^2}{|\boldsymbol{R}_I - \boldsymbol{R}_J|} \tag{4.1}$$

where the usual notations for position, $\boldsymbol{r}_i$ ($\boldsymbol{R}_i$), mass, m_i (M_I), and charge, e ($Z_I e$) are used for the electrons (nuclei). Of course this problem is computationally impossible to solve because of the complexity and sheer number of particles in a real system. However a number of physically justified approximations can be made that allow for simpler calculations to be performed which yield results that are in very good agreement with experiments; see for example Martin's book [33]. The starting point for these calculations is always to consider the ground state of the material and to then calculate excited state properties based on

the ground state results.

Density functional theory (DFT) is one of the predominant method to calculate ground state properties for a system of interacting electrons and is based on the theory of Hohenberg and Kohn. They theorized that a functional for the energy of a system of interacting particles with any external potential could be defined solely by the charge density within the system, $n(\boldsymbol{r})$. This formulation removes the many body wavefunction and can be expressed as

$$E_{HK} = T[n] + E_{int}[n] + \int d\boldsymbol{r} V_{ext}(\boldsymbol{r}) n(\boldsymbol{r}) \tag{4.2}$$

where T is the kinetic energy, E_{int} is the interaction energy of the electrons and V_{ext} is the external potential, which for our purposes will consist of the lattice. For the purposes of this discussion, the interaction term between nuclei is neglected as it is independent of the electron density. If all the terms in Eq. 4.2 are known, one can in principle minimize the total energy to determine the exact ground state charge density of the system. In reality these terms are not known exactly, and thus, a slightly different approach developed by Kohn and Sham must be followed. The alternative approach is to assume a system of non-interacting particles with an auxiliary Hamiltonian, in which the many body interaction is included separately in the form of an exchange-correlation functional $E_{xc}[n]$. The total energy is then written as

$$E_{KS} = T_s[n] + \int d\boldsymbol{r} V_{ext}(\boldsymbol{r}) n(\boldsymbol{r}) + E_H[n] + E_{xc}[n] \tag{4.3}$$

where T_s is the kinetic energy of the independent particle system and E_H is the Hatree energy corresponding to the classical interaction energy of the electron system without exchange or correlation contributions. In this form, the Kohn-Sham variational equations are derived for the single particle orbitals ψ_i:

$$(H_{KS} - \varepsilon_i)\psi_i(\boldsymbol{r}) = 0 \tag{4.4}$$

where

$$H_{KS} = -\frac{\hbar^2}{2m_e}\nabla^2 + V_{ext}(\boldsymbol{r}) + V_H(\boldsymbol{r}) + V_{xc}(\boldsymbol{r}) \tag{4.5}$$

Equations 4.4 & 4.5 are exact and if V_{xc} were known, would lead to the exact ground state density. However in practice by separating out the long range Hartree interaction, various approximations can be made for the exchange and correlation term locally, which give results in remarkable agreement with experiments.

4.1.1 Local Density Approximation

For the purposes of this thesis we mention only the local density approximation (LDA) employed in the calculations presented in Ch. 5. LDA approximates the charge density as that of a homogenous electron gas for which the total energy is obtained by integrating the local exchange and correlation energy densities over the entire system

$$E_{xc}^{LDA} = \int d\boldsymbol{r} n(\boldsymbol{r}) \left[\epsilon_x(n(\boldsymbol{r})) + \epsilon_c(n(\boldsymbol{r}))\right] \tag{4.6}$$

Values for the exchange and correlation energies as a function of density have been determined to a high level of accuracy with calculations and quantum Monte Carlo simulations obtained for a homogeneous electron gas. Exchange and correlation effects are expected to be short range and thus well approximated by a homogeneous gas for many semiconductor materials. However it is well known that despite yielding accurate ground state properties, the LDA eigenenergies are not those of the actual physical system. In particular, they are known to underestimate the band gap, and thus, further methods are required to obtain accurate excited state properties.

4.1.2 Pseudopotentials

In the case of semiconductors, the external potential described above comes from the lattice of atomic nuclei. However it is important to note that electron wavefunctions very close to a nucleus can have highly oscillatory forms. At the same time, the valence electrons are primarily responsible for bonding between atoms. As a result, calculations can be greatly simplified by merely replacing the atomic nuclei and their core electrons by atomic pseudopotentials with the appropriate wavefunctions for the valence electrons outside the core region. Norm-conserving pseudopotentials do just this using orthonormal wavefunctions for a model potential that varies smoothly inside the core and yields functions that match the real electron wavefunctions outside the defined core region. It is important to note that the obtained model potential depends on the orbital angular momentum and as such is semilocal in nature. These pseudopotentials serve as the starting point for most *ab initio* calculations of solids where it is convenient to expand the eigenstates of the Kohn-Sham equations using a plane wave basis.

Methods for generating pseudopotentials are well documented [34]. For the calculations presented here, separate pseudopotentials for iodine and lead were generated by Professor Emmanouil Kioupakis. In the case of the iodine pseudopotential, only the 5s and 5p electrons were treated as valence electrons. In the case of lead however, in addition to the 6s and 6p electrons, the 5d electrons were also included in the valence electrons because they are shallow and mix with the valence electrons of iodine.

4.1.3 Bulk and Layer Unit Cells

In the same way that a periodic crystal can be completely described by repeating a unit cell, its energy can be calculated using a single unit cell and periodic boundary conditions. For bulk calculations, this means the unit cell is merely the unit cell of the crystal. In the case of PbI_2, the cell is defined as in Fig. 2.1 with three atoms per cell. For the layer structures however, the unit cell must be modified along the $\hat{c}$ direction of the crystal to avoid inter-

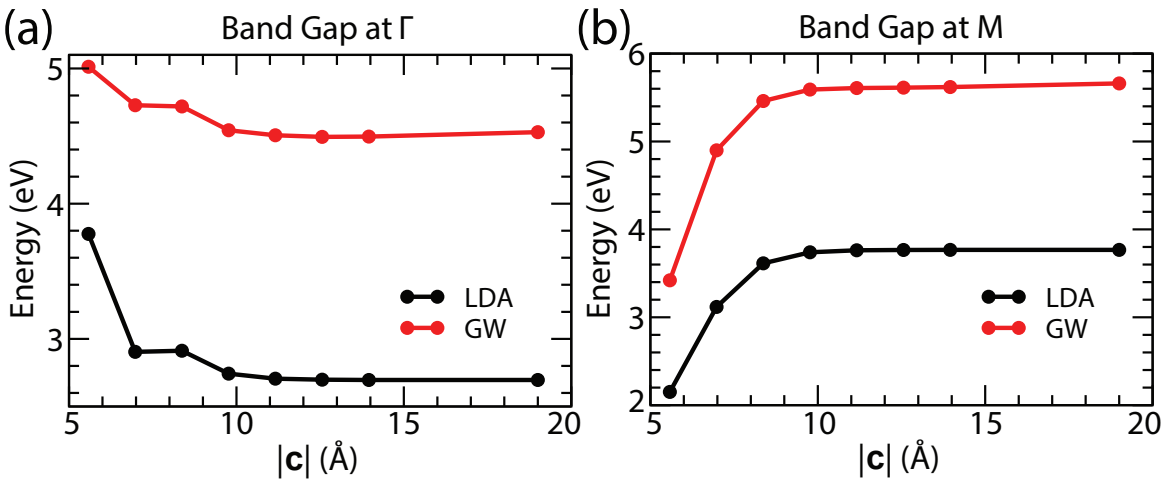

Figure 4.1: Convergence calculations showing the band gap calculated at the Γ and M points of the Brillouin zone as a function of the super-cell size in the $\hat{c}$ direction. Calculations are shown for both LDA and GW calculations.

actions between a layer and its periodic image. This is accomplished by extending the unit cell and adding a layer of vacuum above and below the layers of material to create what is referred to as a supercell. This reduces the interaction between periodic images and the separation can be adjusted to achieve a required energy tolerance. However, this comes at cost because increasing the size of the supercell also increases the computational cost of calculations, and thus, limiting the separation.

The supercell sizes were determined by converging the individual band energies as well as the band gaps of each layer structure.

4.1.4 Plane Wave Basis

It is known that according to Bloch's theorem, the electronic wavefunctions in a crystal can be described by the product of a plane wave with a function that is periodic with the lattice. The periodic function is typically expanded using a plane wave basis set [35]

$$\psi_i(\boldsymbol{r}) = \sum_{\boldsymbol{G}} C_{i,\boldsymbol{k}+\boldsymbol{G}} e^{i(\boldsymbol{k}+\boldsymbol{G})\cdot\boldsymbol{r}} \tag{4.7}$$

Table 4.1: Total energy obtained for a bulk PbI_2 scf calculation of the charge density for various plane wave cutoff energies using a 4x4x3 k-grid.

ECUTWFC (RY)	TOTAL ENERGY (RY)
40	-224.699
50	-224.830
60	-224.836
80	-224.844
100	-224.848
600	-224.849

Table 4.2: Difference in band energies calculated at the Γ point for plane wave cutoffs of 600 and 50 Ry, i.e. $\Delta E = E(50) - E(600)$. Results were obtained for a bulk PbI_2 nscf calculation using a 4x4x3 k-grid. Note that band 14 is the highest occupied valence band.

BAND #:	1,2	3	4,5	6	7	8	9	10,11	12,13	14	15	16,17
ΔE (meV)	11.4	11.4	11.5	3.8	4.8	0.3	0.3	0.0	0.3	0.1	0.0	0.9

where the $\boldsymbol{G}$'s are reciprocal lattice vectors and $C_{i,\boldsymbol{k}+\boldsymbol{G}}$ is the amplitude of each plane wave.

In solving the Kohn-Sham equations, it makes sense to only include as many plane waves as are necessary for the desired calculation. Thus, plane waves are included only up to a maximum cutoff, which is dependent solely on the pseudopotential used and determined by convergence tests on the relevant energy. In this case, convergence of both the total energy as well as individual band energies, both at the LDA level, were considered. In Quantum Espresso, the plane wave cutoff is set with the flag `ecutwfc`, which sets the kinetic energy cutoff in Rydberg energy. Table 4.1 shows the total energies obtained from an scf calculation on bulk PbI_2 for a range of cutoff energies. The values of the total energies themselves are unimportant but the change in energy from one cutoff to a higher cutoff should be converged down to $\approx$ 1 mRy/atom. A cutoff of 50 Ry was selected for the pseudopotentials used in the present calculations. It is clear from Tab. 4.2 that 50 Ry is sufficiently large to converge the energies of individual bands to well within the $\sim$ 0.1 eV tolerance of the technique. Unless otherwise stated, all subsequent calculations were performed with a plane wave cutoff of 50 Ry.

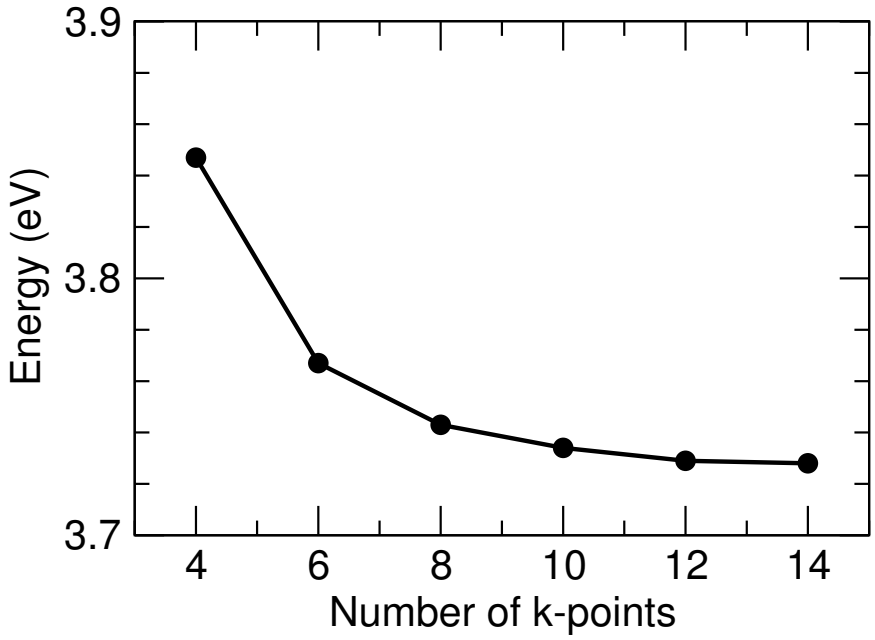

Figure 4.2: GW band gaps calculated for a 2 L structure as a function of the number of k-points in both in-plane directions. Calculations were performed with only 200 bands included in the epsilon and sigma calculations to minimize the computational cost while converging the sampling grid.

4.1.5 k-Space Sampling

LDA and GW band energy calculations were performed on a sampling grid of discrete points in reciprocal space. Interpolation was performed afterwards to generate complete band structures. To keep the computational costs down, the smallest grid sizes that produced converged energy calculations were used. The k-grid sizes were determined by convergence tests on the band gap. A convergence test for the 2 L structure is shown in Fig. 4.2, where a 9x9x1 grid size was selected because its band gap was within ≈ 0.01 eV of the converged value. Layer structures only included one k point along $\hat{c}$ due to their lack of periodicity.

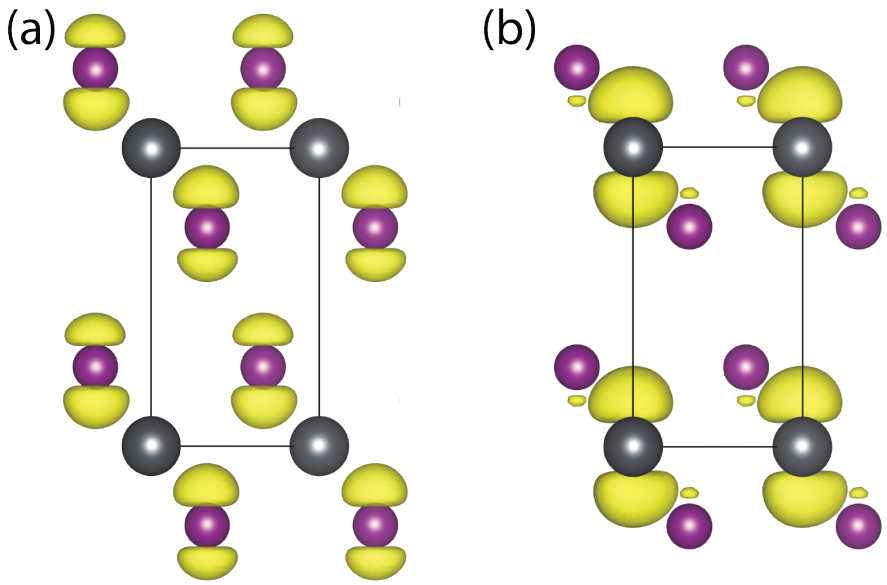

Figure 4.3: Isosurfaces encompassing $\approx 33\%$ of the charge density for the (a) highest valence and (b) lowest conduction bands.

4.1.6 Quantum Espresso Calculations

The LDA calculations in this thesis were performed using the Quantum Espresso package. To generate a complete band structure, we began by running a self-consistent (scf) calculation to obtain the charge density of the system. This was followed by a non-self-consistent calculations to obtain the wavefunctions at all points in k-space.

4.1.7 Band Projections

We can project the calculated LDA eigenfunctions on to the atomic orbitals to determine the dominant orbital contributions of each band. The results are shown in Tab. 4.3, and the charge density for the top filled valence band, 14, and lowest empty conduction band, 15, are plotted in real space in Fig. 4.3. However this projection is done without including SO effects. The VASP program allows one to automatically include spin orbit in the LDA band calculations. Without SO, VASP results are agree almost exactly with the Quantum Espresso projections. However, we find if the projection is done including SO using VASP

Table 4.3: Dominant contributions of valence and conduction bands from projections on to atomic orbitals at the A point for LDA wavefunctions without SO.

BAND NUMBER:	ATOMIC ORBITAL
1 - 5	Pb: d
6 - 7	I: s
8	Pb: s
9	I: p_z
10 - 13	I: $p_{x,y}$
14	I: p_z (84%); Pb: s (14%)
15	Pb: p_z (81%); I: s (14%)
16 - 17	Pb: $p_{x,y}$)

as opposed to Quantum Espresso that SO mixes in some $p_{x,y}$ contributions. For band 14, the mixing adds approximately 10% of I: $p_{x,y}$ into and the p_z contribution drops to $\approx 70\%$. For band 15, the effect is much more significant, with an addition of approximately 40% of Pb: $p_{x,y}$ and the p_z contribution drops to approximately 44%. This band mixing proves to be critical in understanding the band edge absorption in PbI_2.

4.1.8 Relaxation

Calculations were performed using the bulk parameters because relaxation techniques that minimize the energy based on the positions of the atoms have trouble dealing with van der Waals interactions. Thus relaxed bulk cell parameters were calculated and used for the calculation of band gaps and exciton energies of layer structures to study the dependence of these energies on the atomic positions. A decrease of $\approx 2.9\%$ in the out-of-plane lattice vector and $\approx 1.7\%$ decrease in the in plane lattice vector was obtained for the bulk relaxation. Results for layer structures using the relaxed bulk atomic positions are shown in Fig. 4.4. The layer separation appears to have the strongest effect and shifts all the energies downward. This is evident from the monolayer, which experiences very little change in the band gap. This may be a result of the predominant p-z like top valence and lowest conduction bands, which are expected to be more sensitive to the interlayer spacing.

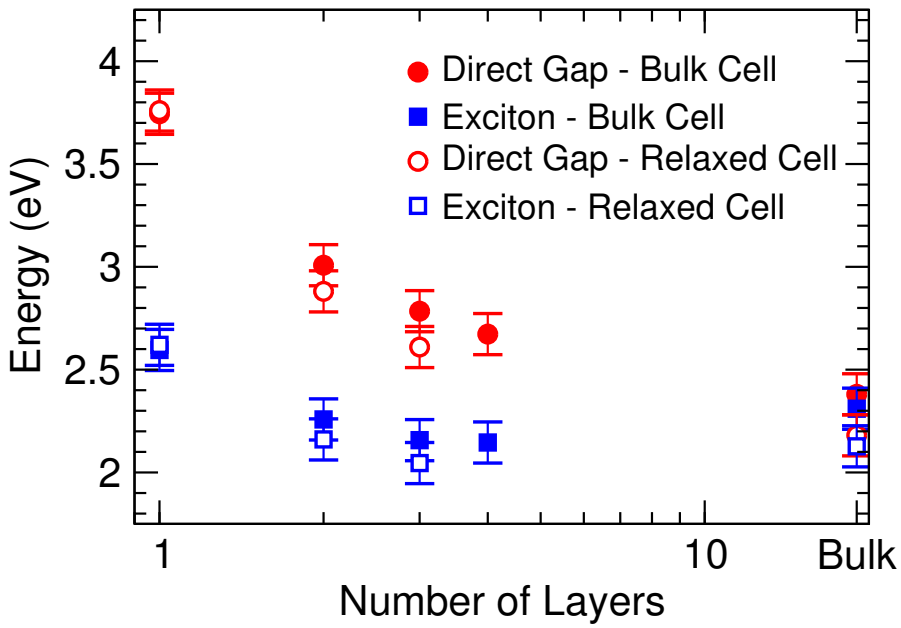

Figure 4.4: Comparison of exciton energies for structures using bulk and relaxed cell parameters.

4.2 GW Calculations

As mentioned earlier, the goal of the Kohn-Sham formalism is to obtain an accurate ground state charge density. However, the obtained eigenvalues and eigenvectors are not accurate representations of the physical excitation energies and are well known to underestimate the band gaps of semiconductors. To obtain accurate excitation energies, such as those probed by optical experiments, one must go beyond DFT and LDA methods and consider the effect of introducing excited electron or hole particles into the system. These particles will affect the surrounding electrons and induce a polarization or modified potential around the excited particle, which is termed a quasiparticle and has an associated self energy. The GW approximation is well established technique, which has demonstrated significantly more accurate excited state results. Quasiparticle energies in this work have been calculated using the BerkeleyGW package (www.berkeleygw.org) with the DFT eigenenergies and wavefunctions used as a starting point.

4.2.1 GW Approximation

The approach employed to determine quasiparticle properties is based on a the use of single particle Green's functions for particles in a system of interacting electrons. The Hamiltonian of this system is given by

$$H = \sum_i \left[-\frac{\hbar^2}{2m_e}\nabla^2 + V_{ext}(\boldsymbol{r}_i) \right] (\boldsymbol{r}_i) + \sum_{i<j} V_c(|\boldsymbol{r}_i - \boldsymbol{r}_j|) \tag{4.8}$$

where V_c is the bare Coulomb potential term. In addition, the Green's function can be expressed as

$$G(\boldsymbol{r}, \boldsymbol{r'}; \omega) = \sum_{n\boldsymbol{k}} \frac{\psi_{n\boldsymbol{k}}(\boldsymbol{r})\psi^*_{n\boldsymbol{k}}(\boldsymbol{r'})}{\omega - E_{n\boldsymbol{k}}} \tag{4.9}$$

where $\psi_{n\boldsymbol{k}}(\boldsymbol{r})$ and $E_{n\boldsymbol{k}}$ are the quasiparticle wave function and energy respectively for a give band n and wavevector $\boldsymbol{k}$. Then from the equation of motion for the Green's function, one can obtain the quasiparticle equation

$$\left(-\frac{\hbar^2}{2m_e}\nabla^2 + V_{ext}(\boldsymbol{r}) + V_H(\boldsymbol{r}) \right) \psi_{n\boldsymbol{k}}(\boldsymbol{r}) + \int \Sigma(\boldsymbol{r}, \boldsymbol{r'}; E_{n\boldsymbol{k}})\psi_{n\boldsymbol{k}}(\boldsymbol{r'})d\boldsymbol{r'} = E_{n\boldsymbol{k}}\psi_{n\boldsymbol{k}}(\boldsymbol{r}) \tag{4.10}$$

where $\Sigma(\boldsymbol{r}, \boldsymbol{r'}; E_{n\boldsymbol{k}})$ is the self energy of the quasiparticle through which the many-body interactions are included. One must then determine the self energy to solve for the quasiparticle energies and wave functions. In principle this is accomplished by solving Hedin's equations self consistently. In practice, an expansion of Σ can be made in terms of the Green's function G and the screened Coulomb interaction W given by

$$W(\boldsymbol{r}, \boldsymbol{r'}; \omega) = \int \varepsilon^{-1}(\boldsymbol{r}, \boldsymbol{r''}; \omega)V_c(\boldsymbol{r''}, \boldsymbol{r'})d\boldsymbol{r''} \tag{4.11}$$

where $\varepsilon(\boldsymbol{r}, \boldsymbol{r''}; \omega)$ is the dielectric response of the system. The lowest order term of such an expansion is given by

$$\Sigma(\boldsymbol{r}, \boldsymbol{r'}; E_{n\boldsymbol{k}}) = i \int \frac{d\omega}{2\pi} e^{-t(0^+)\omega} G(\boldsymbol{r}, \boldsymbol{r'}; E - \omega) W(\boldsymbol{r}, \boldsymbol{r'}; \omega) \tag{4.12}$$

and provides the name of GW approximation. This has proved to be a very good approximation of Σ, whereby the self energy of the quasiparticle can be determined using DFT results as a starting point to construct the Green's function, known as a single shot G_0W_0 calculation. The frequency dependent dielectric response can in turn also be determined, and in practice is done using a plasmon pole model. This formalism provides a means to determine the quasiparticle energies which have been found to give excellent agreement to within ≈ 10 % and resolve the apparent band gap problem for LDA calculations of most semiconductors and insulators.

4.2.2 Coulomb Truncation

It is important to note that a truncation of the Coulomb interaction in the layer structures is implemented to eliminate spurious interactions between periodic images. This is not a problem for bulk calculations but it is a concern when calculating confined systems. Supercells serve to eliminate interaction of the electronic wavefunctions, which decay exponentially in the vacuum, however the Coulomb interaction decays slowly. This sheet truncation is built directly into the bare Coulomb interaction in the BerkeleyGW package as [36]

$$V_c(r) = \frac{\theta(z_c - |z|)}{|r|} \tag{4.13}$$

where the cutoff distance is set to $z_c = L_z/2$. Coulomb truncation is utilized in the GW and BSE calculations of the layered structures in this work and has been shown to rapidly increase band gap and binding energy convergence with layer separation and k-space sampling [37].

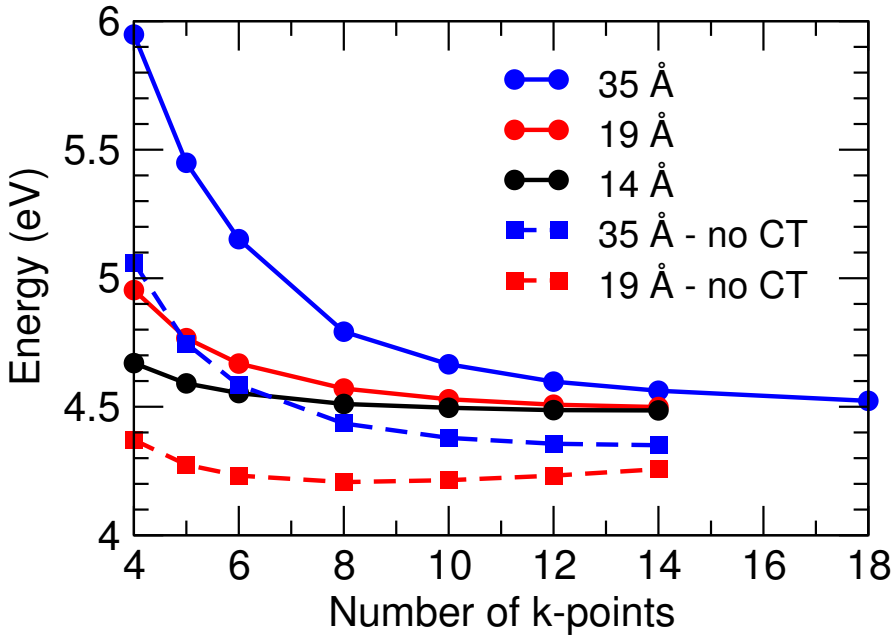

Figure 4.5: GW band gaps calculations for a 1 L structure as a function of the number of k-points along both in-plane directions. Different curves were calculated for various supercell sizes by varying the amount of vacuum. Dashed curves represent calculations without the use of the Coulomb truncation method.

4.2.3 GW Convergence

The static dielectric response used in the GW calculations is computed as a matrix in momentum space given by [36]

$$\varepsilon_{\boldsymbol{GG'}}(\boldsymbol{q};\omega=0) = \delta_{\boldsymbol{GG'}} - V_c(\boldsymbol{q}+\boldsymbol{G})\chi_{\boldsymbol{GG'}}(\boldsymbol{q};0) \tag{4.14}$$

where $\chi_{\boldsymbol{GG'}}$ is the RPA polarizability and involves a sum over all the empty states included in the calculation. The size of this matrix depends on the number of $\boldsymbol{G}$ vectors included and must be converged with respect to the energy tolerance required to determine the cutoff. Additionally, the number of empty bands included in the polarizability sum must be converged. Ideally the energy of the highest band should be equivalent to the $\boldsymbol{G}$ vector cutoff energy. However in practice, as cutoffs are increased and more bands are included, the computational cost over a grid of k-points can increase dramatically. Luckily in many

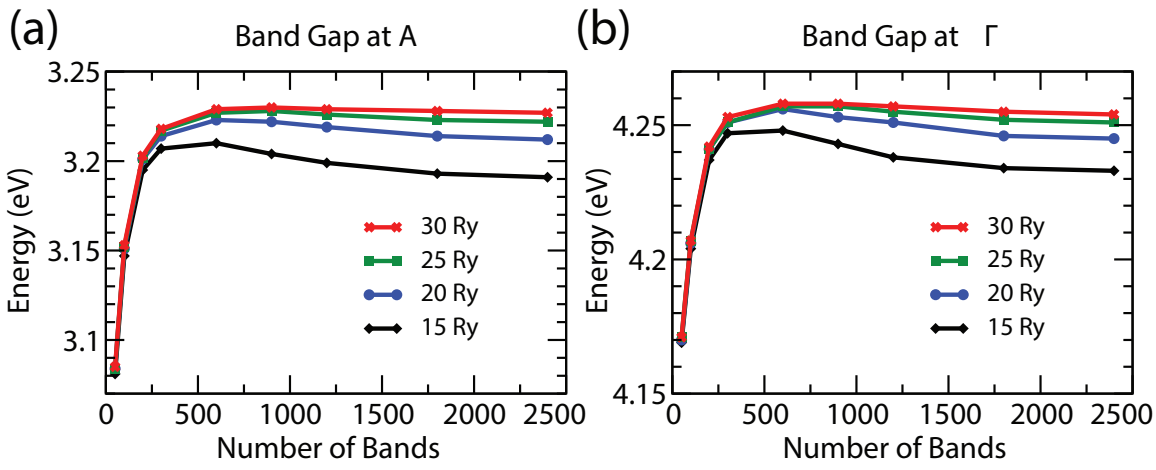

Figure 4.6: Calculated band gap energies for a bulk PbI_2 structure as a function of the number of empty bands included in both the epsilon and sigma calculations at the (a) A and (b) Γ points in reciprocal space. Colored curves represent different epsilon cutoff energies as indicated.

cases, the property of interest can be found to converge to adequate tolerances with lower parameters, which minimizes the time and computational cost of the calculations.

Figure 4.6 presents convergence tests performed at two different point in k-space in bulk PbI_2 to determine the required epsilon cutoff and number of empty bands. It is clear that to fully converge the band gap both a large enough cutoff and number of bands must be used in the epsilon calculation. A cutoff of 20 Ry was selected because it appears to converge the energy to within a tolerance of 0.02 eV. This cutoff was then used in all final calculations. In practice, the required epsilon cutoff did not vary from bulk to layered structures and 20 Ry was used for both. However with increasing number of layers and supercell sizes, the energy of each additional empty band decreases. Thus, the number of empty bands was converged separately for each structure to obtain approximately the same highest band energy. These results are shown in Tab. 4.4. Calculations for the one layer structure were performed at a much higher energy cutoff merely because one layer calculations were significantly cheaper than for more layers.

In addition, one must specify the number of bands over which to sum in calculating the Σ term. Again it is recommended that the highest band included be equal to the the

Table 4.4: Number of bands used in final epsilon calculations and determined from convergence tests. The corresponding band energies for the highest empty bands are also listed.

STRUCTURE	NUMBER OF BANDS	BAND ENERGY (EV)
1 L	1000	158
2 L	1200	113
3 L	2100	125
4 L	2500	117
Bulk	400	122

energy of the epsilon cutoff. However, the computational cost increases dramatically with the number of states, and the band gaps were found to converge much earlier. It was found that 400 bands was sufficient to achieve a convergence of ≈ 0.025 eV for all the structures, and this was the number of bands included in all final sigma calculations.

4.3 Spin-Orbit Coupling

Spin-orbit coupling strength is proportional to the atomic number of the atoms in the material. Given that I has atomic number of 53 and Pb has an atomic number of 82, spin-orbit effects are expected to be strong in PbI_2. We therefore include the effect of spin-orbit coupling as a correction to the GW band energies by adding a term to the Hamiltonian [38]

$$H^{SO} = \sum_{l} |l\rangle \, V_l^{SO}(r) \boldsymbol{L} \cdot \boldsymbol{S} \, \langle l| \tag{4.15}$$

Wavefunctions obtained from LDA calculations and expanded in the plane-wave basis set give a new Hamiltonian matrix $H_{s,\boldsymbol{k}+\boldsymbol{G};s',\boldsymbol{k}+\boldsymbol{G'}}$. This Hamiltonian can then be added to the previously calculated LDA + GW matrix and rediagonalized to obtain the spin-orbit corrected eigenenergies.

This task was performed using a code which follows the method described in Ref. [38]. Convergence tests were performed and SO energies at the A point in bulk were found to be converged for 200 bands, an energy cutoff of 40 Ry, and a k-grid of 400. These parameters

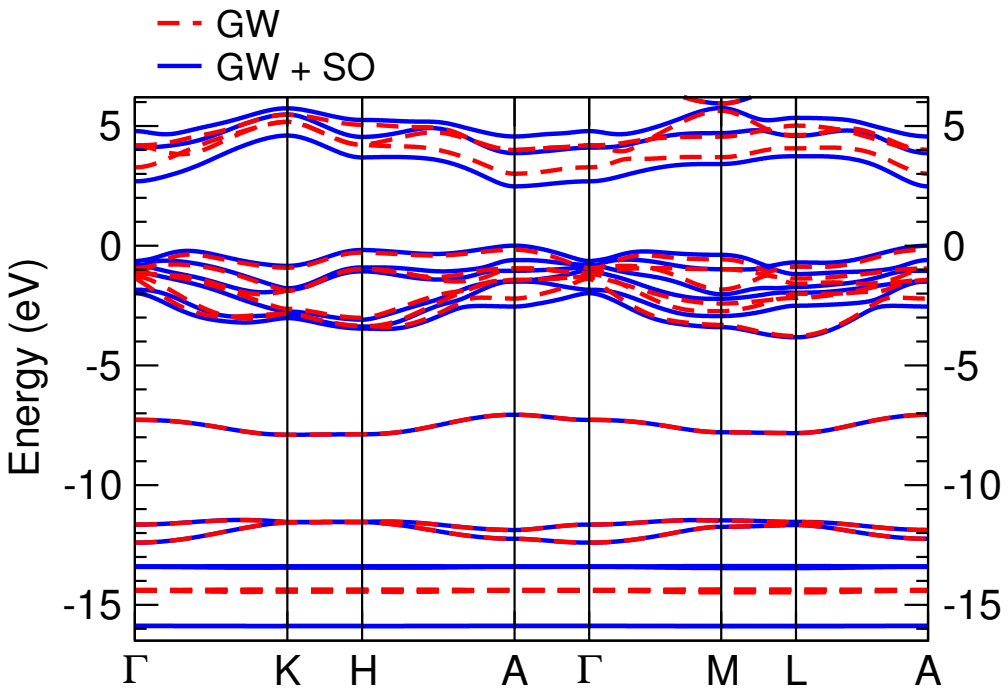

Figure 4.7: GW bandstructures calculated for bulk PbI_2 without (GW) and with (GW + SO) the inclusion of spin orbit interactions. The plot is showing the 14 highest valence and 3 lowest conduction bands with the top valence band maximum corresponding to 0 eV.

were used for band gap energy calculations, with the band number converged to higher values for few-layer structures. The spin-orbit correction varied very little in bulk and layered structures, and was found to be ≈ 0.8 eV in all cases. Fewer bands were used to calculate the complete band structures at many k-points for which the exact energies were less critical. Results of SO corrections to the bulk bandstructure are shown in Fig. 4.7. SO interactions tend to affect the lowest d-like bands the most, splitting them into two groups. It also affects the predominantly p-like bands which make up the top six valence and lowest three conduction bands. As indicated previously, SO effects tend to mix the bands, but it is important to note that the shape of the top valence and lowest conduction bands change very little. Near the band gap at the A point, SO appears to rigidly shift the bands without affecting their form, which is used later to justify rigidly shifting exciton energies calculated without the explicit inclusion of SO effects.

4.4 Wannier Interpolation

As discussed in Sec. 4.1.5, the LDA + GW calculations were performed at points on a fixed grid in reciprocal space. The size of the grids is minimized and limited by the computational cost of calculations, resulting in fewer than 10 points along any one direction in k-space for most structures. With such low sampling it would be impossible to visualize and identify separate bands, particularly when band crossings occur. To resolve this issue, we use an interpolation technique based around Wannier functions built into the `Wannier90` program, which is freely available at *www.wannier.org*.

The technique is based on defining a set of N Wannier functions $w_{n\boldsymbol{R}}(\boldsymbol{r})$, which are constructed from a set Bloch bands $\psi_{n\boldsymbol{k}}(\boldsymbol{r})$ rotated by a unitary matrix $U^{\boldsymbol{k}}$ to give [39]

$$w_{n\boldsymbol{R}}(\boldsymbol{r}) = \frac{V}{(2\pi)^3} \int_{BZ} \left(\sum_{m}^{N} U^{\boldsymbol{k}}_{mn} \psi_{m\boldsymbol{k}}(\boldsymbol{r}) \right) e^{-i\boldsymbol{k}\cdot\boldsymbol{R}} d\boldsymbol{k}. \tag{4.16}$$

The problem then essentially boils down to minimizing the spread of the functions with

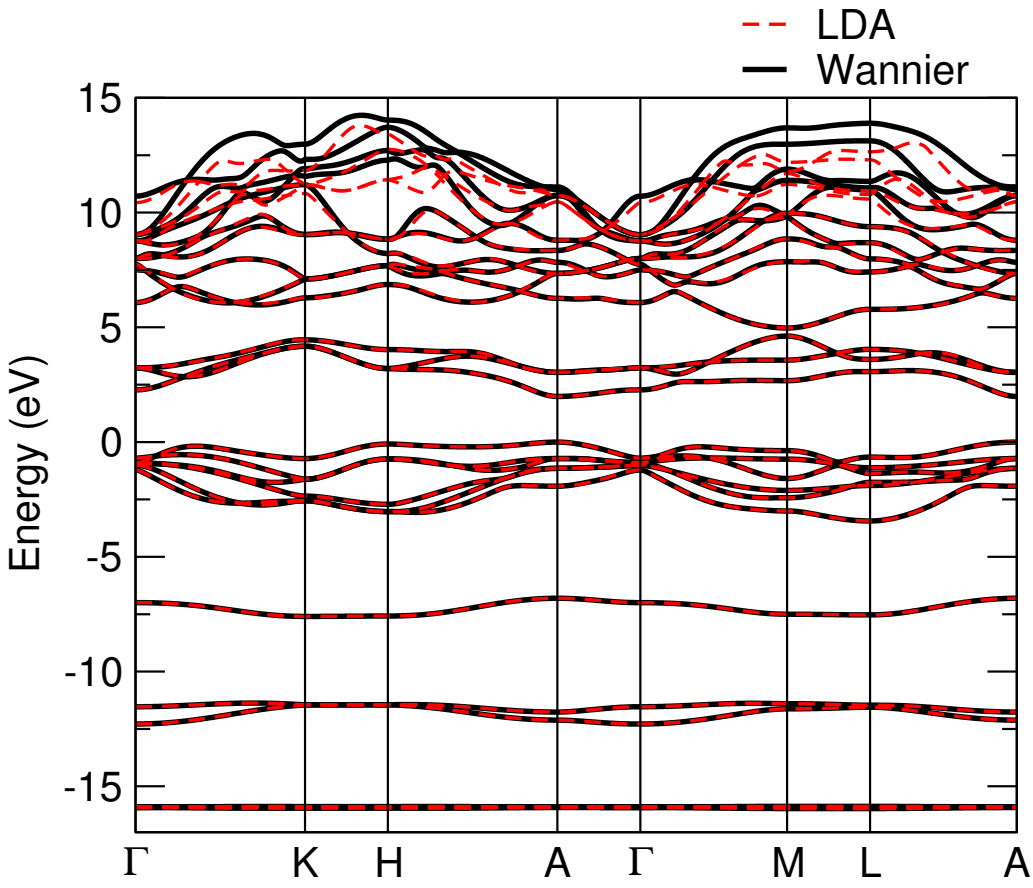

Figure 4.8: An example convergence test of the bulk PbI_2 band structure using the Wannier90 code. The bandstructure generated using Wannier interpolation is compared to bands calculated directly at the LDA level using the Quantum ESPRESSO code. The ordinate axis is adjusted such that 0 eV corresponds to the top valence band maximum.

respect to the unitary rotations, where the total spread can be expressed as

$$\Omega = \sum_{n}^{N} \langle w_{n\mathbf{0}} | \, r^2 \, | w_{n\mathbf{0}} \rangle - | \langle w_{n\mathbf{0}} | \, \boldsymbol{r} \, | w_{n\mathbf{0}} \rangle |^2 \tag{4.17}$$

Using similar minimization procedures, entangled bands can also be separated by maximizing their overlap at every point in $\boldsymbol{k}$ [40]. In the end, this method yields maximally localized Wannier functions, which can be visualized in real space. Using the unitary matrices, the LDA + GW Hamiltonian can also be rotated to yield a Hamiltonian in the Wannier basis $H^W(\boldsymbol{k})$ from which a Fourier sum can be constructed

$$H_{nm}(\boldsymbol{R}) = \frac{1}{N_0} \sum_{\boldsymbol{k}} e^{-i\boldsymbol{k}\cdot\boldsymbol{R}} H^W_{nm}(\boldsymbol{k}) \tag{4.18}$$

where N_0 is the number of lattice vectors $\boldsymbol{R}$ given by the k-grid. An inverse Fourier transform can then be taken to interpolate $H(\boldsymbol{k})$ on to a significantly finer sampling grid than the one on which the LDA + GW calculations are performed.

An example calculation is shown for bulk PbI_2 in Fig. 4.8. The bandstructure calculated using Wannier interpolation is compared to a band structure calculated directly at the LDA level at many points in k-space. Tests such as this one were conducted to ensure the interpolation was properly converged and generated the proper bandstructure when fully converged GW bandstructures were calculated. As is clear, the band agreement is almost exact between the two techniques below $\approx$ 10 eV. As we are primarily interested in the valence and first three conduction bands, below 5 eV, the agreement justifies the reliable use of Wannier interpolation to generate the complete GW + SO bandstructures.

4.5 Bethe-Salpeter Equation

In the case of the optical spectra of semiconductors, we are often interested in the absorption of a material. This process is dependent on the simultaneous excitation of an electron

and hole as well as their mutual interaction, known as excitonic effects. Therefore the electron and the hole quasiparticles must be described together by a two-particle Green's function and a combined exciton state S whose wave function is given by

$$\chi_S(\boldsymbol{r}, \boldsymbol{r'}) = \sum_{v}^{hole} \sum_{c}^{elec} A_{cv}^S \psi_c(\boldsymbol{r}) \psi_v^*(\boldsymbol{r'}) \tag{4.19}$$

where c (v) correspond to quasi-electron (quasi-hole) states and ψ their respective wave functions. The equation of motion for the quasi-electron and hole Green's function yields an eigenvalue form of the Bethe-Salpeter equation for the coefficients A_{cv}^S

$$(E_c - E_v) A_{cv}^S + \sum_{cv,c'v'} K_{cv,c'v'}(\Omega_S) A_{c'v'}^S = \Omega_S A_{cv}^S \tag{4.20}$$

which can be solved to obtain the excitation energies Ω_S and wavefunctions. The kernel K contains the excited electron and hole interactions and is related to the self energy for both quasiparticles. Following from the GW approximation, the kernel for a given set of positions, spins, and times, e.g. $1 = (\boldsymbol{r}_1, \sigma_1, t_1)$ is found to be

$$K(1,2,3,4) = -i\delta(1,3)\delta(2^-,4)V_c(1,4) + i\delta(1,4)\delta(3,2)W(1^+,3) \tag{4.21}$$

where the first terms acts as a repulsive exchange term and the second acts as an attractive screening term. Finally, having determined the excited state energies and wavefunctions, allows the optical absorption to be obtained from the imaginary part of the macroscopic dielectric function

$$\varepsilon_2(\omega) = \frac{16\pi^2 e^2}{\omega^2} \sum_S \left| \sum_{cv} A_{cv}^S < c|\hat{\boldsymbol{e}} \cdot \boldsymbol{v}|v > \right|^2 \delta(\Omega_S - \hbar\omega) \tag{4.22}$$

where $\hat{\boldsymbol{e}}$ is the polarization of the incident light and $\boldsymbol{v}$ is the velocity operator. Note Eq. 4.22 includes electon-hole interactions. The form without Coulomb interactions is given

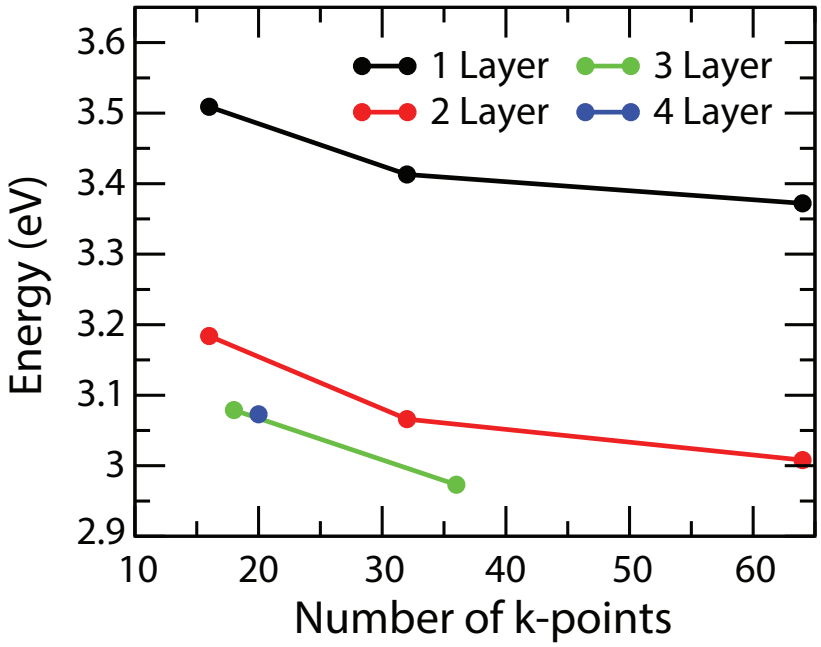

Figure 4.9: Calculated energies for the $n = 1$ exciton of PbI_2 as a function of the number of points sampled along the in-plane directions in k-space. Results for 1 through 4 layers are indicated by color.

by

$$\varepsilon_2(\omega) = \frac{16\pi^2 e^2}{\omega^2} \sum_{cv} |< c|\hat{\boldsymbol{e}} \cdot \boldsymbol{v}|v >|^2 \, \delta(E_c - E_v - \hbar\omega) \tag{4.23}$$

Note: These techniques are fairly accurate for moderately correlated electrons, but break down in strongly correlated systems where the perturbation approximation is no longer valid. Errors have been found to be $\approx$ 10 - 15% of the energies [41].

4.5.1 Exciton Calculations

After solving Eq. 4.20 for the excitation energies, the correlated electron-hole wavefunction can be determined from Eq. 4.19. To perform these calculations however, the spatial extent of excitons must be considered. Since they can extend over many unit cells, their energies can be very sensitive to the sampling density in the k-space. Performing the GW and kernel calculations on a much finer mesh though becomes computationally challenging and

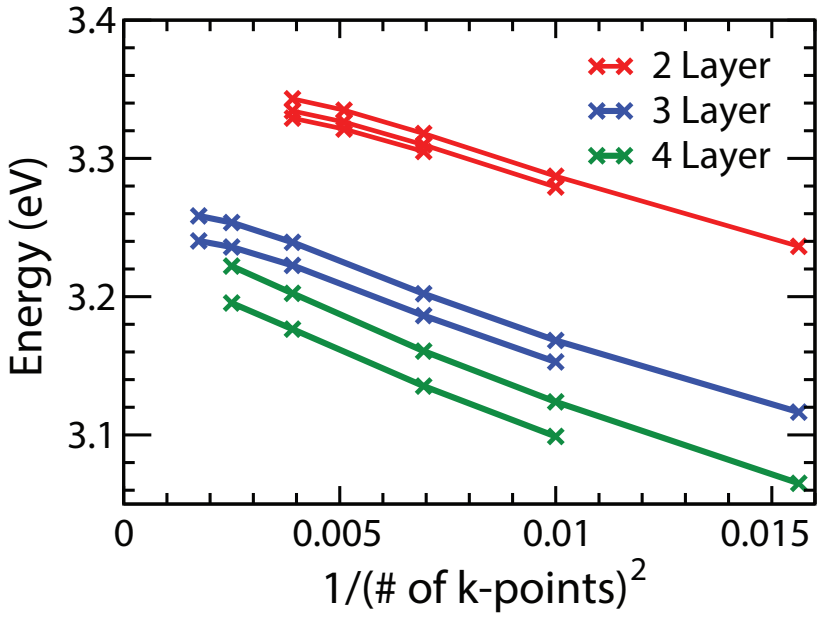

Figure 4.10: Calculated $n = 1$ exciton energies as a function of k-space sampling shown for 2, 3 and 4 layers. Respective curves for each structure correspond to GW eigenenergies calculated on 8x8x1, 10x10x1 and 12x12x1 coarse grids which were then interpolated on to the finer grid sizes for BSE calculations. The curves decrease in energy with increasing grid size.

in some cases impossible depending on the resources available. BerkeleyGW deals with this by interpolating the kernel calculation, which includes the screened Coulomb interaction and is done using the coarse GW mesh, on to a much finer mesh for the absorption calculation [36]. This procedure works well for bulk calculations and is especially critical because of the sheer number of points to calculate in three dimensions. However, for the layer structures the interpolation on to the fine grid was found to dramatically overestimate the binding energy calculated without the fine grid interpolations procedure by several hundred meV in some cases. Calculations with interpolation for PbI_2 are shown in Fig. 4.9, where the calculations for the densest grids yield energies below that of the bulk exciton energy. This effect is deemed to be unphysical and a result of underestimation of the screening in the interpolation process.

Based on the previous observation, exciton calculations for the layer structures were

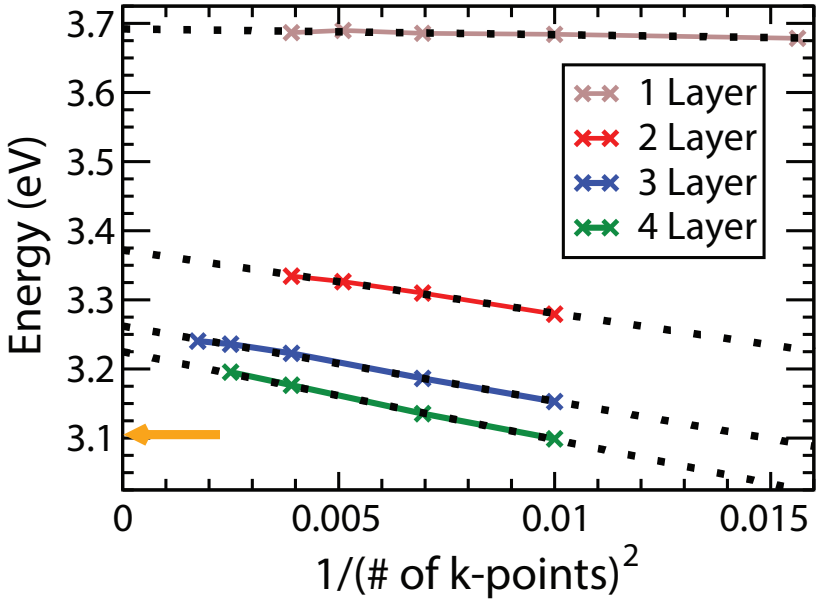

Figure 4.11: Exciton energies for 1, 2, 3, and 4 layers as a function of k-space sampling calculated as described in the text. GW eigenvalues used in the 2, 3 and 4 layers structures were calculated on a 10x10x1 grid. Dotted lines correspond to linear fits to each data set and give the exciton energy extrapolated to infinite sampling. The yellow arrow corresponds to the bulk exciton energy.

done separately by doing the BSE calculations on much denser coarse grids rather than than using BerkeleyGW's interpolation scheme. It becomes extremely computationally expensive to perform the entire GW and BSE calculation from start to finish using fully converged parameters and finer sampling grids. In fact, this was only possible to do for the case of the monolayer, which with fewer atoms in a unit cell is cheaper to calculate than the few-layer structures. Instead for the 2, 3 and 4 layer structures, we perform the BSE calculations on a denser grid, while using a lower epsilon cutoff, set to 4 Ry, and a lower number of bands, set to three times the number of valence bands. These parameters are critical in the accurate calculation of the GW energies but much less so for exciton energies, which allowed for the use of lower values and decreased computational requirements. To ensure accurate energies, the already converged GW eigenenergies were used by interpolating them separately on to the denser grid using BerkeleyGW's interpolation utility `inteqp`. In test cases with smaller grid sizes, the eigenenergies using this procedure were found to be within $\approx$ 0.01 eV of BSE calculations performed with fully converged GW cutoffs. Results are shown in Fig. 4.10 for 2, 3, and 4 layers, with different curves corresponding to fully converged GW eigenenergies on 8x8x1, 10x10x1 and (only for 2 layers) 12x12x1 coarse grids. A 10x10x1 coarse grid GW calculation was found to be sufficiently converged for these calculations, and the exciton energies were found to increase linearly with sampling as $\sim 1/k^2$ as shown in Fig. 4.11. The energies were extrapolated to infinite sampling, or $1/k^2 = 0$ using a linear fit to the calculated points to obtain the final $n = 1$ exciton energy for each structure.

4.5.2 Absorption

In addition to exciton energies, it is in principle possible to obtain the absorption spectrum for each structure from BSE calculations. This is done by determining the imaginary part of the permittivity using Eqs. 4.22 & 4.23. Results for bulk PbI_2 are presented in Fig. 4.12 with and without the inclusion of excitonic effects. As is expected from excitonic

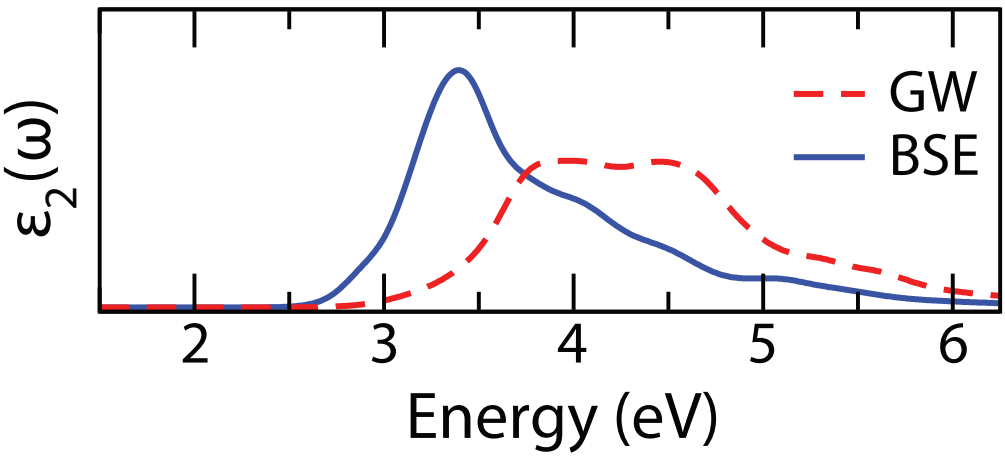

Figure 4.12: Energy spectra of the imaginary part of the dielectric response function calculated with (BSE) and without (GW) the inclusion of electron-hole interactions for bulk PbI_2. Spectra have been shifted down in energy by the magnitude of the spin orbit correction to the band gap.

effects [10], we observe a redistribution of oscillator strength towards the band edge in the spectrum including Coulomb interactions. Both spectra have been shifted down in energy by the spin orbit correction to the bulk band gap of 0.795 eV. Surprisingly, the BSE result bears little resemblance to the band edge absorption observed experimentally in Fig. 2.3, and instead increases slowly near the band edge. This discrepancy was found to be a result of not being able to include SO interactions in the BSE calculations. Using a spin orbit band interpolation code modified by Guangsha Shi to calculated the velocity matrix elements, we were able to calculate the imaginary part of the permittivity as well as the relevant matrix contributions as shown in Fig. 4.13. The results show that without the inclusion of SO effects the absorption for $E \parallel \hat{c}$ is proportional to $(E - E_0)^{1/2}$, which is consistent with a direct allowed transition, whereas the absorption for $E \perp \hat{c}$ fits much closer to $(E - E_0)^{3/2}$, the form for a forbidden transition [10]. When SO interactions are included, there is some mixing of the bands as discussed in Sec. 4.1.7, which leads to the absorption being allowed for both incident polarizations. The relevant matrix elements in-plane at $k_1 = 0$, where the band gap is located, confirm that without SO, the transition probability

is zero. Experimentally however, the oscillator strength is found to be four times larger for incident polarization $E \perp \hat{c}$ [16], which remains an unresolved issue with the calculations. Finally, we note that these results do not include excitonic effects because the BerkeleyGW code that performs the BSE calculations is not currently capable of including SO effects. Therefore, while these results do not completely agree with the experimental results, they are instructive to show the importance of SO effects in absorption profile of PbI_2.

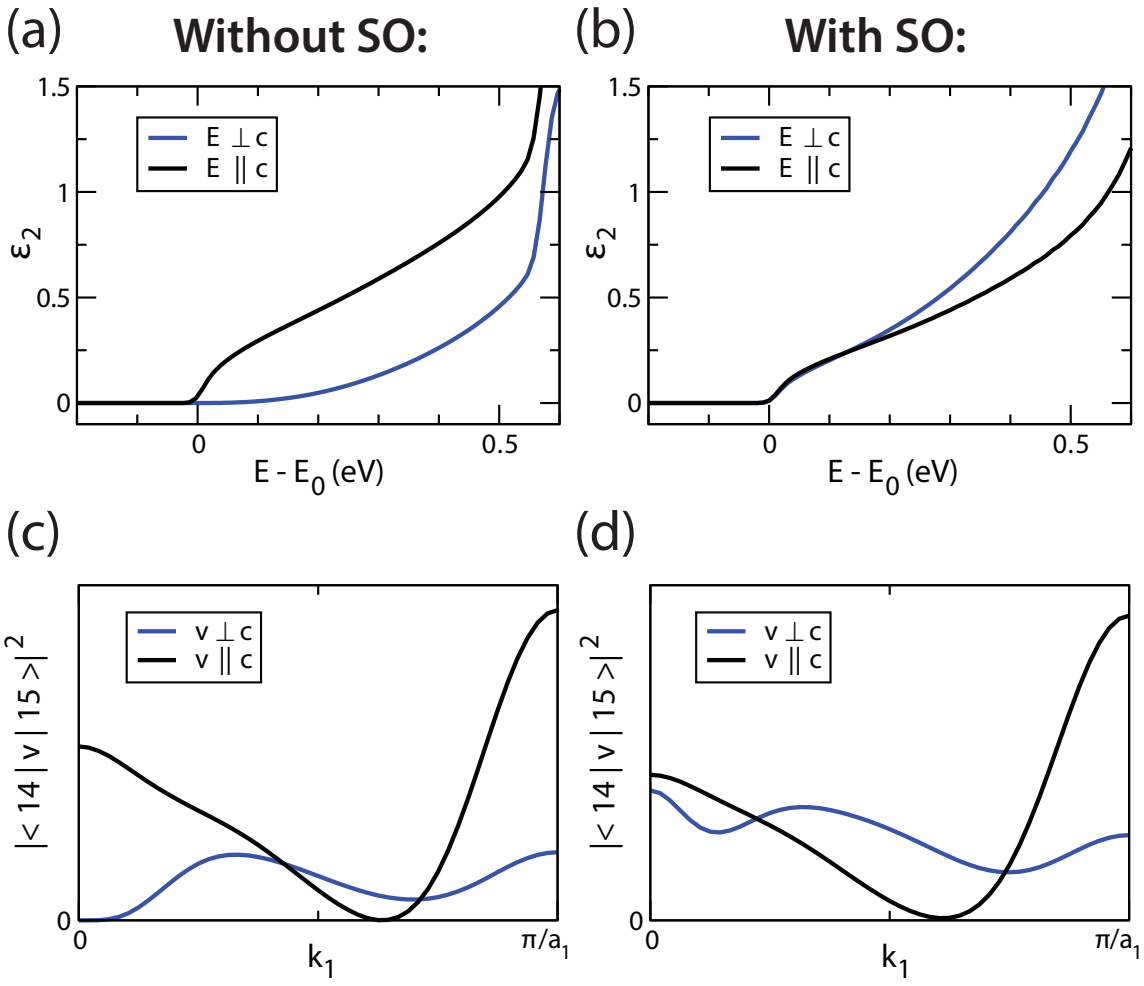

Figure 4.13: (a, b) Imaginary part of the dielectric response calculated for bulk PbI_2 as a function of energy relative to the band gap E_0. Results are shown without (a) and with (b) SO interactions. (c, d) Corresponding velocity matrix element calculations between the top valence band (14) and the lowest conduction band (15) as a function of the in-plane k_1 vector.

CHAPTER 5

Frenkel-like Wannier-Mott Excitons

In this chapter we present: Optical measurements and first-principles calculations of the band structure and exciton states in direct-gap bulk and few-layer PbI_2 indicate that the $n = 1$ exciton is Frenkel-like in nature in that its energy exhibits a weak dependence on thickness down to atomic-length scales. Results reveal large increases of the gap and exciton binding energy with decreasing number of layers, and a transition of the fundamental gap, which becomes indirect for 1-2 monolayers. Calculated values are in reasonable agreement with a particle-in-a-box model relying on the Wannier-Mott theory of exciton formation. General arguments and existing data suggest that the Frenkel-like character of the lowest exciton is a universal feature of wide-gap layered semiconductors whose effective masses and dielectric constants give bulk Bohr radii that are on the order of the layer spacing. The work in this chapter has been published in Ref. [42].

5.1 Introduction

Following the discovery of graphene [1], two-dimensional systems derived from van der Waals layered materials and, in particular, semiconductors have attracted much attention due to their unusual physical properties and possible applications, including the potential development of a new class of artificial superlattices resulting from the alternate deposition of highly dissimilar substances [2]. Recent work on few-layer semiconductors [43, 44, 45, 46, 47, 48] has shown that the energy of the lowest exciton associated with

the direct gap varies only weakly with layer thickness down to a few layers, a behavior usually associated with highly localized Frenkel excitons. This is in stark contrast with the strong dependence of the lowest direct or indirect gap [43, 44, 45] and confinement effects observed in semiconductor quantum wells based on, e. g., $Al_xGa_{1-x}As$ where the exciton energy and band gaps both increase dramatically with decreasing well width [20]. The observed Frenkel-like behavior is ostensibly in conflict with results indicating that excitons in these materials are not strongly localized; their radii are on the order of a few lattice constants[17, 13] and, on that basis alone, one would expect them to fall in a range intermediate between the Frenkel and Mott-Wannier cases. Here we present band-structure calculations, optical reflectance and photoluminescence (PL) measurements on bulk and atomically-thin PbI_2, which show that this layered semiconductor follows the pattern observed in other wide-gap layer systems for which both the gap, E_G, and the $n = 1$ exciton binding-energy, E_B , exhibit large increases with decreasing thickness while the exciton energy, $E_G - E_B$, hardly changes. Results are in reasonable agreement with a simple model based on the effective-mass approximation. Relying on this model and available data, we present a plausible explanation as to why the lowest exciton is Frenkel-like and argue that it is a generic property of wide-gap layered semiconductors.

PbI_2 is a van der Waals system whose most common polytype, $2H$, crystallizes in the layered CdI_2 structure [8]. As such, it is a good candidate for two-dimensional studies since crystals can be easily cleaved due to the weak inter-layer bonding, and samples of arbitrarily small thickness can be produced [1]. The optical properties and the electronic structure of bulk PbI_2 were extensively studied in the late 1960s and early 1970s [13, 49, 6, 16]. Below the fundamental direct gap, E_0 = 2.55 eV, experiments at $\sim$ 4 K reveal a prominent quasi-hydrogenic exciton series for which the binding energy of the lowest, $n = 1$ state is $E_B \sim 55$ meV [13]. We note that, owing to increased interest in this material for x-ray and γ-ray detection applications, techniques for growing single-crystals of PbI_2 have greatly improved in recent years [50].

5.2 Experimental Results

Few-layer samples were mechanically exfoliated [1] from bulk $2H$ PbI_2 crystals and deposited on silicon wafers covered by a 285-nm-thick oxide layer. Measurements were made over a large range of thicknesses on optically uniform samples. PL measurements were done at 4.5 K. As excitation, we used $\sim$ 15 μW from a 476.5 nm Ar^+ laser line. Reflectivity measurements were performed at 77 K using a tungsten-halogen lamp. The incident light was focused using long-working-distance 50$\times$ and 100$\times$ microscope objectives, which gave spot sizes of $\sim$ 5 and 2 μm in diameter, respectively. Sample thicknesses, given here in units of the c lattice parameter L $\sim$ 7 Å[8], were estimated from atomic force microscopy. Thickness uncertainties are explicitly indicated for few-layer samples; the estimated error for thicker samples is $\sim$ 5 layers.

Reflectance measurements are shown in Fig. 5.1 (a). The arrows, labeled FX, indicate the peak energy of the $n = 1$ exciton in the corresponding reflection simulations for PbI_2 on a Si/SiO_2 substrate. The oscillations observed in the samples with 1290 L and 419 L are due to interference effects from multiple reflections. As shown in the figure, these assignments are supported by the simulations and agree with earlier measurements on bulk PbI_2 [13, 49]. PL spectra are presented in Fig. 5.1 (b). In the thickest sample we observe three main peaks, two of which, $e - h$ (donor-acceptor) and BX (bound exciton), are associated with impurities [51] while the highest-energy band FX is due to free-exciton recombination. The FX energy from PL is in excellent agreement with values from reflectance measurements. Interestingly, the observed emission intensities of e-h and BX decrease much more rapidly than FX with decreasing thickness and are not visible in the few-layer crystals.

The most striking feature of the PL and reflectance data is the extremely weak width-dependence of the absolute exciton energy. Aside from small ($\lesssim$ 10 meV) random shifts in the FX position attributed to a sparse presence of the $4H$ polytype [13, 51], it is only in samples below $\sim$ 10 monolayers that a significant blue shift ensues as a result of confinement. This shift is clearly visible in the PL spectra of the thinnest samples, which exhibit

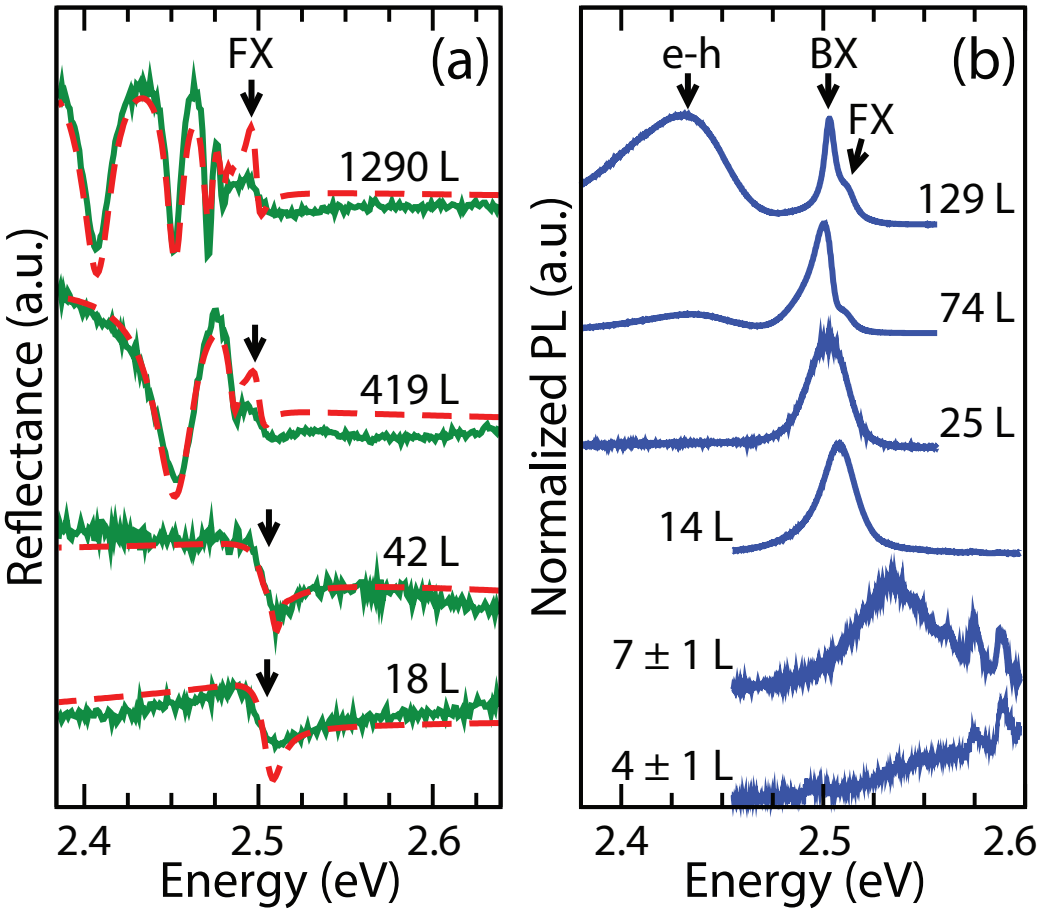

Figure 5.1: (a) Reflectance spectra at 77 K. FX denotes the position of the n = 1 exciton. Fabry-Perot oscillations are seen in the two thickest samples. Red-dashed curves are results of simulations using optical constants of bulk PbI_2 [13]. (b) PL data at 4.5 K. Spectra show free (FX) and bound (BX) exciton recombination, and emission due to donor-acceptor pairs (e-h).

additional, equally-spaced peaks on the high-energy side we ascribe to forbidden resonant Raman scattering [52] by A_{2u} and E_u longitudinal-optical modes at, respectively, 113 and 106 cm^{-1} [21] and its overtones. The observed larger PL broadening in ultrathin samples is tentatively attributed to enhanced sensitivity to strain from the substrate.

5.3 Computational Results

Theoretical band structures of bulk and few-layer PbI_2 were obtained from first principles calculations based on density functional theory (DFT) in the local-density approximation [53] using the QUANTUM ESPRESSO code [54] as well as the single-shot GW method [55] using the BerkeleyGW package [36]. Band structures were interpolated with the maximally localized Wannier function method [40]. In addition, exciton eigenstates and eigenvalues were determined using the Bethe-Salpeter-Equation (BSE) code within the BerkeleyGW package [55]. Spin-orbit coupling (SO) effects on the band structures were considered in a non-self-consistent way, as in Ref. [56], but they were ignored in the evaluation of the exciton wavefunctions. Due to the inherent difficulty in accounting for the van der Waals interaction, which determines the interlayer separation, we used atomic-position data for bulk crystals [8]. Parameters such as, e. g., the plane-wave cutoff energies and the k-grid sampling were chosen to converge the band gap and exciton energies separately to within ~ 0.1 eV.

Ab initio band structures are shown in Fig. 5.2. For simplicity, we plot only the 6 highest valence and 3 lowest conduction bands per layer, which derive predominantly from iodine $5p$ and lead $6p$ orbitals, respectively. Throughout most of the Brillouin zone, these states are separated by a few eV from other bands. Direct band gaps and corresponding k-space sampling used are listed in Table 5.1. For bulk PbI_2, we find a fundamental direct gap of 2.38 eV at the A point, which agrees relatively well with the experimental value, E_0 = 2.55 eV, and previous calculations with empirical pseudo-potentials [6]. The calculated

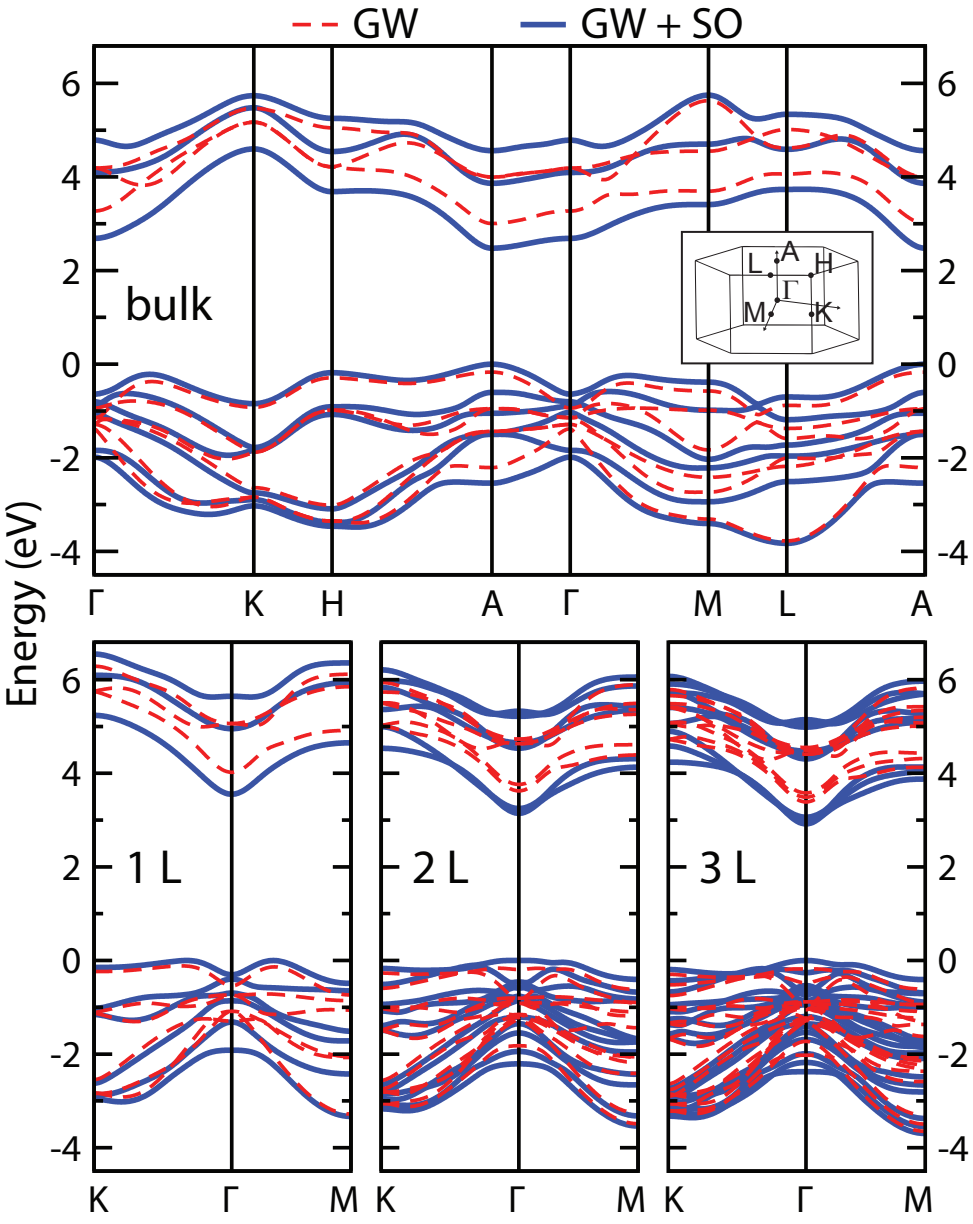

Figure 5.2: Band structures without (GW; dashed red) and with (GW+SO; solid blue) spin-orbit coupling. Results are shown along principal directions in the three- (two-) dimensional hexagonal Brillouin zone of bulk (few-layer) PbI_2, shown in the inset. The fundamental gap is direct (indirect) for bulk and 3L- (1L- and 2L-) PbI_2; calculated values are listed in Table 5.1.

Table 5.1: Direct gaps (eV) from DFT, GW, and GW with spin-orbit coupling (GW+SO) calculations and the k-grid used to sample the Brillouin zone. Gaps in bulk and few-layer PbI_2 are, respectively, at the A and Γ point.

STRUCTURE	LDA	GW	GW+SO	k-GRID
bulk	1.99	3.18	2.38	6x6x4
4 layer	2.07	3.49	2.67	10x10x1
3 layer	2.12	3.60	2.78	9x9x1
2 layer	2.24	3.82	3.01	8x8x1
1 layer	2.70	4.56	3.72	8x8x1

electron (hole) effective masses at the A-point, perpendicular and parallel to the $\hat{c}$-axis are $m_e^{\perp} = .21m_0$ ($m_h^{\perp} = .59m_0$) and $m_e^{\parallel} = 1.05m_0$ ($m_h^{\parallel} = .56m_0$), in units of the electron mass; the relevant states involve primarily p_z-orbitals. We briefly emphasize the importance of SO effects, which not only shrink the gap by ≈ 0.80 eV, as in Fig. 5.2, but also lead to a mixing of states that transforms the character of the direct-gap transition from dipole-forbidden (without SO coupling) to optically allowed.

Large increases in the gap due to quantum confinement are clearly observed in Fig. 5.2; note that the bulk A-point projects onto the Γ-point of the two-dimensional zone. The most significant changes occur for iodine-like states, reflecting the strong effect neighboring layers have on these atoms because of their position in the layers. Confinement effects are most prominent for the top p_z-like valence band, which develops a minimum at the Γ-point for a single monolayer such that the fundamental gap becomes indirect. The bilayer structure also results in an indirect gap slightly smaller than its direct gap; however, the difference is below the accuracy of the calculation. Interestingly, this behavior is the reverse of that of MoS_2 for which the gap is indirect except for the monolayer [43].

Central to our arguments concerning the Frenkel-like behavior of the lowest exciton are the properties of its wave function. Results of BSE calculations are shown in Fig. 5.3; as noted, they do not include the SO interaction although we believe that its inclusion would not significantly modify the exciton radii. Fig. 5.3 (a) shows the modulus squared of the $n = 1$ bulk wave function Ψ for a fixed hole position [57]. The calculated in- and

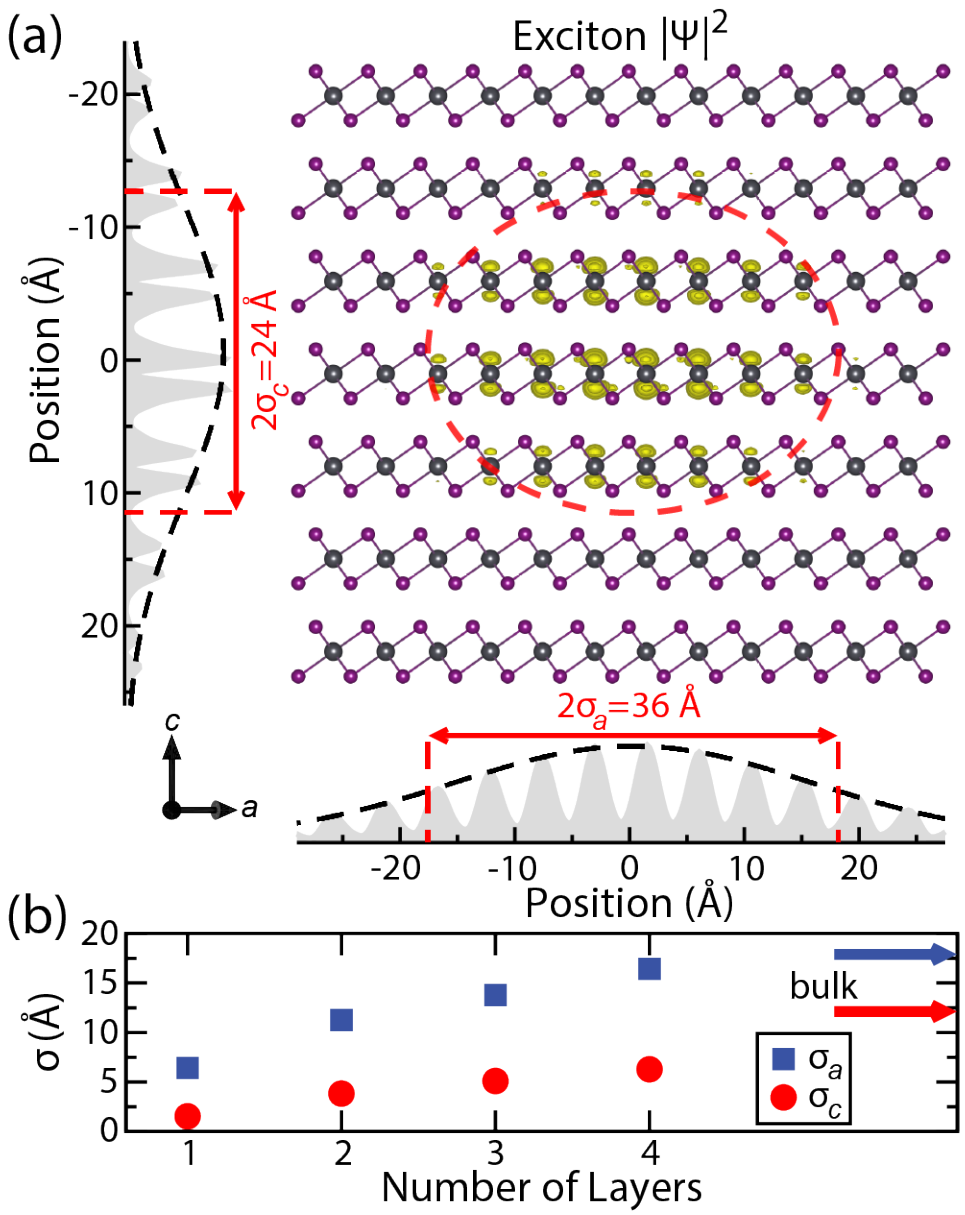

Figure 5.3: (a) Probability distributions for directions parallel (a-axis) and perpendicular (c-axis) to the layers for bulk PbI_2, with standard deviations (exciton radii) σ_a and σ_c. The central panel shows an isosurface corresponding to the value of $|\Psi|$ at the exciton radii. Black and purple balls represent, respectively, lead and iodine ions. The dashed-red curve is an ellipse centered at the position of the hole whose principal axes are the radii. (b) Radii vs. number of layers. Bulk values are indicated by arrows.

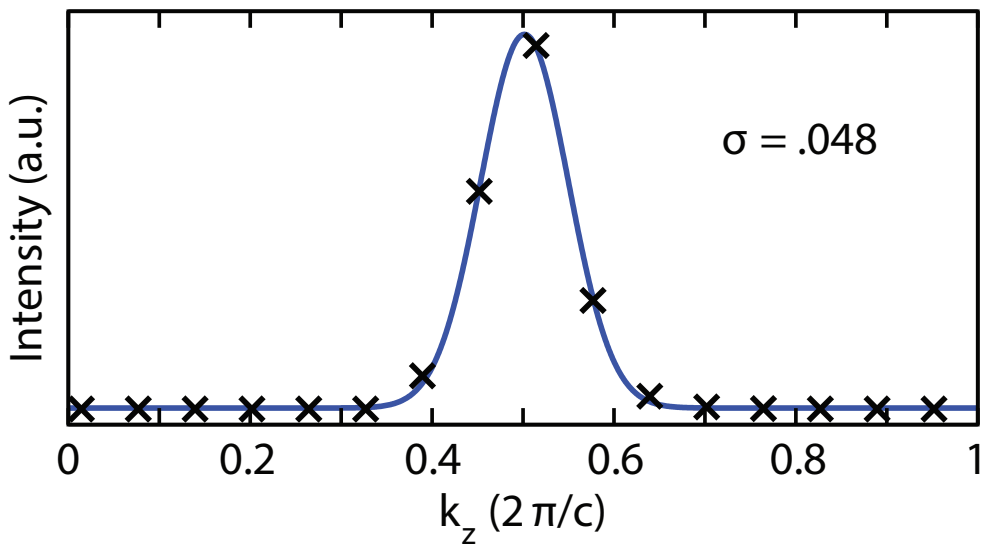

Figure 5.4: Calculated distribution of the $n = 1$ exciton in momentum space for bulk PbI_2. The curve is a fit to the points using a Gaussian distribution centered at k_z = 0.5 with the indicated standard deviation.

out-of-plane radii of the ellipsoidal envelope are 18 Å and 12 Å, which are very close to experimental values obtained assuming an isotropic mass tensor [49, 58], and a factor of, respectively, 4 and 1.7 larger than the corresponding lattice constants. These ratios are similar to those for II-VI semiconductors like CdS and ZnS, but much larger than for organic semiconductors such as picene ($C_{22}H_{14}$) [59]. As expected for hydrogenic systems, confinement enhances the Coulomb interaction as well as the binding energy, reducing in turn the exciton radii, and thereby causing a transition from borderline Wannier-Mott to Frenkel type; see Fig. 5.3 (b). It is interesting to note that the calculated size reduction from bulk to monolayer PbI_2 is a factor of approximately four, as for the ratio between three- and two-dimensional hydrogen [60]. We also observe that, while the $\hat{c}$-axis bulk radius is slightly less than the thickness of two atomic layers, the calculations indicate that the exciton wave function involves states with wavevectors that are spread over a width of $\approx 10\%$ of the size of the Brillouin zone from the A-point, see Fig. 5.4, and, thus, well within the range where the bands can be treated as parabolic.

The thickness-dependence of the energy of the $n = 1$ exciton from PL experiments and

that of the direct gap from GW+SO results are plotted in Fig. 5.5. The plot includes also SO-corrected values for the exciton from BSE calculations, obtained by subtracting the SO-induced red shift of the gap. This procedure is justified on the grounds that the introduction of SO coupling leads to a fairly rigid shift of the relevant bands by $\sim$ 0.8 eV (see Fig. 2 and Table I). Moreover, to correct for what we believe is a systematic layer-thickness-independent error due to the approximations involved in our first-principles calculations, all the theoretical results have been rigidly shifted upwards by 0.17 eV. For a discussion of the shift problem, see, e. g. Ref. [61, 41]. This value represents the difference between the measured [13] and calculated bandgap for bulk PbI_2 (note that, unlike the absolute energy, the calculated bulk exciton binding energy of 70 meV is in reasonable agreement with E_B = 55 meV from experiments [13]). It is apparent that, on account of this shift, the calculated exciton energies are in excellent agreement with the PL data.

Also shown in Fig. 5.5 are results of effective-mass calculations for a single electron-hole pair in an infinite square well for which the gap is $E_G = E_0 + \hbar^2\pi^2/2\mu^{\|}d^2$, where d is the sample thickness, $\mu^{\|} = m_e^{\|}m_h^{\|}/(m_e^{\|} + m_h^{\|})$ is the reduced mass and, as before, E_0 is the bulk gap. The electron-hole Coulomb interaction is $e^2/\varepsilon r$, where r is the relative coordinate and ε is the screening constant ($\varepsilon_{\|} = 6.25$ and $\varepsilon_{\perp} = 26.75$ in PbI_2 [21]). The exciton binding energy was calculated using a variational approach valid for GaAs-$Al_xGa_{1-x}As$ quantum wells [62]. This procedure gives values of the binding energy, which are in agreement with the exact results $2e^2/\varepsilon a_0$ for the two-dimensional limit [60] and $e^2/2\varepsilon a_0$ for $d \gg a_0$; a_0 is the bulk exciton radius. The results for $\varepsilon = \infty$ (non-interacting pair) agree relatively well with GW+SO calculations for the gap down to one monolayer whereas those for $\varepsilon = 9.5$ are in very good agreement with experimental and theoretical exciton energies down to $\sim$ 3 layers. Moreover, the model predicts negligible (i.e., less than 10 meV) confinement effects for samples thicker than $\sim$ 15 layers. As the layer thickness approaches the atomic limit, we expect effective-mass models to break down and, moreover, exciton parameters to become more and more affected by the surrounding

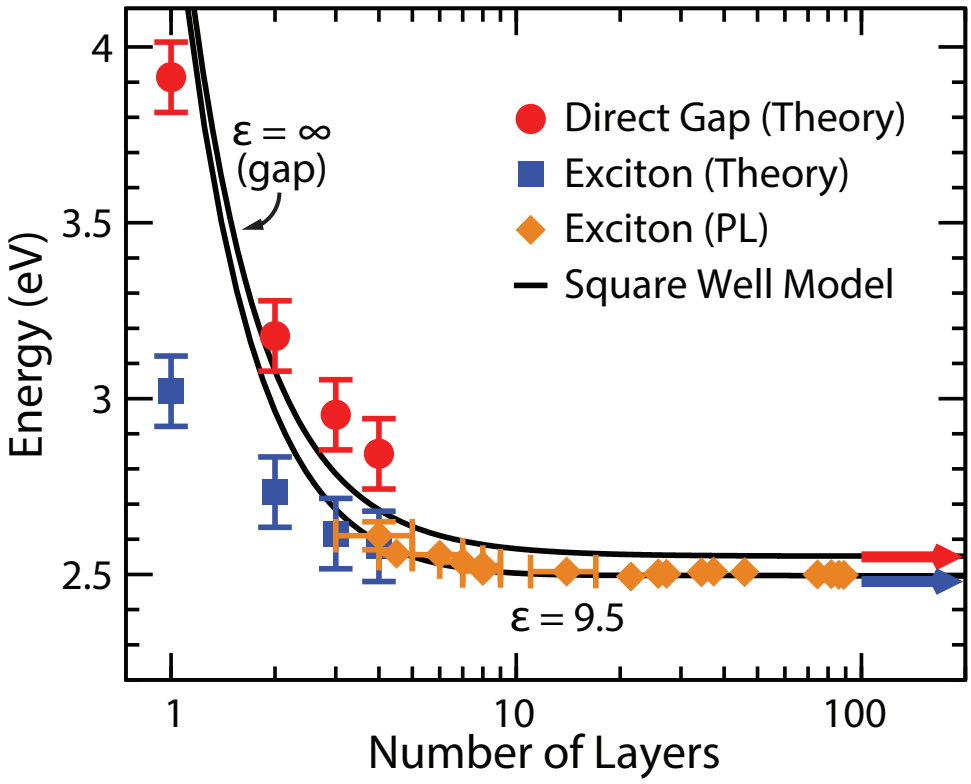

Figure 5.5: Calculated results for the direct gap (red circles) and the n = 1 exciton (blue squares) of few-layer PbI_2. The theoretical data have been rigidly shifted upwards by 0.17 eV to match the band gap of bulk PbI_2; see text for an explanation. Arrows give bulk theoretical values. Orange diamonds are free-exciton data from PL experiments. Also shown are effective-mass-approximation predictions for the lowest-energy exciton and unbound electron-hole pairs ($\varepsilon = \infty$) in an infinite square well.

dielectric [44, 46]. This applies in particular to mono- and bilayer crystals for which the square-well model strongly underestimates the binding energy.

5.4 Conclusions

The totality of our results suggests a simple explanation as to why the lowest exciton in PbI_2 and other wide-gap layer systems behaves in a Frenkel manner with decreasing thickness. First, we emphasize the fact that, while the approximation is strictly valid in the Wannier-Mott limit, effective-mass calculations are in good agreement with the PL data and GW+SO results down to atomically thin crystals. It is easy to see that, according to the exciton-in-a-box model, the exciton energy in the limits $d \ll a_0$ and $d \gg a_0$ are, respectively, $E_0 - 4E_B + \hbar^2\pi^2/2d^2\mu^{\parallel}$ [62] and $E_0 - E_B + \hbar^2\pi^2/2d^2M^{\parallel}$ [63]. Here, $M^{\parallel} = m_e^{\parallel} + m_h^{\parallel}$ is the $\hat{c}$-axis exciton mass. From these expressions, we obtain the crossover length $l \sim a_0(1 - \mu^{\parallel}/M^{\parallel})^{\frac{1}{2}} \sim a_0$ and, thus, the thickness below which confinement effects become important. It follows that the observed Frenkel-like behavior is simply the result that the interlayer thickness is on the order of the $\hat{c}$-axis bulk Bohr radius.

5.5 Supplementary Information

5.5.1 Reflection Calculations

Fits to the reflection data shown in Fig. 5.1 were performed using the transfer matrix method to account for reflections from the SiO_2 and Si substrate layers. Expressions for the optical constants for the substrate were taken from Ref. [64, 65]. A convenient analytic expression for the complex dielectric function of a semiconductor including excitonic effect was used to approximate the optical constants of PbI_2 [66]. The slightly modified

expression used for the three dimensional case is given by

$$\varepsilon(E) = \varepsilon_0 + A\frac{16R}{E_0 - R}\frac{1}{(E_0 - R)^2 - (E + i\Gamma_1)^2} + B\frac{1}{(E + i\Gamma_2)^2}\ln\left(\frac{E_0^2}{E_0^2 - (E + i\Gamma_2)^2}\right) \tag{5.1}$$

where R corresponds to the binding energy and E_0 the fundamental band gap. $\Gamma_{1,2}$ are broadening parameters, which along with ε_0 and A, B were used as fitting parameters and allowed to vary slightly from sample to sample.

The fits are in qualitative agreement with the experimental spectra but rarely gave exact fits around the band edge. There are a number of factors that may influence this agreement from the exact thicknesses of the samples and oxide layer as well as any water or other adsorbed particles between the samples and substrate. Varying stress from sample to sample may also play a role. Finally, Eq. 5.1 does not account for higher exciton states or other features that may arise in the absorption spectrum at the band edge. However the fits, are able clearly distinguish the band edge absorption from multiple reflection effects and provide a clear indication of the their trends above and below the gap as a function of thickness.

5.5.2 Temperature Dependence

Typically Wannier excitons are unstable at room temperature because their binding energies are on the order of the thermal energy $kT \approx 25$ meV. One potential indication of an increasing binding energy in thin samples would be the persistence of exciton PL at higher temperatures. For this reason, exciton PL measurements as a function of temperature were performed as shown in Fig. 5.6. It is interesting that the PL signal decreases rapidly with increasing temperature and appears to quench far below room temperature. This might be somewhat surprising given the bulk binding energy of ≈ 55 meV. However, PL is known to be strongly influenced by defects and impurities, which are likely to lead to non-radiative recombination pathways with increasing temperature. Thus no direct conclusions could be

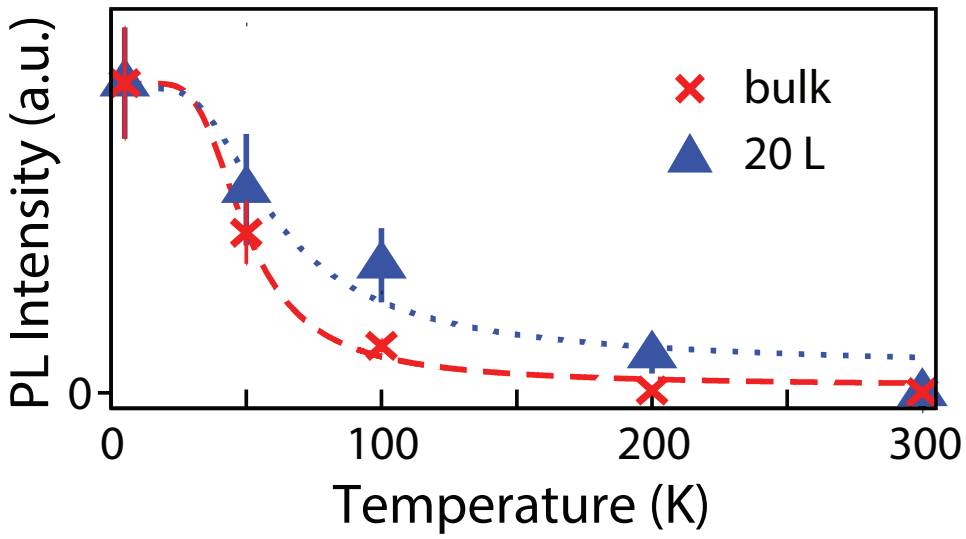

Figure 5.6: Integrated PL intensity as a function of temperature for a bulk and 20 layer sample. For the purposes of comparison, the intensities of each sample have been normalized to their respective intensities at 5 K. The lines correspond to fits to the data using an Arrhenius equation.

drawn about the binding energy from this data, but the temperature dependence is useful knowledge nonetheless and is the reason it is presented here. Reliable measurements on thinner samples were not obtained. This was primarily because this measurement was only performed using the 50x collection objective, which resulted in a weak signal, but also because even with the 100x collection objective, the signal in few-layer samples was already very weak at 5 K so no attempts were made at higher temperatures.

5.5.3 Effective Mass Calculations

Having calculated the complete band structure of bulk PbI_2, it is possible to determine the effective mass of electrons, m_e, and holes, m_h, near the band gap. Fitting the lowest conduction and highest valence bands to a parabolic function of the form given by Eq. 2.4 should give these masses. However, the bands at an M_0 critical point are typically only parabolic very near to the band minimum, and become more linear further away. This

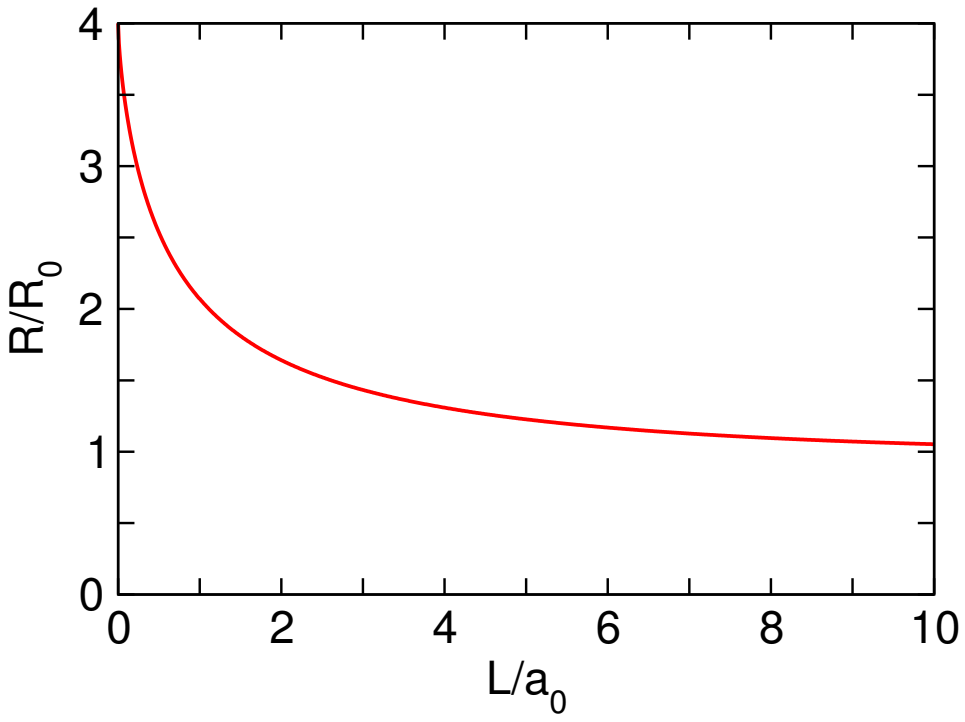

Figure 5.7: Exciton binding energy trend with confinement as calculated by Bastard [62], where R_0 is the binding energy and a_0 the bulk exciton radius.

complicates the fitting because the mass will be affected by the band region over which the fitting is done. A slightly better approximation of the masses can therefore be obtained using a hyperbolic fit of the form

$$E(\boldsymbol{k})(1+\alpha E(\boldsymbol{k})) = E_0 + \frac{\hbar^2}{2m_e}(\boldsymbol{k}-\boldsymbol{k}_0)^2 \tag{5.2}$$

where α is a fitting parameter for the linear contribution. The effective masses of PbI_2 were obtained using hyperbolic fitting to the top valence and lowest conduction bands obtained from LDA calculations around the A-point. As mentioned earlier, the obtained electron (hole) masses perpendicular and parallel to the $\hat{c}$-axis are $m_e^{\perp} = .21m_0$ ($m_h^{\perp} = .59m_0$) and $m_e^{\parallel} = 1.05m_0$ ($m_h^{\parallel} = .56m_0$).

5.5.4 Square Well Model

For the purposes of the effective mass calculations shown in Fig. 5.5, few-layer samples were approximated by an infinite square potential. The confinement energy of a particle in an infinite square well as a function of well width is well known. In the case of the electronic bandgap, the particle mass is replaced by the reduced mass of the electron and hole along $\hat{c}$. However, there is no simple corresponding analytical expression to obtain the Coulomb interaction energy with well width. Exciton binding energy as function of well width was calculated for a square well by Bastard by assuming a form for the wavefunction and performing a variational calculation [62]. The results of those calculations were fit with excellent agreement to the analytic expression

$$f(x) = 4 - 3\left(\frac{x}{1+x}\right)^{2/3} - 0.18\left(1 - e^{-0.28x}\right) + 0.18\left(\frac{2\arctan(x/30)}{\pi}\right) \tag{5.3}$$

This function is shown in Fig. 5.7, and the total energy, confinement minus binding energy, is shown in Fig. 5.5 for $\varepsilon = 9.5$, which gives the appropriate bulk binding energy.

CHAPTER 6

Multiphonon Resonant Raman Scattering in Few-Layer PbI_2

Resonant Raman scattering (RRS) is a technique that can be used to study electronic transitions including excitons as well as defect and impurity states in detail. The scattering cross-sections of normally forbidden modes can become extremely strong near resonance with certain electronic transitions and in particular excitonic transitions. At the same time, RRS can lead to diverse effects driven by different mechanisms, and a fairly comprehensive review of resonant scattering effects can be found in Refs. [24, 67]. The focus of this chapter is on multiple phonon resonant Raman scattering in bulk and few-layer exfoliated PbI_2 crystals. Section 6.1 begins with a brief overview of multiphonon RRS and is followed by a review of the work performed on exfoliated PbI_2.

6.1 Background

The Fröhlich interaction which was introduced in Sec. 2.5.2, plays an important role in LO phonon scattering near exciton energies at the fundamental direct band gap of polar semiconductors. Enhanced scattering from the forbidden LO phonon has been observed in a number of materials near resonance. One of the best examples is that of cadmium sulfide. Martin [68] showed, in the case of CdS, that the cross section for forbidden 1-LO scattering can increase dramatically, overtaking the allowed TO scattering, as the incident light

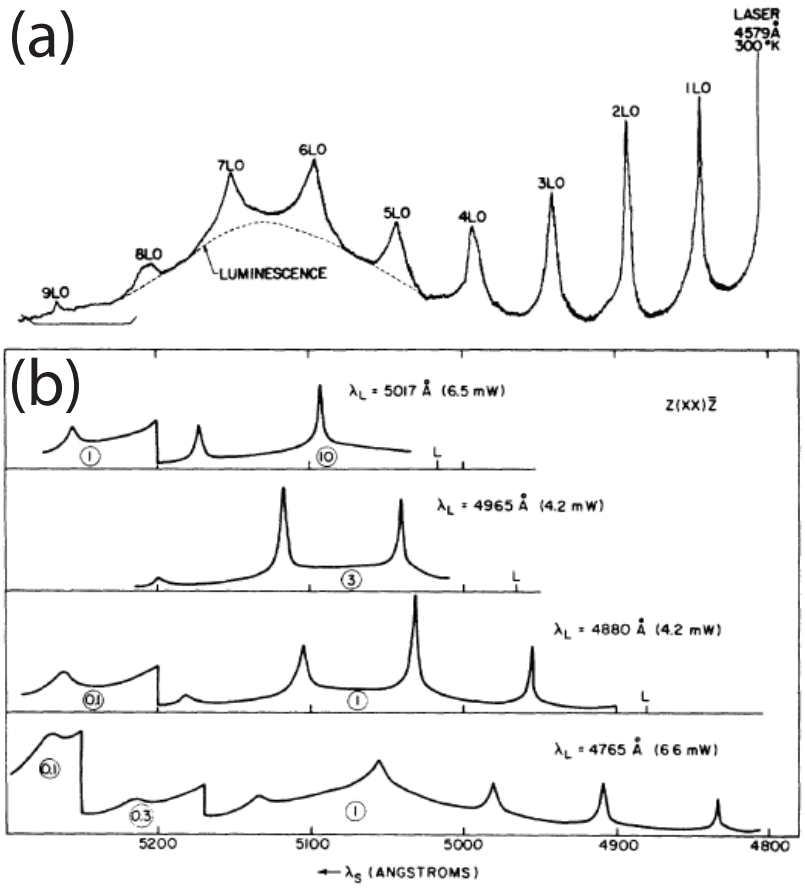

Figure 6.1: Examples of multiple phonon resonant Raman scattering in CdS from (a) Ref. [69] and (b) Ref. [70].

approaches the $n = 1$ exciton energy. Calculations using idealized Wannier exciton states show that all the intermediate states, below and above the continuum, must be included to obtain an accurate description of the cross section, except very close to resonance where the the sum can be limited to just one intermediate state for the incident photon. This effect demonstrates the dominant role played by the Fröhlich coupling near resonance in the enhancement of LO phonon scattering.

In addition to a dramatic increase in the scattering cross-section of first-order LO modes, the Fröhlich interaction can lead to the appearance of higher order modes near resonance. Multiple order LO phonon scattering has been observed in a number of polar crystals, including CdS, ZnTe, ZnSe, InAs and GaP [71] as well as ZnO [72], GaSe [73, 74] and even

PbI_2 [75]. The number of overtones observed in a material appears to be correlated with their polaron coupling coefficients [76]. The best know example of multiphonon scattering in polar crystals is found in CdS, which exhibits sharp peaks up to the ninth LO-phonon overtone when excited above the gap close to resonance [69, 70]. These results are shown in Fig. 6.1. One of the striking features of this data is that the overtone intensities do not appear to decrease rapidly as would be expected from higher order processes. However when exciting below the gap, very different behavior is observed with only up to the second order peak visible.

Typical Raman processes cannot be used to fully rationalize the observation of such strong scattering of n phonons simultaneously or iteratively [71]. Therefore a cascade model was proposed by Martin and Varma [77], which has in varying forms become the most widely accepted mechanism [78]. For a brief review of the cascade model see Ref. [10]. The process involves the absorption of an incident photon and creation of an exciton with the emission of an LO phonon. This is followed by the successive relaxation of the exciton through the emission of LO phonons, and finally the radiative recombination of the exciton with an additional phonon producing a photon at the scattered frequency. The scattering probability is described phenomenologically by decay times [10]

$$P_n \propto \alpha_{LO} \left(\frac{\tau_{LO}}{\Gamma(\boldsymbol{K}_1)}\right)\left(\frac{\tau_{LO}}{\Gamma(\boldsymbol{K}_2)}\right)\cdots\left(\frac{\tau_{LO}}{\Gamma(\boldsymbol{K}_{n-2})}\right)\left(\frac{\tau_{rad}}{\Gamma(\boldsymbol{K}_{n-1})}\right) \tag{6.1}$$

where α_{LO} is the LO assisted exciton absorption, τ_{LO} is the decay rate of the exciton state through LO phonons, τ_{rad} is the radiative decay rate of the exciton with LO phonon emission, and Γ is the exciton damping. This type of model gives relatively good agreement for relative scattering strengths of the overtones in CdS [77]. A more rigorous microscopic approach has also been developed by Zeyher [78].

We note that in all cases, the overtones are observed to be multiples of the first order LO phonons and are assigned to scattering by zone center phonons [69, 71]. In a perfect

bulk crystal, conservation of momentum requires that $\boldsymbol{q} = \boldsymbol{k}_i - \boldsymbol{k}_s$. It has been shown [79] that exciton-LO phonon Fröhlich interaction is proportional to q^2 for small q and a maximum for $qa_0 \approx 2$, with a_0 the exciton radius. Thus, in the case of forward scattering, where $\boldsymbol{q} \approx 0$, the scattering intensity is also expected to be ≈ 0, and the scattering intensity is expected to be at its maximum in backscattering, where $\boldsymbol{q} = {}^{4\pi n}/_{\lambda}$. However, when momentum conservation is broken, by impurities or confinement for example, the forward scattering may be non-zero. Generally the scattering was reported to be independent of polarization. The width of the peaks is attributed to the anisotropy of the crystals and given by the difference in phonon energies near zone center. This accordingly leads to increased broadening in the n-LO peaks [72].

Observation of multiple higher order scattering peaks are common in small molecules and ions in doped crystals[80]. This effect is typically understood using a configuration coordinate model. Similar models have also been developed to account for multiphonon LO scattering in polar crystals [52, 81]. Such a configuation-coordinate model was developed to interpret LO phonon overtones observed at slightly different energies in reflectance and Raman spectra of YbS [52]. Good agreement was obtained using a phenomenological effective displacement to fit the scattering intensity and reflectance spectra.

6.2 Introduction

Raman scattering (RS) and photoluminescence (PL) spectroscopy measurements are important tools in the characterization of semiconductors and have proven to be of particular importance to the thriving area of research on two-dimensional van der Waals crystals. Examples of note include the single 2D peak observed in RS of monolayer graphene [82], as well as shifts in the phonon frequencies in RS [45, 83] and exciton induced luminescence in PL [43, 84] observed in few-layer transition metal dichalcogenides. These techniques have been used to identify differences in the thickness and quality of atomically thin layers, but

their signals can be weak and difficult to measure reliably especially with the low incident powers required to avoid sample heating. This is especially true in the case of PbI_2, where the luminescence is expected to quench as the band gap becomes indirect in the monolayer thickness limit [42]. In this paper, we demonstrate the aptitude of multiphonon resonant RS in effectively probing few-layer samples of PbI_2. Changing the number of layers in an ultrathin sample causes small shifts in the exciton energy, which can be difficult to clearly distinguish by absorption or luminescence. However, small changes to the exciton energy may result in large changes to the relative intensity of multiphonon scattering peaks, thus providing a clear signature of thickness changes down to a mere single atomic layer. This approach provides a rapid low-power method of characterizing few-layer polar crystals, and is a particularly useful means of obtaining enhanced signal despite the significantly diminished emission and scattering volumes in ultrathin samples.

Resonant Raman scattering is a well-known phenomenon, which can be accurately described using third-order perturbation theory when incident radiation is near a resonance with the electronic transitions of a material [67]. Scattering near exciton states is known to be especially strong, exhibiting enhanced Raman allowed scattering, recently demonstrated in few-layer MoS_2 [85], as well as strongly enhanced Raman forbidden scattering of longitudinal optical (LO) modes due to the Fröhlich interaction in polar crystals [24]. What's more, when exciting polar semiconductors with radiation above the band gap, strong higher order LO scattering has been observed, with the most notable example of CdS displaying peaks up to the ninth order [71]. Several theories have been proposed to explain these results, most notably a cascade model [77] and models based on a configuration coordinate [52], which are based on the strength of the Fröhlich interaction between LO phonons and electron-hole pairs near resonance. One measure of this interaction is the Fröhlich or polaron coupling constant [76], which estimated for PbI_2 using calculated electron and hole masses [42] and experimentally obtained dielectric constants [86], gives a value of 2.1 (2.7) for electrons (holes). This value is comparable to those of alkali halides and serves

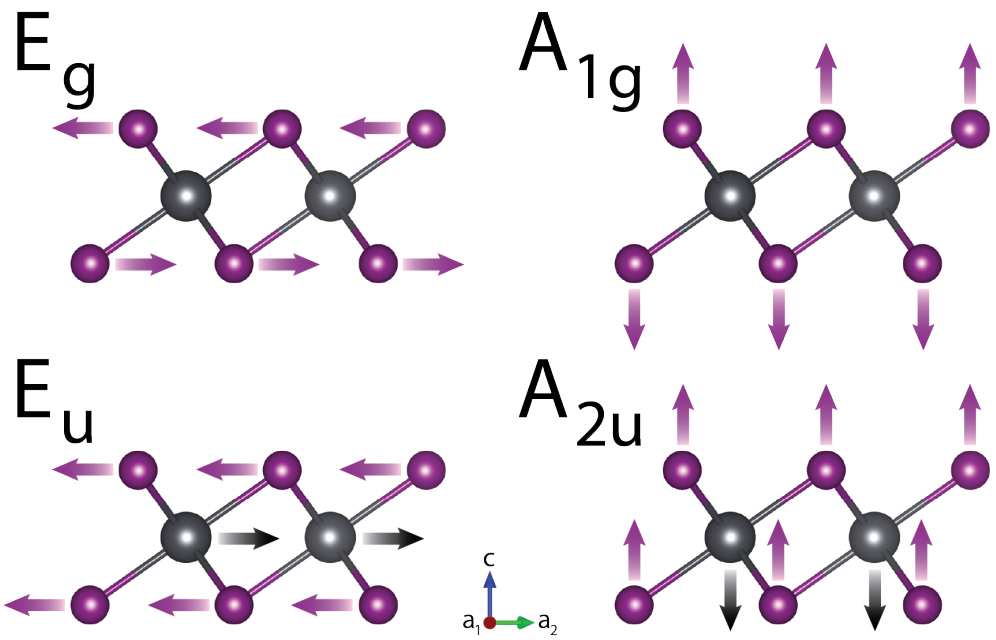

Figure 6.2: Schematic figure of the atomic displacements within a layer of the optical phonon modes of PbI_2.

as indication of the strong Fröhlich coupling in PbI_2 which can be attributed to its large ionicity.

We present, herein, the observation of multiple LO phonon scattering superimposed on luminescence around the lowest exciton state in few-layer PbI_2 samples. Bulk $2H$ PbI_2 has a fundamental band gap of 2.552 eV and exhibits strong exciton lines in its absorption spectrum just below the band edge [13]. It has a hexagonal layered structure belonging to the point group D_{3d} and has 9 vibrational modes, of which, two are Raman allowed, the E_g and A_{1g} modes, and two are infrared active, the E_u and A_{2u} modes. A schematic of the displacements of these modes is shown in Fig. 6.2. The phonon modes have been previously studied using both RS [21, 87] and infrared reflectivity [21, 86], and near resonance, the observation of forbidden scattering from the E_u and A_2u LO modes as well as their 2-LO counterparts has been reported [21, 88]. Weak higher order LO scattering peaks up to the sixth order have also been observed on the high energy tail of PL [75]. This data is shown in Fig. 6.3. However, the 1-LO was not observed at all in this case, while the higher

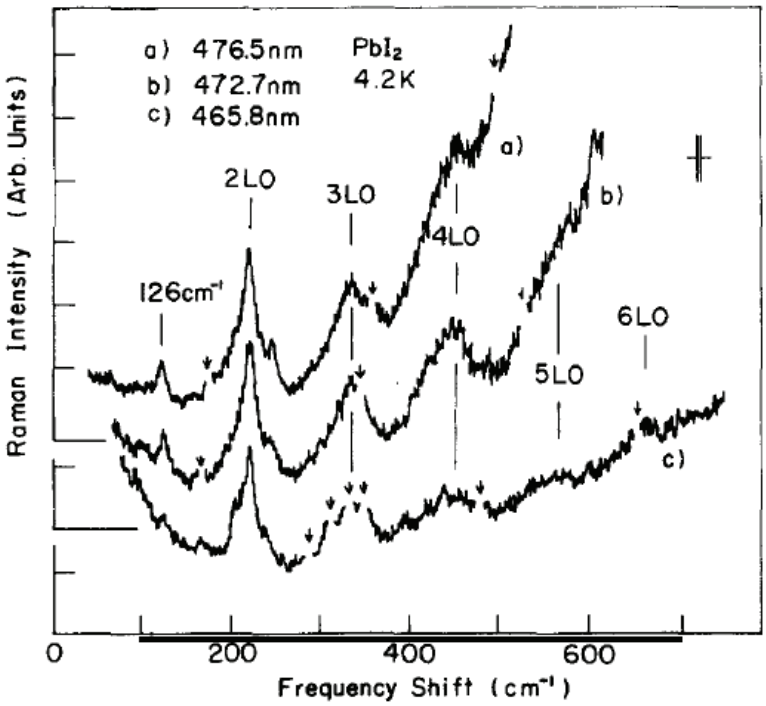

Figure 6.3: Multiple phonon resonant Raman scattering in bulk PbI_2 from Ref. [75].

order peaks were overwhelmed by strong PL and A_{1g} scattering very near to resonance. In contrast to traditional resonant RS, where the resonance is approached by tuning the frequency of the exciting laser source in the vicinity of the excitonic transition, we demonstrate here the ability to tune the exciton energy directly. Below $\sim$ 10 layers, the exciton energies in PbI_2 begin to increase dramatically [42], and we show that these changes can be sensitively probed by observing the relative intensity of the LO phonon overtones using fixed excitation sources. Additionally, tuning the resonance with thickness provides an interesting means by which to probe the electron-phonon coupling strength in few-layer structures where the exciton parameters are affected by confinement. With the use of the proper tunable source, this technique could, in principle, be used to map out exciton states in the susceptibility as reported for few-layer MoS_2 [85].

6.3 Methods

Samples were prepared from a bulk $2H$ PbI_2 crystal grown using the Bridgman method [50]. Few-layer crystals were then mechanically exfoliated using the methods employed for other two-dimensional crystals and deposited on a silicon wafer with a 90 nm oxide layer for optical identification [1]. Sample dimensions ranged from approximately 5 - 50 μm, and sample thicknesses were determined based on atomic force microscopy measurements. Estimated error in few-layer sample thicknesses are explicitly indicated in the figures below, while for thicker samples, the error is estimated to be within 5 atomic layers. As excitation, a 3.054 eV diode laser was utilized in addition to the 2.602, 2.541 and 2.410 eV lines of an Ar^+ laser, and spectra were recorded using a Dilor XY triple grating spectrometer. Due to the nature of the samples, a long working distance 100x microscope objective was used in a backscattering geometry to focus the excitation on areas of interest and simultaneously collect emitted and scattered light. Thus, the incident excitation was primarily along $\boldsymbol{k} \parallel \hat{\boldsymbol{c}}$ with $\boldsymbol{E}$ in the plane of the layers, however due to the focusing of the objective there is also a non-negligible component with $\boldsymbol{E} \parallel \hat{\boldsymbol{c}}$. Unless otherwise noted, the incident laser power for all measurements was ~ 30 μW, which was found to be sufficient to avoid any sample heating issues, and measurements were performed at 5 K.

6.4 Results

Figure 6.4 (a) presents a typical image of samples on which measurements were performed. Red circles indicate the areas on which the laser excitation was focused and from which emission was collected. Areas of different thickness are visible, and can be easily distinguished by their contrast with the substrate. As the number of layers increases, the contrast increases and the color of the samples shifts to a lighter shade of blue. We display the corresponding luminescence spectra for these samples, in Fig. 6.4 (b), obtained using a laser source near resonance with the fundamental bulk band gap at 2.602 eV, as well as one far

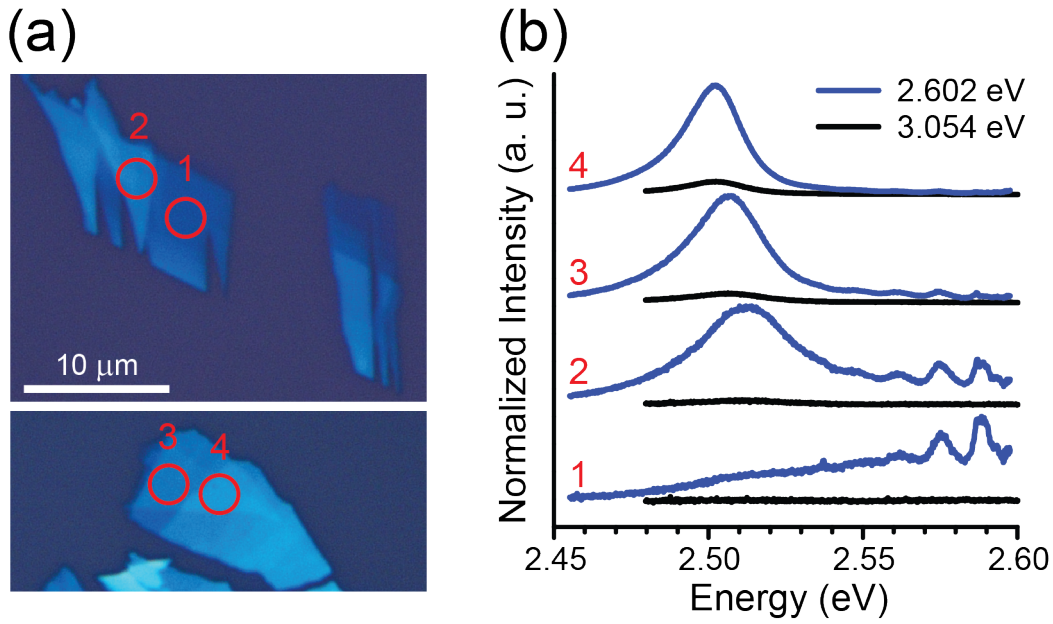

Figure 6.4: (a) Optical microscope images of PbI_2 samples. Red circles indicate areas that were probed optically in PL experiments. (b) Luminescence spectra, of samples shown in (a), measured using two different excitation sources, 3.054 and 2.602 eV, at 5 K. Intensities have been normalized to the joint maximum for each sample.

above at 3.054 eV. The spectra show a luminescence peak near $\sim$ 2.5 eV that corresponds well with the lowest $n = 1$ exciton energy, and appears to shift to higher energy with decreasing thickness. It is clear from the figure that the near resonant excitation, yields significantly stronger luminescence derived from radiative recombination of excitons. This may be due to a number of factors, including enhanced absorption and a lower probability of non-radiative decay near resonance, but it serves to demonstrate the importance of the excitation energy when probing ultrathin samples. Moreover, we observe peaks that appear near the laser line in the 2.602 eV spectra, and grow stronger relative to the PL with decreasing thickness. These are ascribed to resonantly enhanced scattering and discussed later on.

In a previous publication we discussed changes in both the fundamental band gap as well as the $n = 1$ exciton energy with decreasing layer thickness that result from confinement effects in PbI_2 [42]. As opposed to MoS_2, where the luminescence yield increases as

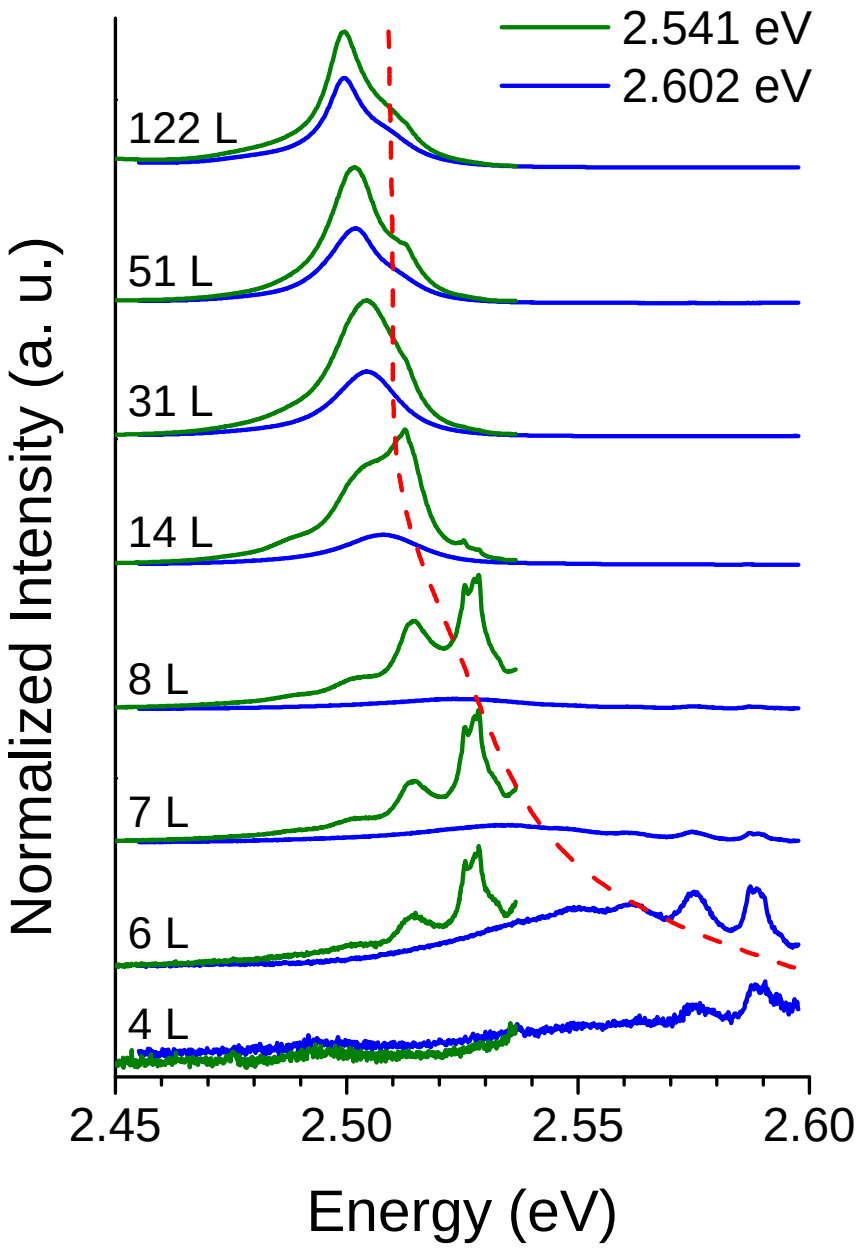

Figure 6.5: Representative PL spectra for two different laser excitations of PbI_2 samples with a range of thicknesses. Each sample was measured with both sources at 5 K, and thicknesses are indicated next to the corresponding curves. The red dashed curve serves as a guide to the eye indicating the exciton emission peaks for each thickness.

the thickness approaches a monolayer [43], the luminescence in PbI_2 is expected to quench as the band gap becomes indirect in the monolayer limit. In addition, an increasing direct band gap and changes to binding energies alter the absorption profile. It is complicated to quantify the combination of these effects in the PL of few-layer crystals where in addition, the emission volume is changing. However, in Fig. 6.5, we present emission spectra for a range of representative samples from bulk down to few-layer samples and qualitatively describe their evolution. Laser excitations of 2.541 and 2.602 eV were used for these measurements and the two spectra for each sample are shown alongside each other and normalized together to their overall maximum. In the thickest spectra, 122 and 51 L, we find a strong luminescence peak at $\sim$ 2.5 eV with a shoulder on the high energy side. This is consistent with previous measurements in bulk, where the dominant peak is attributed to luminescence from excitons bound to donors with the weak shoulder due to radiative recombination of the $n = 1$ free exciton [51]. As the layer number decreases, the emission profile begins to change, and the intensity of the bound exciton emission decreases relative to that of the free exciton to the point that only one broadened peak is observed. We attribute this to diminished reabsorption of free exciton emission as sample thicknesses approach the skin depth, which at the exciton frequency is estimated to be $\sim$ 30 layers based on absorption measurements in bulk PbI_2 at 4.5 K [13].

Furthermore at 14 layers, sharp features begin to appear in the spectra obtained with the lower excitation energy, which correspond to resonantly enhanced scattering peaks. Due to the proximity of the 2.541 eV laser with the exciton energy, the sharp phonon peaks appear clearly in its spectra down to 6 layers. The phonon scattering is made all the more apparent by comparing these spectra with the adjacent ones displaying the bare exciton luminescence from the off resonance higher energy source. As expected in the thinner samples, the exciton shifts towards higher energy approaching and even passing the 2.602 eV line below $\sim$ 4 layers. In the process, the resonant peaks begin to appear in the spectra with 2.602 eV excitation, eventually becoming more prominent than in the 2.541 eV spectra.

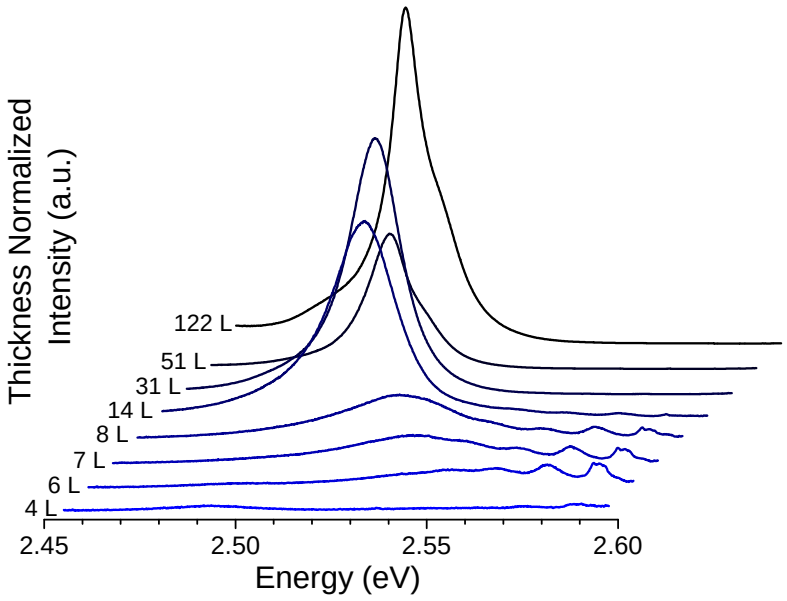

Figure 6.6: PL intensity as a function of emission energy normalized to sample thickness. Spectra were measured at 5 K using a 2.602 eV (476.5 nm) laser source. Thicknesses are denoted next to the corresponding curve.

Finally in the thinnest, 4 L, sample, the exciton energy appears to shift above 2.602 eV, and only two weak phonon peaks are visible. In addition to the resonant peaks, the PL peak appears to broaden significantly with decreasing thickness. This may be due to a number of effects including the interaction with the substrate, to which the thinnest samples would be most sensitive, nevertheless the resonant incoming and outgoing scattering appears to contribute to this effect. This is consistent with observations in CdS indicating strong exciton broadening near resonance from electron-phonon interactions [70], which is clearly visible in the thickness normalized spectra in Fig. 6.6. We also remark that due to the decreased emission from the thinnest samples, we sometimes observe background luminescence from stray light in thicker nearby areas around 2.5 eV, which has been removed in the 6 L and 4 L samples.

We now consider more closely the nature of the resonant Raman scattering. To verify these peaks are not somehow a result of the exfoliation process, we present in Fig. 6.7 the Raman scattering data for an exfoliated bulk sample with a thickness of ~ 1 μm. This

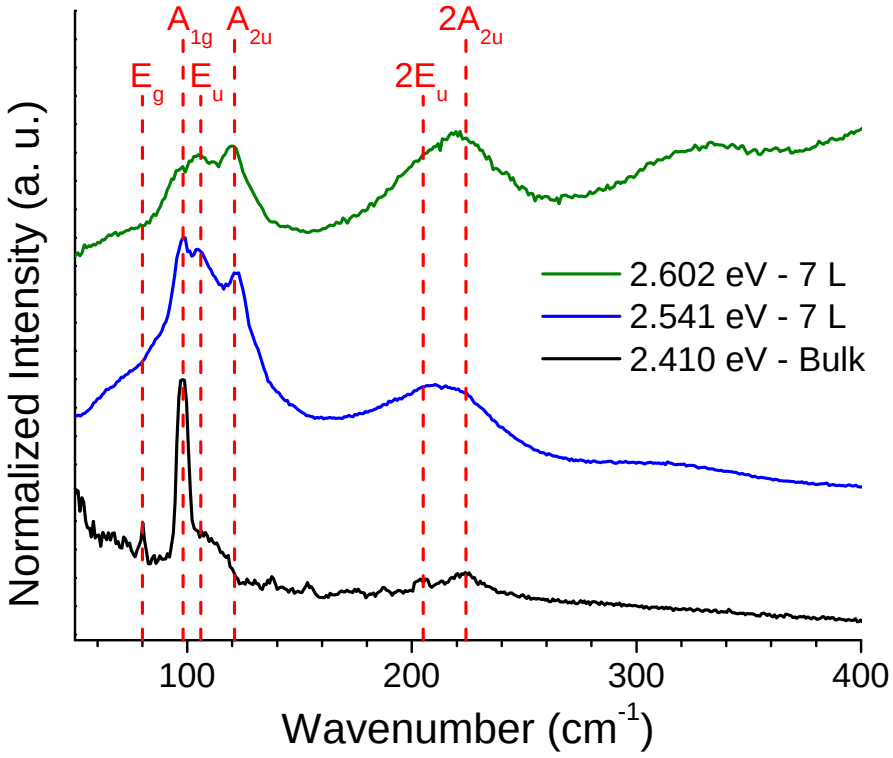

Figure 6.7: Raman scattering spectrum of a mechanically exfoliated bulk sample of PbI_2 measured at 5 K shown alongside spectra for a 7 L sample. Laser energies are indicated for each spectrum, and red dotted lines indicate phonon peaks positions.

measurement was performed using 140 μW of power well below the band edge, with a 2.41 eV laser line, to avoid the overwhelming PL signal in thicker samples. The measurement was done using the same setup as for few-layer samples, and for comparison, spectra for a 7 L sample are also shown. The peaks are labelled by their vibrational modes and their positions are generally in agreement with previous assignments [21, 87, 86]. The two most prominent peaks in the Raman spectrum are the E_g and A_{1g} modes at 80 and 98 cm^{-1} respectively. We also observe a broad hump, from $\sim$ 100 to 120 cm^{-1}, attributed to second-order scattering. In bulk, this hump masks any contribution from the Raman forbidden E_u and A_{2u} LO modes found at 106 and 121 cm^{-1} in thinner samples, which supports their resonant nature. It is interesting to note that the E_g phonon is absent in the 7 L spectra, while the A_{1g} remains visible despite the strong nearby LO peaks. Finally, we observe two weak peaks in the bulk spectrum at 205 and 224 cm^{-1}, which are attributed to resonant 2-LO phonon peaks of the E_u and A_{2u} modes respectively. In the 7 L sample, the 2-LO peaks are enhanced significantly and difficult to distinguish as they meld into one very broad peak centered around $\approx$ 215 cm^{-1}. We note that measurements nearer to resonance on bulk samples, at room temperature using a 2.331 eV laser, were consistent with the 7 L spectrum, also displaying a single broad 2-LO peak at $\approx$ 214 cm^{-1}.

Finally, we present spectra as a function of wavevector obtained at 5 and 120 K using both 2.541 and 2.602 eV laser excitations in Fig. 6.8. Again it is clear that as the luminescence shifts to higher energy there is an enhancement of the resonant phonon peaks. In this presentation it is also apparent that multiples of the LO phonons are visible up to the fourth order in the few-layer spectra. However due to their broad linewidths, it is not possible to clearly distinguish between overlapping higher order E_u and A_{2u} multiples. Thus it is not possible to assign positions to the peaks, but they are spread over energies corresponding to multiples of the first order LO modes. Measurements at 120 K show similar features with weaker background luminescence albeit also with weaker phonon enhancement, particularly in the 2.602 eV spectra. This is consistent with an intermediate excitonic state, which

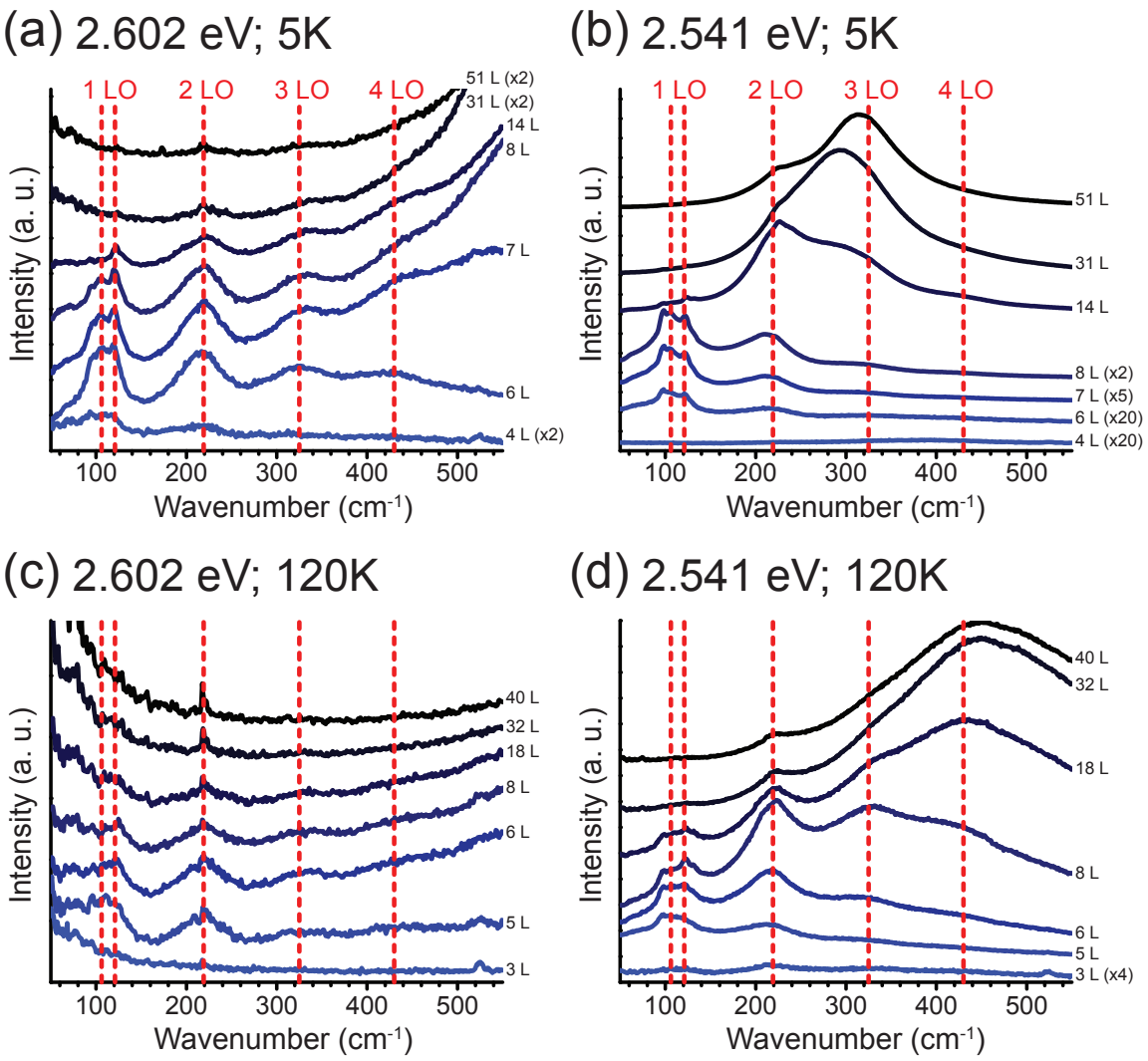

Figure 6.8: Raman spectra at 5 and 120 K using both 2.602 and 2.541 eV excitation energies. Two different sets of samples were measured at the two temperatures, and sample thicknesses are indicated alongside the corresponding curves. As noted, some curves have been multiplied by a factor for visualization purposes. The red dotted lines correspond to LO phonon overtone positions as inidicated.

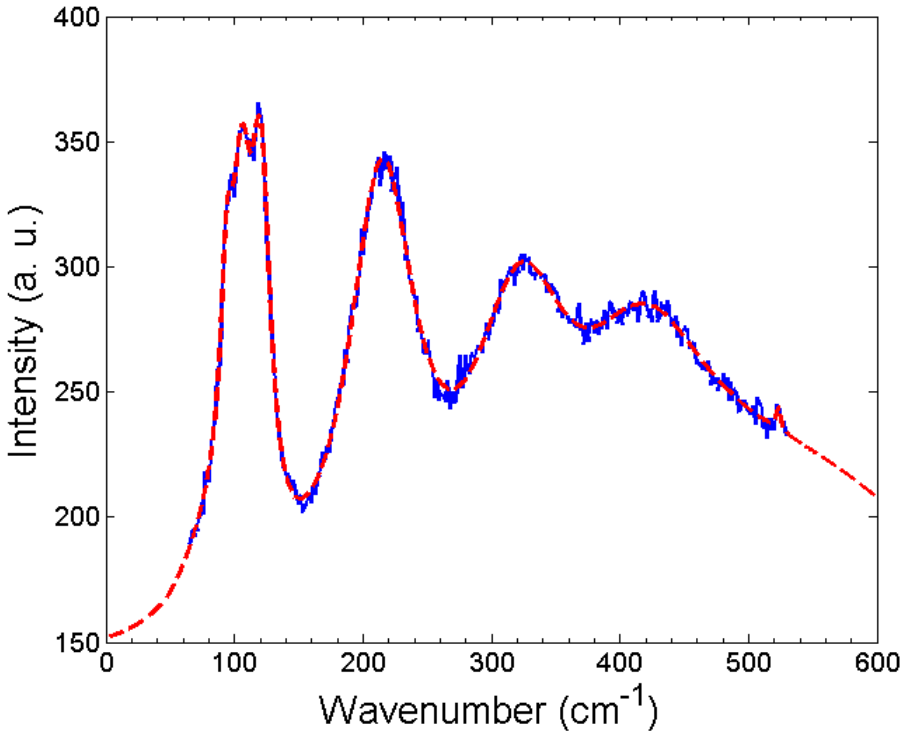

Figure 6.9: Spectrum of a 6 L sample (blue solid line) reproduced from Fig. 6.8 measured at 5 K with a 2.602 eV source. The red dashed line is a fit to the data using seven Lorentzians for the individual peaks, including the Si peak at ≈ 520 cm^{-1}, and a Gaussian for the PL background.

is expected to broaden at higher temperatures.

Based on our measurements, it is possible to estimate the Raman scattering efficiency of the observed modes near resonance. To accomplish this, individual phonon peaks were fitted with Lorentzian functions and their integrated intensities I were compared with the peak appearing at ≈ 520 cm^{-1} from the silicon substrate. The silicon scattering is weak but clearly visible in the 2.602 eV spectra of the thinnest samples in Fig. 6.8. For the purpose of demonstration, we present an estimate of the scattering efficiency near resonance for phonons at ω_s in 6 L PbI_2 at 5 K using silicon scattering at $\omega_{s'}$ as a reference. The fit to the 6 L data is shown in Fig. 6.9 where a Gaussian distribution was used to fit the PL background. The scattering efficiency S is then calculated in a backscattering geometry with corrections incorporated according to Ref. [89] for absorption and reflection in the

Table 6.1: Raman scattering efficiencies S and polarizabilities d for the phonon modes observed near resonance in a 6 L sample measured at 5 K with a 2.602 eV laser excitation.

MODE	FREQUENCY (cm^{-1})	S (cm^{-1} sr^{-1})	$\|d\|$ (cm^2)
A_{1g}	98	4.3×10^{-2}	2.4×10^{-13}
E_u	106	9.2×10^{-2}	3.6×10^{-13}
A_{2u}	121	1.1×10^{-1}	4.2×10^{-13}
2 LO	219	4.5×10^{-1}	1.1×10^{-12}
3 LO	325	4.3×10^{-1}	1.4×10^{-12}
4 LO	430	4.9×10^{-1}	1.7×10^{-12}

superposed PbI_2, SiO_2 and Si layers of our samples. The resulting expression is given by:

$$S = S_{Si}\frac{I}{I_{Si}}F_R\frac{n_{Si}(\omega_{s'})}{n(\omega_s)}\frac{(1-R_1^s)e^{-\alpha_s L}(1-R_2^s)\frac{(1-R_3^s)(1-R_3^i)}{\alpha_i^{Si}+\alpha_{s'}^{Si}}(1-R_2^i)e^{-\alpha_i L}(1-R_1^i)}{(1-R_1^s)(1-R_1^i)\frac{(1-e^{-(\alpha_i+\alpha_s)L})}{\alpha_i+\alpha_s}} \tag{6.2}$$

where $n(\omega_s)$ is the index of refraction and F_R is a function of the spectrometer response = .64 in our case. The reflectance R_j^i (R_j^s) of the incident (scattered) light at the jth interface (1 = Vacuum-PbI_2; 2 = PbI_2-SiO_2; 3 = SiO_2-Si) and the absorption coefficient α_i (α_s) at the incident (scattered) light frequency were determined for PbI_2 (using $n \approx 3.6$ [29], $\alpha_i \approx 1.2\times10^5 cm^{-1}$ and $\alpha_s \approx 1.2\times10^6 cm^{-1}$ [13]) and for Si and SiO_2 from corresponding optical parameters [64, 65]. Due to the difficulty in determining the exact frequency dependence of absorption around the exciton energy in PbI_2, the maximum α_s was assumed for all the scattered frequencies. The silicon Raman scattering efficiency S_{Si} and polarizability are given in Refs. [90, 91], and for simplicity we use the values quoted for a laser energy of 2.54 eV. Our results are presented in Table 6.1, and the estimates are comparable to the largest values found in Ref. [67] for Mg_2Si and Mg_2Ge.

6.5 Conclusions

We have demonstrated resonantly enhanced multi-phonon scattering in few-layer samples of PbI_2, observing up the fourth overtone, with extremely large Raman scattering efficiencies. This effect can be used as a precise technique to characterize few-layer crystals of PbI_2 and should prove useful for other polar van der Waals crystals, such as GaSe. We have shown that by changing layer thickness, it is possible to change exciton energies and in turn use fixed excitation sources to detect these changes even for weakly emitting samples. With the use of tunable lasers, it should in principle be possible to map the exciton absorption spectrum for the various layer thicknesses. Finally, we observe no significant changes to phonon energies or widths down to approximately 4 layers. However, with added tunability, we expect to be able to probe additional changes due to confinement in mono- and bilayer samples.

6.6 Supplementary Information

6.6.1 Room Temperature Micro-Raman

We briefly present the results of micro-Raman measurements performed in Professor Matzger's lab using a Renishaw inVia Raman microscope. Results are presented in Fig. reffig:microraman for exfoliated PbI_2 samples with a range of thicknesses. Due to the notch filter used, there is no visible signal below ≈ 150 cm^{-1}. However we observe second order scattering from both the PbI_2 and Si. The 165 and 214 cm^{-1} peaks are attributed to $2E_g$ and 2 LO scattering in PbI_2 [87] and are likely visible because the 2.331 eV excitation is relatively close to the bulk gap at room temperature. However, no higher order LO peaks are visible, and the scattering is significantly weaker than the Si scattering. As the samples get thinner those peaks disappear as the band gap is expected to move to higher energy. The thinnest 4 L sample shows only the second order Si scattering along with the strong 520 cm^{-1} peak. It

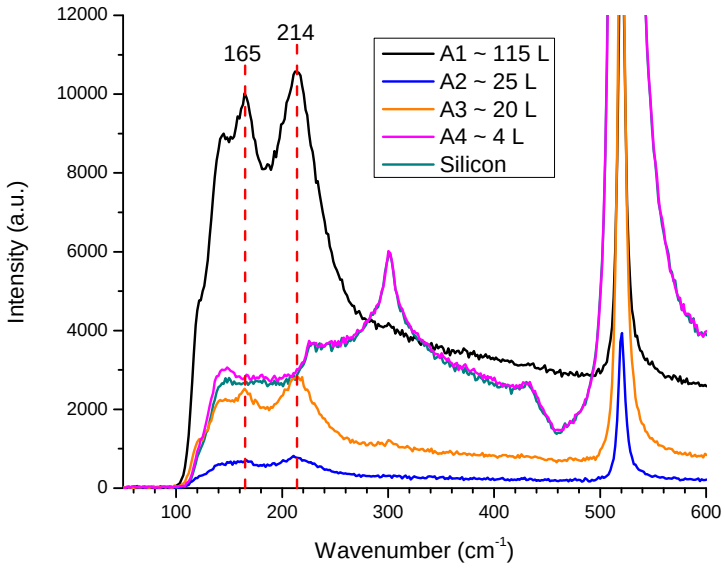

Figure 6.10: Room temperature Raman measurements on PbI_2 and the Si/SiO_2 substrate using a Renishaw inVia Raman microscope with a 100x objective and $\approx$ 1.5 mW of power from a 532 nm laser.

is also interesting to note that samples only began to visibly burn for $\gtrsim$ 10 mW of power as seen in area A1 of Fig. 3.10.

CHAPTER 7

Conclusions

PbI_2 is a interesting semiconductor with exceptionally strong absorption at its band edge, which may prove useful in the large and growing field of research on two dimensional van der Waals crystals. This thesis has investigated the properties of few-layer PbI_2 crystals both optically and theoretically. Results have been presented showing that the lowest exciton state is extremely tightly bound and Frenkel-like despite belonging to a Wannier series. In addition, first-principles bandstructure and exciton calculations for bulk as well as 1, 2, and 3 layers have been performed for the first time, shedding new light on the properties of PbI_2. This understanding will be critical for future work involving few-layer PbI_2. Finally, multiphonon resonant Raman scattering has been demonstrated for the first time in atomically thin exfoliated crystals. This technique provides a new tool to effectively probe and characterize few-layer crystals, and this strong effect is expected to be found in many other polar few-layer compounds near resonance.

While this work has provided significant insight on PbI_2 at the few-layer scale, much future work remains. The most apparent shortcoming in this work has been the inability to probe mono- and bilayer samples experimentally through PL because of the laser energies required. Reflection experiments with higher resolution and better signal should readily indicate the exciton energy in these thinnest samples, which would allow for direct comparison with the calculated energies as well as the predicted nature of the band gap. It would also be interesting to go to lower temperatures to try and observe higher exciton

states as well as potential LO sidebands in reflection. The temperature dependence itself is something that should be studied more closely in few-layer samples as increases in the binding energy may lead to exciton PL at higher temperatures in the thinnest samples. Finally, using a tunable laser, it would be interesting to see if multiphonon resonant Raman scattering can be observed at room temperature, which would make the technique more useful and accessible.

Although this work has focused on PbI_2, there is an entire class of other similar layered van der Waals semiconductors to be studied. The understanding and techniques developed in this work and that of others on graphene and the transition metal dichalcogenides should translate directly to the study of few-layer crystals of other materials. In particular, GaSe is a similar material that is readily obtained and whose band gap, ≈ 2.1 eV, is easily accessed using a Rhodamyne dye laser. Preliminary measurements have already shown that higher order LO scattering may be probed in exfoliated crystals of GaSe.

Like many new materials, the greatest limitation for the field of two dimensional van der Waals materials is the ability to produce large area crystals at scale rapidly and cheaply. While mechanical exfoliation is extremely useful in obtaining satisfactory samples for experiments, new techniques must be developed for applications to be feasible. This remains the greatest challenge for this field and will likely dictate the level of interest in the future. As such, this must be included as one of the most important areas for future work.

APPENDIX A

Computational Files

In this section, example input files are presented for the primary computer packages utilized for computations. Input files are limited to those for the bulk and the monolayer structures of PbI_2, but the required changes for additional layer structures should be relatively straightforward from the examples. Detailed explanations of the various flags and their settings can be found in each respective package's documentation.

A.1 Quantum Espresso

A.1.1 scf.in

Bulk:

```
&control
   calculation     = 'scf'
   restart_mode    = 'from_scratch',
   prefix          = 'pbi2',
   tstress         = .true.
   tprnfor         = .true.
   pseudo_dir      = '.',
   outdir          = '.'
   wf_collect      = .true.
   verbosity       = 'high'
/
```

```
 &system
    ibrav           =  4,
    celldm(1)       =  8.6077018780d0
    celldm(3)     =  1.5317233809
    nat             =  3,
    ntyp            =  2,
    ecutwfc         =  50.0,
    nbnd            =  30
    occupations     = 'fixed'
 /
 &electrons
    diagonalization = 'cg'
    mixing_mode     = 'plain'
    mixing_beta     =  0.7
    conv_thr        =  1.0d-8
    diago_full_acc  = .true.
 /
ATOMIC_SPECIES
 Pb  207.20000  Pb.cpi.UPF
 I   126.90447  I.cpi.UPF
ATOMIC_POSITIONS crystal
Pb 0.0000000000  0.0000000000  0.0000000000
I  0.3333333333  0.6666666667  0.2650000000
I  0.6666666667  0.3333333333 -0.2650000000
K_POINTS automatic
6 6 4 1 1 1
```

1 Layer:

```
 &control
    calculation     = 'scf'
    restart_mode    = 'from_scratch',
    prefix          = 'pbi2',
    tstress         = .true.
```

```
    tprnfor         = .true.
    pseudo_dir      = '.',
    outdir          = '.'
    wf_collect      = .true.
    verbosity       = 'high'
 /
 &system
    ibrav           =  4,
    celldm(1)       =  8.6077018780d0
    celldm(3)       =  2.6344676180
    nat             =  3,
    ntyp            =  2,
    ecutwfc         =  50.0,
    nbnd            =  30
    occupations     = 'fixed'
 /
 &electrons
    diagonalization = 'cg'
    mixing_mode     = 'plain'
    mixing_beta     =  0.7
    conv_thr        =  1.0d-8
    diago_full_acc  = .true.
 /
ATOMIC_SPECIES
 Pb  207.20000  Pb.cpi.UPF
 I   126.90447  I.cpi.UPF
ATOMIC_POSITIONS crystal
Pb 0.0000000000  0.0000000000  0.0000000000
I  0.3333333333  0.6666666667  0.1511981826
I  0.6666666667  0.3333333333 -0.1511981826
K_POINTS automatic
8 8 1 1 1 0
```

A.2 BerkeleyGW

A.2.1 kernel.inp

Bulk:

```
number_val_bands 6
number_cond_bands 3
screened_coulomb_cutoff 20.0
bare_coulomb_cutoff 50.0
use_symmetries_coarse_grid
screening_semiconductor
```

1 Layer:

```
number_val_bands 6
number_cond_bands 3
screened_coulomb_cutoff 20.0
bare_coulomb_cutoff 50.0
use_symmetries_coarse_grid
screening_semiconductor
cell_slab_truncation
```

A.2.2 sigma.inp

Bulk:

```
frequency_dependence 1
exact_static_ch 1
degeneracy_check_override
screened_coulomb_cutoff 20.0
bare_coulomb_cutoff 50.0
number_bands 400
band_occupation 14*1 386*0
band_index_min 1
band_index_max 59
```

```
screening_semiconductor
number_kpoints 1
begin kpoints
  0.000000000  0.000000000  0.500000000  1.0
end
```

1 Layer:

```
requency_dependence 1
exact_static_ch 1
degeneracy_check_override
screened_coulomb_cutoff 20.0
bare_coulomb_cutoff 50.0
number_bands 400
band_occupation 14*1 386*0
band_index_min 1
band_index_max 28
screening_semiconductor
cell_slab_truncation
number_kpoints 1
begin kpoints
  0.000000000  0.000000000  0.000000000  1.0
end
```

A.3 Wannier90

Bulk:

```
num_bands         =   59
num_wann          =   27

dis_win_min       =  -13.0d0
dis_win_max       =   32.0d0
dis_froz_min      =  -13.0d0
```

```
dis_froz_max      =   14.0d0

#search_shells = 20

#hr_plot = .true.
#wannier_plot = .true.
#wannier_plot_format = cube

#restart = wannierise

num_iter          = 2000
num_print_cycles  = 10

dis_num_iter = 10000
dis_mix_ratio = 0.99

Begin Atoms_Frac
Pb     0.0000000000        0.0000000000        0.0000000000
I      0.3333333333        0.6666666667        0.2650000000
I      0.6666666667        0.3333333333       -0.2650000000
End Atoms_Frac

Begin Projections
Pb:sp3;d
I:sp3;d
End Projections

bands_plot .true.
begin kpoint_path
G 0.000000 0.000000 0.000000 K 0.333333 0.333333 0.000000
K 0.333333 0.333333 0.000000 H 0.333333 0.333333 0.500000
H 0.333333 0.333333 0.500000 A 0.000000 0.000000 0.500000
A 0.000000 0.000000 0.500000 G 0.000000 0.000000 0.000000
```

```
G 0.000000 0.000000 0.000000 M 0.500000 0.000000 0.000000
M 0.500000 0.000000 0.000000 L 0.500000 0.000000 0.500000
L 0.500000 0.000000 0.500000 A 0.000000 0.000000 0.500000
end kpoint_path
bands_num_points 200
bands_plot_format gnuplot xmgrace

Begin Unit_Cell_Cart
Bohr
 8.607701878000000E+000  0.000000000000000E+000  0.000000000000000E+000
-4.303850939000000E+000  7.454488494551549E+000  0.000000000000000E+000
 0.000000000000000E+000  0.000000000000000E+000  1.318461822234944E+001
End Unit_Cell_Cart

mp_grid      = 6 6 4
begin kpoints
...
End Kpoints
```

1 Layer:

```
num_bands         =   59
num_wann          =   17

dis_win_min       =  -17.0d0
dis_win_max       =   22.0d0
dis_froz_min      =  -17.0d0
dis_froz_max      =   4.4d0

#search_shells = 20

#hr_plot = .true.
#wannier_plot = .true.
#wannier_plot_format = cube
```

```
#restart = plot

num_iter          = 2000
num_print_cycles  = 10

dis_num_iter = 10000
dis_mix_ratio = 0.99

Begin Atoms_Frac
Pb     0.0000000000        0.0000000000        0.0000000000
I      0.3333333333        0.6666666667        0.1511981826
I      0.6666666667        0.3333333333       -0.1511981826
End Atoms_Frac

Begin Projections
Pb:sp3;d
I:sp3
End Projections

bands_plot .true.
begin kpoint_path
K 0.333333 0.333333 0.000000 G 0.000000 0.000000 0.000000
G 0.000000 0.000000 0.000000 M 0.500000 0.000000 0.000000
end kpoint_path
bands_num_points 200
bands_plot_format gnuplot xmgrace

Begin Unit_Cell_Cart
Bohr
 8.607701878000000E+000  0.000000000000000E+000  0.000000000000000E+000
-4.303850939000000E+000  7.454488494551549E+000  0.000000000000000E+000
 0.000000000000000E+000  0.000000000000000E+000  2.267671186298879E+001
```

```
End Unit_Cell_Cart

mp_grid      = 8 8 1

begin kpoints
...
End Kpoints
```

A.4 Spin Orbit

Bulk:

```
GW_eig .TRUE.

# coordinates of the atoms, mandatory
begin coordinates
newtype Pb
coord     0.0000000000  0.0000000000  0.0000000000
newtype I
coord     0.3333333333  0.6666666667  0.2650000000
coord     0.6666666667  0.3333333333 -0.2650000000
end coordinates

# lattice vectors in cartesian coordinates in Bohr (copy from data-file.xml)
begin latticevecs
coord  8.607701878000000E+000  0.000000000000000E+000  0.000000000000000E+000
coord -4.303850939000000E+000  7.454488494551549E+000  0.000000000000000E+000
coord  0.000000000000000E+000  0.000000000000000E+000  1.318461822234944E+001
volume  846.0044
end latticevecs

band_range 1 59
```

```
energy_cutoff 40

k_grid 400

begin kpoints
0.000000000000 0.000000000000 0.500000000000
end kpoints
```

1 Layer:

```
GW_eig .TRUE.

# coordinates of the atoms, mandatory
begin coordinates
newtype Pb
coord     0.0000000000  0.0000000000  0.0000000000
newtype I
coord     0.3333333333  0.6666666667  0.1511981826
coord     0.6666666667  0.3333333333 -0.1511981826
end coordinates

# lattice vectors in cartesian coordinates in Bohr (copy from data-file.xml)
begin latticevecs
coord  8.607701878000000E+000  0.000000000000000E+000  0.000000000000000E+000
coord -4.303850939000000E+000  7.454488494551549E+000  0.000000000000000E+000
coord  0.000000000000000E+000  0.000000000000000E+000  2.267671186298879E+001
volume  1455.0742
end latticevecs

band_range 1 59

energy_cutoff 40

k_grid 400
```

```
begin kpoints
0.000000000000 0.000000000000 0.000000000000
end kpoints
```

BIBLIOGRAPHY

[1] Novoselov, K. S., Jiang, D., Schedin, F., Booth, T. J., Khotkevich, V. V., Morozov, S. V., and Geim, A. K., "Two-dimensional atomic crystals." *Proceedings of the National Academy of Sciences of the United States of America*, Vol. 102, No. 30, July 2005, pp. 10451–3.

[2] Geim, A. K. and Novoselov, K. S., "The rise of graphene." *Nature materials*, Vol. 6, No. 3, March 2007, pp. 183–91.

[3] Kittel, C., *Introduction to Solid State Physics*, John Wiley & Sons, 8th ed., 2005.

[4] Israelachvili, J. N., *Intermolecular and Surface Forces*, Elsevier, 2011.

[5] Tubbs, M., "The Optical Properties and Chemical Decomposition of Lead Iodide," *Proceedings of the Royal Society of London*, Vol. 280, No. 1383, 1964, pp. 566.

[6] Schlüter, I. and Schlüter, M., "Electronic structure and optical properties of PbI_{2}," *Physical Review B*, Vol. 9, No. 4, Feb. 1974, pp. 1652–1663.

[7] Lucovsky, G., White, R., Liang, W., Zallen, R., and Schmid, P., "The lattice polarizability of PbI2," *Solid State Communications*, Vol. 18, No. 7, Jan. 1976, pp. 811–814.

[8] Wyckoff, R. W. G., *Crystal Structures, Volume 1*, Interscience Publishers, New York, 2nd ed., 1963.

[9] Beckmann, P. A., "A review of polytypism in lead iodide," *Crystal Research and Technology*, Vol. 45, No. 5, May 2010, pp. 455–460.

[10] Yu, P. and Cardona, M., *Fundamentals of Semiconductors*, Springer-Verlag, Berlin Heidelberg New York, 3rd ed., 2001.

[11] Knox, R. S., *Theory of Excitons*, Academic Press, New York, 1963.

[12] Toyozawa, Y., *Optical Properties in Solids*, Cambridge University Press, Cambridge, 2003.

[13] Gähwiller, C. and Harbeke, G., "Excitonic Effects in the Electroreflectance of Lead Iodide," *Physical Review*, Vol. 185, No. 3, Sept. 1969, pp. 1141–1149.

[14] Nikitine, S. and Perny, G., "Etude du spectre de raies d'absorption de PbI2 aux tres basses temperatures," *Compte Rendu: Academie des Sciences (Paris)*, Vol. 240, 1955, pp. 64.

[15] Thanh, L. C., Depeursinge, C., Levy, F., and Mooser, E., "The band gap excitons in PbI2," *Journal of Physics and Chemistry of Solids*, Vol. 36, No. 7-8, July 1975, pp. 699–702.

[16] Harbeke, G. and Tosatti, E., "Band-Edge Excitons in PbI_{2}: A Puzzle?" *Physical Review Letters*, Vol. 28, No. 24, June 1972, pp. 1567–1570.

[17] Fortin, E. and Raga, F., "Excitons in molybdenum disulphide," *Physical Review B*, Vol. 11, No. 2, Jan. 1975, pp. 905–912.

[18] Dingle, R., Wiegmann, W., and Henry, C., "Quantum States of Confined Carriers in Very Thin Al_{x}Ga_{1-x}As-GaAs-Al_{x}Ga_{1-x}As Heterostructures," *Physical Review Letters*, Vol. 33, No. 14, Sept. 1974, pp. 827–830.

[19] Davies, J. H., *The Physics of Low-Dimensional Semiconductors: An Introduction*, Cambridge University Press, Cambridge, 1998.

[20] Dingle, R., "Confined Carrier Quantum States in Ultrathin Semiconductor Heterostructures," *Festkörperprobleme 15: Advances in Solid State Physics*, edited by H. Queisser, Springer Berlin Heidelberg, 1975, pp. 21–48.

[21] Grisel, A. and Schmid, P., "Polytypism and Lattice Vibrations of PbI2," *physica status solidi (b)*, Vol. 73, No. 2, Feb. 1976, pp. 587–591.

[22] Hayes, W. and Loudon, R., *Scattering of Light by Crystals*, John Wiley & Sons, New York, 1978.

[23] Loudon, R., "The Raman effect in crystals," *Advances in Physics*, Vol. 50, No. 7, Nov. 2001, pp. 813–864.

[24] Martin, R. M. and Falicov, L. M., "Resonant Raman Scattering," *Light Scattering in Solids I*, Vol. 8 of *Topics in Applied Physics*, chap. 3, Springer Berlin Heidelberg, Berlin, Heidelberg, 1983, pp. 79–145.

[25] Matuchova, M., Zdansky, K., Zavadil, J., Danilewsky, A., Maixner, J., and Alexiev, D., "Electrical, optical and structural properties of lead iodide," *Journal of Materials Science: Materials in Electronics*, Vol. 20, No. 3, Dec. 2008, pp. 289–294.

[26] Novoselov, K. S., Geim, A. K., Morozov, S. V., Jiang, D., Zhang, Y., Dubonos, S. V., Grigorieva, I. V., and Firsov, A. A., "Electric field effect in atomically thin carbon films." *Science*, Vol. 306, No. 5696, Oct. 2004, pp. 666–9.

[27] Blake, P., Hill, E. W., Castro Neto, A. H., Novoselov, K. S., Jiang, D., Yang, R., Booth, T. J., and Geim, A. K., "Making graphene visible," *Applied Physics Letters*, Vol. 91, No. 6, Aug. 2007, pp. 063124.

[28] Gorbachev, R. V., Riaz, I., Nair, R. R., Jalil, R., Britnell, L., Belle, B. D., Hill, E. W., Novoselov, K. S., Watanabe, K., Taniguchi, T., Geim, A. K., and Blake, P., "Hunting for monolayer boron nitride: optical and Raman signatures." *Small (Weinheim an der Bergstrasse, Germany)*, Vol. 7, No. 4, Feb. 2011, pp. 465–8.

[29] Dugan, A. and Henisch, H., "Dielectric properties and index of refraction of lead iodide single crystals," *Journal of Physics and Chemistry of Solids*, Vol. 28, No. 6, June 1967, pp. 971–976.

[30] Bruker Corporation, "Introduction to Brukers ScanAsyst and PeakForce Tapping AFM Technology," 2011.

[31] Nemes-Incze, P., Osváth, Z., Kamarás, K., and Biró, L., "Anomalies in thickness measurements of graphene and few layer graphite crystals by tapping mode atomic force microscopy," *Carbon*, Vol. 46, No. 11, 2008, pp. 1435–1442.

[32] Wood, J. D., Wells, S. A., Jariwala, D., Chen, K.-S., Cho, E., Sangwan, V. K., Liu, X., Lauhon, L. J., Marks, T. J., and Hersam, M. C., "Effective passivation of exfoliated black phosphorus transistors against ambient degradation." *Nano letters*, Vol. 14, No. 12, Dec. 2014, pp. 6964–70.

[33] Martin, R. M., *Electronic structure : Basic Theory and Practical Methods*, Cambridge University Press, Cambridge, 2004.

[34] Fuchs, M. and Scheffler, M., "Ab initio pseudopotentials for electronic structure calculations of poly-atomic systems using density-functional theory," *Computer Physics Communications*, Vol. 119, No. 1, June 1999, pp. 67–98.

[35] Payne, M. C., Arias, T. A., and Joannopoulos, J. D., "Iterative minimization techniques for ab initio total-energy calculations: molecular dynamics and conjugate gradients," *Reviews of Modern Physics*, Vol. 64, No. 4, Oct. 1992, pp. 1045–1097.

[36] Deslippe, J., Samsonidze, G., Strubbe, D. A., Jain, M., Cohen, M. L., and Louie, S. G., "BerkeleyGW: A massively parallel computer package for the calculation of the quasiparticle and optical properties of materials and nanostructures," *Computer Physics Communications*, Vol. 183, No. 6, June 2012, pp. 1269–1289.

[37] Ismail-Beigi, S., "Truncation of periodic image interactions for confined systems," *Physical Review B*, Vol. 73, No. 23, June 2006, pp. 233103.

[38] Hybertsen, M. and Louie, S., "Spin-orbit splitting in semiconductors and insulators from the ab initio pseudopotential," *Physical Review B*, Vol. 34, No. 4, Aug. 1986, pp. 2920–2922.

[39] Mostofi, A. A., Yates, J. R., Lee, Y.-S., Souza, I., Vanderbilt, D., and Marzari, N., "wannier90: A tool for obtaining maximally-localised Wannier functions," *Computer Physics Communications*, Vol. 178, No. 9, May 2008, pp. 685–699.

[40] Marzari, N., Mostofi, A. A., Yates, J. R., Souza, I., and Vanderbilt, D., "Maximally localized Wannier functions: Theory and applications," *Reviews of Modern Physics*, Vol. 84, No. 4, Oct. 2012, pp. 1419–1475.

[41] Onida, G., Reining, L., and Rubio, A., "Electronic excitations: density-functional versus many-body Greens-function approaches," *Reviews of Modern Physics*, Vol. 74, No. 2, June 2002, pp. 601–659.

[42] Toulouse, A. S., Isaacoff, B. P., Shi, G., Matuchová, M., Kioupakis, E., and Merlin, R., "Frenkel-like Wannier-Mott excitons in few-layer Pb I 2," *Physical Review B*, Vol. 91, No. 16, April 2015, pp. 165308.

[43] Mak, K. F., Lee, C., Hone, J., Shan, J., and Heinz, T. F., "Atomically Thin MoS_{2}: A New Direct-Gap Semiconductor," *Physical Review Letters*, Vol. 105, No. 13, Sept. 2010, pp. 136805.

[44] Komsa, H.-P. and Krasheninnikov, A. V., "Effects of confinement and environment on the electronic structure and exciton binding energy of MoS_{2} from first principles," *Physical Review B*, Vol. 86, No. 24, Dec. 2012, pp. 241201.

[45] Zhao, Y., Luo, X., Li, H., Zhang, J., Araujo, P. T., Gan, C. K., Wu, J., Zhang, H., Quek, S. Y., Dresselhaus, M. S., and Xiong, Q., "Interlayer breathing and shear modes in few-trilayer MoS2 and WSe2." *Nano letters*, Vol. 13, No. 3, March 2013, pp. 1007–15.

[46] Chernikov, A., Berkelbach, T. C., Hill, H. M., Rigosi, A., Li, Y., Aslan, O. B., Reichman, D. R., Hybertsen, M. S., and Heinz, T. F., "Exciton Binding Energy and Nonhydrogenic Rydberg Series in Monolayer WS2," *Physical Review Letters*, Vol. 113, No. 7, Aug. 2014, pp. 076802.

[47] Hu, P., Wen, Z., Wang, L., Tan, P., and Xiao, K., "Synthesis of few-layer GaSe nanosheets for high performance photodetectors." *ACS nano*, Vol. 6, No. 7, July 2012, pp. 5988–94.

[48] Tongay, S., Sahin, H., Ko, C., Luce, A., Fan, W., Liu, K., Zhou, J., Huang, Y.-S., Ho, C.-H., Yan, J., Ogletree, D. F., Aloni, S., Ji, J., Li, S., Li, J., Peeters, F. M., and Wu, J., "Monolayer behaviour in bulk ReS2 due to electronic and vibrational decoupling." *Nature communications*, Vol. 5, Feb. 2014, pp. 3252.

[49] Tubbs, M. and Forty, A., "The exciton spectrum of lead iodide," *Journal of Physics and Chemistry of Solids*, Vol. 26, No. 4, April 1965, pp. 711–719.

[50] Matuchova, M., Prochazkova, O., Maixner, J., Zdansky, K., and Zavadil, J., "Influence of rare earth holmium on the properties of lead iodide," *physica status solidi (c)*, Vol. 2, No. 4, March 2005, pp. 1275–1279.

[51] Lévy, F., Mercier, A., and Voitchovsky, J.-P., "Band-edge photoluminescence of PbI2," *Solid State Communications*, Vol. 15, No. 5, Sept. 1974, pp. 819–822.

[52] Merlin, R., Güntherodt, G., Humphreys, R., Cardona, M., Suryanarayanan, R., and Holtzberg, F., "Multiphonon processes in YbS," *Physical Review B*, Vol. 17, No. 12, June 1978, pp. 4951–4958.

[53] Perdew, J. P. and Zunger, A., "Self-interaction correction to density-functional approximations for many-electron systems," *Physical Review B*, Vol. 23, No. 10, May 1981, pp. 5048–5079.

[54] Giannozzi, P., Baroni, S., Bonini, N., Calandra, M., Car, R., Cavazzoni, C., Ceresoli, D., Chiarotti, G. L., Cococcioni, M., Dabo, I., Dal Corso, A., de Gironcoli, S., Fabris, S., Fratesi, G., Gebauer, R., Gerstmann, U., Gougoussis, C., Kokalj, A., Lazzeri, M., Martin-Samos, L., Marzari, N., Mauri, F., Mazzarello, R., Paolini, S., Pasquarello, A., Paulatto, L., Sbraccia, C., Scandolo, S., Sclauzero, G., Seitsonen, A. P., Smogunov, A., Umari, P., and Wentzcovitch, R. M., "QUANTUM ESPRESSO: a modular and open-source software project for quantum simulations of materials." *Journal of physics. Condensed matter : an Institute of Physics journal*, Vol. 21, No. 39, Sept. 2009, pp. 395502.

[55] Hybertsen, M. and Louie, S., "Electron correlation in semiconductors and insulators: Band gaps and quasiparticle energies," *Physical Review B*, Vol. 34, No. 8, Oct. 1986, pp. 5390–5413.

[56] Kioupakis, E., Tiago, M. L., and Louie, S. G., "Quasiparticle electronic structure of bismuth telluride in the G W approximation," *Physical Review B*, Vol. 82, No. 24, Dec. 2010, pp. 245203.

[57] Rohlfing, M. and Louie, S., "Electron-hole excitations and optical spectra from first principles," *Physical Review B*, Vol. 62, No. 8, Aug. 2000, pp. 4927–4944.

[58] Nagamune, Y., Takeyama, S., and Miura, N., "Magnetoabsorption spectra of band-edge excitons in 2H-PbI2 at high magnetic fields up to 40 T," *Physical Review B*, Vol. 40, No. 11, Oct. 1989, pp. 8099–8102.

[59] Roth, F., Mahns, B., Büchner, B., and Knupfer, M., "Exciton character in picene molecular solids," *Physical Review B*, Vol. 83, No. 16, April 2011, pp. 165436.

[60] Zaslow, B., "Two-Dimensional Analog to the Hydrogen Atom," *American Journal of Physics*, Vol. 35, No. 12, July 1967, pp. 1118.

[61] Noffsinger, J., Kioupakis, E., Van de Walle, C. G., Louie, S. G., and Cohen, M. L., "Phonon-Assisted Optical Absorption in Silicon from First Principles," *Physical Review Letters*, Vol. 108, No. 16, April 2012, pp. 167402.

[62] Bastard, G., Mendez, E., Chang, L., and Esaki, L., "Exciton binding energy in quantum wells," *Physical Review B*, Vol. 26, No. 4, Aug. 1982, pp. 1974–1979.

[63] Efros, A. L., "Excitons in quantum-well structures," *Soviet Physics: Semiconductors*, Vol. 20, No. 7, 1986, pp. 808.

[64] Edwards, D. F., "Handbook of Optical Constants of Solids," *Handbook of Optical Constants of Solids*, edited by E. D. Palik, Elsevier, 1997, pp. 547–569.

[65] Philipp, H., "Handbook of Optical Constants of Solids," *Handbook of Optical Constants of Solids*, edited by E. D. Palik, Elsevier, 1997, pp. 749–763.

[66] Tanguy, C., "Complex dielectric constant of two-dimensional wannier excitons," *Solid State Communications*, Vol. 98, No. 1, April 1996, pp. 65–68.

[67] Cardona, M., "Resonance Phenomena," *Light Scattering in Solids II*, edited by M. Cardona and G. Güntherodt, Vol. 50 of *Topics in Applied Physics*, chap. 2, Springer Berlin Heidelberg, Berlin, Heidelberg, 1982, pp. 19–178.

[68] Martin, R. M., "Theory of the One-Phonon Resonance Raman Effect," *Physical Review B*, Vol. 4, No. 10, Nov. 1971, pp. 3676–3685.

[69] Leite, R. C. C., Scott, J. F., and Damen, T. C., "Multiple-Phonon Resonant Raman Scattering in CdS," *Physical Review Letters*, Vol. 22, No. 15, April 1969, pp. 780–782.

[70] Klein, M. V. and Porto, S. P. S., "Multiple-Phonon-Resonance Raman Effect in CdS," *Physical Review Letters*, Vol. 22, No. 15, April 1969, pp. 782–784.

[71] Scott, J., Leite, R., and Damen, T., "Resonant Raman Effect in Semiconductors," *Physical Review*, Vol. 188, No. 3, Dec. 1969, pp. 1285–1290.

[72] Scott, J. F., "uv Resonant Raman Scattering in ZnO," *Physical Review B*, Vol. 2, No. 4, Aug. 1970, pp. 1209–1211.

[73] Camassel, J., Chiang, T., Shen, Y., Voitchovsky, J.-P., and Amer, N., "Multiphonon resonant Raman scattering in GaSe," *Solid State Communications*, Vol. 19, No. 6, July 1976, pp. 483–485.

[74] Reydellet, J., Balkanski, M., and Besson, J., "Multiple-phonon resonant raman scattering processes in GaSe," *Journal de Physique Lettres*, Vol. 37, No. 9, Sept. 1976, pp. 219–222.

[75] Goto, T. and Nishina, Y., "Multiple-phonon scattering near the direct absorption edge in 2H-PbI2," *Solid State Communications*, Vol. 31, No. 5, Aug. 1979, pp. 369–372.

[76] Scott, J., Damen, T., Silfvast, W., Leite, R., and Cheesman, L., "Resonant Raman scattering in ZnS and ZnSe with the cadmium laser," *Optics Communications*, Vol. 1, No. 8, March 1970, pp. 397–399.

[77] Martin, R. M. and Varma, C. M., "Cascade Theory of Inelastic Scattering of Light," *Physical Review Letters*, Vol. 26, No. 20, May 1971, pp. 1241–1244.

[78] Zeyher, R., "Theory of multiphonon raman spectra above the energy gap in semiconductors," *Solid State Communications*, Vol. 16, No. 1, Jan. 1975, pp. 49–52.

[79] Martin, R. M. and Damen, T. C., "Breakdown of Selection Rules in Resonance Raman Scattering," *Physical Review Letters*, Vol. 26, No. 2, Jan. 1971, pp. 86–88.

[80] Kiefer, W., "Laser-excited Resonance Raman Spectra of Small Molecules and IonsA Review," *Applied Spectroscopy*, Vol. 28, No. 2, March 1974, pp. 115–134.

[81] Jain, K. and Jayanthi, C., "Quasibound excitonLO-phonon intermediate state in multiphonon Raman scattering of semiconductors," *Physical Review B*, Vol. 26, No. 6, Sept. 1982, pp. 3273–3278.

[82] Ferrari, A. C., Meyer, J. C., Scardaci, V., Casiraghi, C., Lazzeri, M., Mauri, F., Piscanec, S., Jiang, D., Novoselov, K. S., Roth, S., and Geim, A. K., "Raman Spectrum of Graphene and Graphene Layers," *Physical Review Letters*, Vol. 97, No. 18, Oct. 2006, pp. 187401.

[83] Lee, C., Yan, H., Brus, L. E., Heinz, T. F., Hone, J., and Ryu, S., "Anomalous lattice vibrations of single- and few-layer MoS2." *ACS nano*, Vol. 4, No. 5, May 2010, pp. 2695–700.

[84] Zhao, W., Ghorannevis, Z., Chu, L., Toh, M., Kloc, C., Tan, P.-H., and Eda, G., "Evolution of electronic structure in atomically thin sheets of WS2 and WSe2." *ACS nano*, Vol. 7, No. 1, Jan. 2013, pp. 791–7.

[85] Carvalho, B. R., Malard, L. M., Alves, J. M., Fantini, C., and Pimenta, M. A., "Symmetry-Dependent Exciton-Phonon Coupling in 2D and Bulk MoS 2 Observed by Resonance Raman Scattering," *Physical Review Letters*, Vol. 114, No. 13, April 2015, pp. 136403.

[86] Lucovsky, G. and White, R. M., "Optical-phonon anisotropies in layered crystals," *Il Nuovo Cimento B*, Vol. 38, No. 2, April 1977, pp. 290–300.

[87] Sears, W., Klein, M., and Morrison, J., "Polytypism and the vibrational properties of PbI_{2}," *Physical Review B*, Vol. 19, No. 4, Feb. 1979, pp. 2305–2313.

[88] Baltog, I., Lefrant, S., Mihut, L., and Mondescu, R., "Resonant Raman Scattering near the Band Gap in 4H-PbI2, Crystals)," *physica status solidi (b)*, Vol. 176, No. 1, March 1993, pp. 247–254.

[89] Richter, W., "Resonant Raman Scattering in Semiconductors," *Solid-State Physics*, Vol. 78 of *Springer Tracts in Modern Physics*, Springer Berlin Heidelberg, Berlin, Heidelberg, 1976, pp. 121–272.

[90] Grimsditch, M. and Cardona, M., "Absolute Cross-Section for Raman Scattering by Phonons in Silicon," *physica status solidi (b)*, Vol. 102, No. 1, Nov. 1980, pp. 155–161.

[91] Aggarwal, R., Farrar, L., Saikin, S., Aspuru-Guzik, A., Stopa, M., and Polla, D., "Measurement of the absolute Raman cross section of the optical phonon in silicon," *Solid State Communications*, Vol. 151, No. 7, April 2011, pp. 553–556.